Characterization of Quantum Sources of Light Generated By Parametric Down-Conversion Processes

A THESIS

submitted for the Award of Ph.D. degree of

MOHANLAL SUKHADIA UNIVERSITY

in the

Faculty of Science

by

Ali Anwar M A

Under the Supervision of

Prof. Ravindra P Singh

Professor

Atomic, Molecular, and Optical Physics Division

Physical Research Laboratory

Ahmedabad, India.

DEPARTMENT OF PHYSICS
MOHANLAL SUKHADIA UNIVERSITY
UDAIPUR
Year of submission: 2018

To

My Parents

DECLARATION

I, **Mr. Ali Anwar M A**, S/o Zubair M A, resident of Room No. 103, PRL Students Hostel, Thaltej, Ahmedabad, 380054, hereby declare that the research work incorporated in the present thesis entitled **Characterization of Quantum Sources of Light Generated by Parametric Down Conversion Processes** is my own work and is original. This work (in part or in full) has not been submitted to any University for the award of a Degree or a Diploma. I have properly acknowledged the material collected from secondary sources wherever required and I have run my entire thesis on the anti-plagiarism software namely, 'iThenticate'. I solely own the responsibility for the originality of the entire content.

Date:

(Ali Anwar M A)

CERTIFICATE

I feel great pleasure in certifying that the thesis entitled, **Characterization of Quantum Sources of Light Generated by Parametric Down Conversion Processes** embodies a record of the results of investigations carried out by Mr. Ali Anwar M A under my guidance. He has completed the following requirements as per Ph.D regulations of the University.

(a) Course work as per the university rules.

(b) Residential requirements of the university.

(c) Regularly submitted six monthly progress reports.

(d) Presented his work in the departmental committee.

(e) Published a minimum of one research paper in a referred research journal.

I am satisfied with the analysis, interpretation of results and conclusions drawn. I recommend the submission of the thesis.

Date:

Prof. Ravindra P Singh
(Thesis Supervisor)
Professor, AMOPH Division,
Physical Research Laboratory,
Ahmedabad - 380 009

Countersigned by

Head of the Department

Acknowledgements

When I write this, I feel that I have accomplished my goal to earn the highest degree in my academic career. This thesis is the final product of my five years' research career and I could not have done this without the support of many people with whom I interacted, shared and lived with. I am glad that I got a space here to put up words of gratitude towards all of them.

First, I thank the Almighty for giving me strength and showering his blessing upon me to carry out the work.

I am deeply indebted to my supervisor Prof. Ravindra Pratap Singh for his able guidance and frequent motivating words for the fulfilment of the research work. I feel very lucky to have such a gem of person as my supervisor who gave me a feeling like family. Many times, I had felt guilty that I couldn't do upto his expectations. During difficult times in my Ph.D life, his continued words of encouragement and coolness made me confident to keep on moving with my work. I could always freely discuss my scientific ideas with him, and he gave me courage and confidence to materialize them. I could always consider him like my father because of the simplicity in his personal as well as in professional lives.

I am very much thankful to Prof. Jagannath Banerji for his encouraging words in both personal and professional ways. I really enjoyed his classes in the English communication course he took during my course work. I take this opportunity to express my sincere gratitude to Dr. Goutam K Samanta for his encouragement in developing managerial skills for research. I have been observing since the starting of my Ph.D how he succeeded to bring a research laboratory to the best in a short period of time.

I take this opportunity to express my profound respect to PRL for providing the basic infrastructural facilities for carrying out the research work. I thank (Late) Prof. R. Ramesh, Dr. Bhuvan Joshi, Dr. Bijaya Sahoo, Dr. Navinder Singh, Dr. M. G. Yadava for taking various courses in physics and mathematical methods. My special thanks goes to the academic committee and my DSC members Prof. Jitesh Bhatt and Dr. Goutam K Samanta for thoroughly reviewing my work. Their support has served me well and I owe them my heartfelt appreciation. I express my sincere gratitude to M.Sc *project guide Dr. Alok Sharan, Pondicherry University, from whom I learned alignment skills in optics experiments. I express my profound respect to Dr. S V M Satyanarayana (Satya sir) whose classes motivated me to take up my research career in Quantum Optics.*

I am thankful to Dr. Chithrabhanu, for his encouragement and guidance in both the professional and the personal life. I learned how to identify new problems to work on while discussing quantum optics and quantum information with him. I would like to thank Dr. Shashi Prabhakar for his help in starting orbital angular momentum entanglement experiments in the lab. I have done a good part of my thesis work by disturbing him continuously with my doubts in experiments as well as in LabView programs. I would like to thank Dr. Pravin Vaity for his help in computational programs. I would say Dr. Pravin came to my research life accidentally. Although, our interests were two extremes, we sat together, discussed and developed a powerful computational code that supported many of our experiments. I am also happy to know that he also learned a lot during our discussions. I enjoyed working with all my lab mates – Dr. Vijay Kumar, Dr. Salla Gangi Reddy, Dr. Aadhi, Dr. Apurv, Dr. Avesh, Jabir, Varun, Nijil, Ayan and all the project associates who have completed their project work in our lab. My special thanks to Dr. Gangi for providing me tips to improve the quality of manuscript, and Jabir, Nijil and Ayan for the help in experiments. I thank them all for their full cooperation and ever needed help throughout to carry this work and also for being around all the time. Many thanks to Jabir and Nijil for their professional and personal interactions that made my work successful. I must thank Dr. Raghwinder Singh, Dr. Ravi Kiran, Dr. ASV Rao, Dr. Deepika, Mr. Anirban Gosh for experimental discussions.

I would like to say thanks to all my colleagues for making my stay in PRL comfortable. The 'THALTEJ GANG' - a group of some 'stress-free' souls, consisting of Jabir, Satish, Chandan, Prahlad, Kumar, Kuldeep, Yasir, Navpreet, Rukmani and Rupa, made my stay in PRL joyful. I thank them all for the 'stress-relieved' and funny moments we shared together. I thank my seniors for their advises during the research life. I am always thankful to my juniors for their pleasant smiles and short chit-chats that kept the campus alive. I am very thankful to my UG and PG batch mates from Pondicherry University for giving me a wonderful company during college life.

I am grateful to all the PRL library, computer center, dispensary and administration staff and also to the staff members of AMOPH Division of PRL for their sincere support. My special thanks to Ms. Pooja Chauhan who helped me a lot in administrative matters.

I thank Bivin Geo George for his frequent advises to step forward in each stages of the Ph.D work. I thank Swapna, Midhun, Lekshmi, Bhavya, Gaurav, Vishnu for building up a good friend circle. My special thanks to Swapna, Lekshmi and Bhavya for the nice lunches during Onam celebrations.

I have no words to express appreciation to my family. Without their love, inspiration and support I would not have been able to complete this work. I am grateful to my Mom and Dad, Zubair and Juvairiyya, for their moral support to complete the work. My three sisters, Azeema, Hadiya and Ayisha, and my brother-in-law Asweel, for keeping their companionship even when I couldn't see them frequently during my research life. I am thankful to all other family members and cousins for keeping frequent lively chats with me.

Acknowledging my life partner in a few words is a difficult task. My soulmate and my better half, Shibla, who came to my life in the final stages of my doctoral research. Even though we were physically apart due to academic reasons, I feel that it is just her love and care which kept me motivated to complete the thesis. I feel very lucky to have such a life partner who understands me always in a better way. Her pat on my back was enough to make myself stress-free during some hiccups in the work.

Ali Anwar M A

List of Abbreviations

SPDC	Spontaneous Parametric Down Conversion
OAM	Orbital Angular Momentum
LG	Laguerre Gaussian
CGH	Computer Generated Hologram or Holography
SPP	Spiral Phase Plate
POV	Perfect Optical Vortex
BG	Bessel-Gauss
SLM	Spatial Light Modulator
SPCM	Single Photon Counting Module

Table of contents

List of figures

Chapter 1

Introduction

The particle nature of light was first considered by Sir Isaac Newton in 1704. He proposed that light contains small particles having a mass. With this argument, he explained the basic phenomena of light such as reflection and refraction. However, his theory was discarded by the scientific community as it could not explain interference and diffraction, which are attributed to the wave nature of light. Thomas Young's double-slit interference experiment based on Huygen's wave theory became more popular among the community as it could explain refraction and reflection also. As a further advancement in the wave theory of light, Scottish physicist James Clark Maxwell found that the light indeed is an electromagnetic (EM) wave consisting of oscillating electric and magnetic fields. He derived a set of equations that describes the dynamics of EM waves propagating in a medium. From the theory, he could derive the speed of light in free space, which is one of the fundamental constants in Physics. Polarization is another important characteristic of light that Maxwell's EM wave theory could explain where the direction of electric field determines the polarization of light.

The particle nature of light, or the concept of photon, gained its ground after Einstein's discovery of photoelectric effect in 1905. He explained the effect with the help of Max Planck's quantum theory of radiation by considering light beam incident on the metal surface as discrete energy packets. Since the existence of matter waves was introduced by de Broglie in 1924, experiments showed that the light also have particle-like as well as wave-like behaviour. The area of quantum optics deals with the particle nature of light. In this, a light beam is considered as a stream of photons and different light sources are characterized by the number of photons seen in a particular time interval of detection.

Generally the quantum state of photon sources is represented by number states $|n\rangle$, where n is the number of photons, which is fixed. Different number states of light give different exotic features during their propagation and interaction in media [2–4]. However, such number states are difficult to realize practically. A stable laser having a constant intensity contains huge number of photons such that their number fluctuations are negligible. The number fluctuations become more sensible when a light source with $n = 1$ is considered, *i.e.* single photon states.

The basic qualities of an ideal single photon source is that it should emit a single photon at a certain time defined by the user. This means that the source is deterministic or the photon is emitted 'on demand'. Such deterministic single photon sources have been practically realized based on single atoms [5], single molecules [6], single ions [7], atomic ensembles [8] as well as from quantum dots [9, 10] and colour centers [11, 12]. All these sources emit single photons in a user-defined time. Apart from this, there are probabilistic single photon sources where the generation of single photons can be realized with certain probability, for a given time. Light sources based on parametric down conversion in non-linear bulk crystals [13, 14] and waveguides [15] come into later category where the qualification to be a single photon source is based on the photon pair emission and their 'heralded' detection. This means that one photon in the pair (heralding photon) is used to know the presence of the other (heralded single photon).

1.1 Classical description of light

1.1.1 Maxwell's equations

In the classical picture, light is considered as an electromagnetic wave composed of an electric field and a magnetic field which are orthogonal to each other. The electromagnetic wave theory of light is formulated using Maxwell's equations

$$\nabla \cdot \mathbf{D} = \rho \tag{1.1}$$

$$\nabla \cdot \mathbf{B} = 0 \tag{1.2}$$

$$\nabla \times \mathbf{E} = -\frac{\partial \mathbf{B}}{\partial t} \tag{1.3}$$

$$\nabla \times \mathbf{H} = \mathbf{J} + \frac{\partial \mathbf{D}}{\partial t} \tag{1.4}$$

where $\mathbf{D} = \varepsilon_0 \varepsilon_r \mathbf{E}$ is the electric displacement vector, $\mathbf{H} = \mathbf{B}/\mu_0 \mu_r$ is the magnetic field intensity, ρ is the free charge density and $\mathbf{J}$ is the free current density. The constants ε_0 and μ_0 are respectively the electric permittivity and magnetic permeability of the medium. ε_r and μ_r are the corresponding relative permittivity and permeability. From the Maxwell's equations, the following partial differential equation is derived

$$\nabla^2 \mathbf{E} = \mu_0 \varepsilon_0 \varepsilon_r \frac{\partial^2 \mathbf{E}}{\partial t^2} \tag{1.5}$$

which describes electromagnetic wave travelling in a medium with a speed $v = 1/\sqrt{\mu_0 \varepsilon_0 \varepsilon_r}$. For a light propagating in free space, $\varepsilon_r = 1$. Then the speed is given by

$$c = \frac{1}{\sqrt{\mu_0 \varepsilon_0}} \approx 3 \times 10^8 ms^{-1} \tag{1.6}$$

In a dielectric medium, the speed of light is given as

$$v = \frac{c}{\sqrt{\varepsilon_r}} = \frac{c}{n} \tag{1.7}$$

where $n = \sqrt{\varepsilon_r}$ is the refractive index of light in the medium. Equation 1.5 can be solved by considering electromagnetic waves as transverse waves where the associated electric field and magnetic fields are orthogonal to each other. Then the solutions are

$$E_x(z,t) = E_{x0} \cos(kz - \omega t + \phi) \tag{1.8}$$

$$B_y(z,t) = B_{y0} \cos(kz - \omega t + \phi)$$

where E_{x0} is the amplitude, ϕ is the phase and k is the magnitude of the propagation vector of the wave, given by

$$k = \frac{2\pi}{\lambda} = \frac{n\omega}{c} \tag{1.9}$$

Here, λ is the wavelength of light inside the medium. The flow of energy of the electromagnetic wave is obtained from the Poynting vector

$$\mathbf{S} = \mathbf{E} \times \mathbf{H} \tag{1.10}$$

The magnitude of the Poynting vector gives the intensity of the light. Taking a time average of the Poynting vector in Eqn. 1.10, the average intensity of the light is given as

$$\langle \mathbf{I} \rangle = \frac{1}{2} nc\varepsilon_0 E_{x0}^2 \tag{1.11}$$

1.1.2 Polarization

Polarization of light is generally associated with the direction of the electric field vector in the electromagnetic wave. Depending on different components of electric field and their orientation in transverse coordinate space, there are different types of polarization, as listed below

- **Linear**: The electric field vector oscillates along a particular direction. Generally, the light having electric field directed along X-axis and Y-axis are called as horizontally and vertically polarized, respectively.
- **Circular**: The electric field vector rotates about the axis of propagation as the wave advances. The light will be right-circularly/left-circularly polarized if the rotation of electric field is clockwise/anti-clockwise.
- **Elliptical**: As in the case of circular polarization, here, the electric field vector rotates as the wave propagates, except that the orthogonal components of the electric field have different amplitudes.
- **Unpolarized**: The electric field vector oscillates in a random direction.

Polarization of light does not change during its propagation in free space. However, in certain anisotropic media, polarization alters as the light propagates. Birefringence or Double refraction is a property of the material where an arbitrary polarized light separates into two light beams having orthogonal polarizations, called as ordinary and extra-ordinary light. The two light beams will have different refractive indices in the material and the difference of refractive indices quantifies the amount of birefringence in the material. Certain optical elements that manipulate the incoming polarization of light, such as polarizers, quarter-wave plates, half-wave plates are manufactured with these materials by using the birefringence property [16]. Birefringence of non-linear crystals has been widely utilized for studying various non-linear effects of light [17].

1.1.3 Interference and Diffraction

In the interference of light, two waves superpose to give a resultant wave having same, greater or lower amplitude. Consider two light waves having electric fields given by

$$\mathbf{E}_1(\mathbf{r},t) = \mathbf{E}_{01}\cos(\mathbf{k}_1\cdot\mathbf{r} - \omega t + \chi_1) \tag{1.12a}$$

$$\mathbf{E}_2(\mathbf{r},t) = \mathbf{E}_{02}\cos(\mathbf{k}_2\cdot\mathbf{r} - \omega t + \chi_2) \tag{1.12b}$$

The two waves superimpose to give a resultant field $\mathbf{E}_1 + \mathbf{E}_2$. To find the intensity of the wave combination, we first take the scalar product of the resultant field with itself

$$\mathbf{E}^2 = (\mathbf{E}_1 + \mathbf{E}_2)\cdot(\mathbf{E}_1 + \mathbf{E}_2) = \underbrace{\mathbf{E}_1^2 + \mathbf{E}_2^2}_{\text{Intensity addition}} + \underbrace{2\mathbf{E}_1\cdot\mathbf{E}_2}_{\text{Interference term}} \tag{1.13}$$

Intensity of the resultant field is obtained by taking the time average of Eqn. 1.13 on both sides, which reads

$$I = \langle\mathbf{E}_1^2\rangle_\mathrm{T} + \langle\mathbf{E}_2^2\rangle_\mathrm{T} + 2\langle\mathbf{E}_1\cdot\mathbf{E}_2\rangle_\mathrm{T} \tag{1.14}$$

Substituting the field expressions from Eqn.1.12b in Eqn. 1.14, one obtains time-averaged intensity of the resultant wave as

$$I = I_1 + I_2 + I_{12} \tag{1.15}$$

where I_1 and I_2 are given as

$$I_1 = \langle \mathbf{E}_1^2 \rangle_\mathrm{T} = \frac{E_{01}^2}{2} \tag{1.16}$$

$$I_2 = \langle \mathbf{E}_2^2 \rangle_\mathrm{T} = \frac{E_{02}^2}{2} \tag{1.17}$$

The third term in the right side of Eqn. 1.15 corresponds to the interference

$$I_{12} = 2\sqrt{I_1 I_2}\cos\delta \tag{1.18}$$

where $\delta = (\mathbf{k}_1 \cdot \mathbf{r} - \mathbf{k}_2 \cdot \mathbf{r} + \chi_1 - \chi_2)$ is the phase difference between the interacting waves. For even integral multiples of π, the waves will interfere constructively to give maximum intensity and for odd multiples of π, they interfere destructively to give minimum intensity.

For interference to occur, the two superposing waves must satisfy the following conditions

1. The interacting waves must be **coherent**.

2. The waves should be **monochromatic**.

3. The two waves must have same polarization.

Coherence is a property that describes the stability of light. For two light waves to be coherent, they have to propagate in space with a constant phase difference. The two types of coherence generally discussed are spatial and temporal coherences. Two light beams are said to be spatially coherent if there is a constant phase difference between the waves emerging from two laterally separate points in space. The waves are temporally coherent if one wave makes a constant phase lag with respect to the other, in time. Young's double slit interference and Michelson interferometer are the two well-known interference experiments in optics that illustrate the spatial and temporal coherence of a light source. In Young's double slit experiment, a single wavefront is divided into two secondary wavelets that are coming out of the slits and they superpose to give bright and dark fringes on screen. In the case of Michelson interferometer, the two interacting waves are formed from the amplitude division of a single wave train.

The term '*chrome*' came from the Greek word '*khrōma*' means colour. The two light waves must be monochromatic means that they must have same colour. This means that the two interfering waves must have same wavelength. Interference can happen between waves with wavelengths close to each other, and the resultant will form a group of waves with beats.

The interfering waves must have same polarization which means that their respective electric fields must oscillate in same direction. If the electric fields $\mathbf{E}_1$ and $\mathbf{E}_2$ are orthogonal, then the interference term in Eqn. 1.13 becomes zero and the resultant wave will be just the addition of intensities of individual waves.

Diffraction is another characteristic that describes the wave nature of light. In a simple way, diffraction of light is defined as the deviation of light from its rectillinear propagation when the light is obstructed by some means. There is no primary difference between interference and diffraction as the superposition of waves is involved in both. Conventionally, interference is considered the case of superposition of a few waves whereas, diffraction comes when one considers the interaction of a large number of waves. Generally, in the case of diffraction from an aperture or a slit, the condition for observing diffraction is that the wavelength of the light must be large compared to the size of the obstacle.

1.2 Classification of Light Sources Based on Photon Statistics

Photon statistics of a light source is carried out by studying the distribution of photons detected on photon counters in a given time for measurement. Consider a simple photon counting experiment where a low intensity light beam produced by attenuating a light source with neutral density filter, is incident on a photon counter (Fig. 1.1). A photon counter usually contains a sensitive photo detector such as photomultiplier tubes (PMT) or avalanche photodiode (APD). Electric pulses are generated from PMT/APD, corresponding to incidences. The photon counter is connected to an electronic circuit that counts the number of pulses in a given time. We consider the light beam as a stream of photons. The number of photons passing through a cross-section of the beam in unit time, the photon

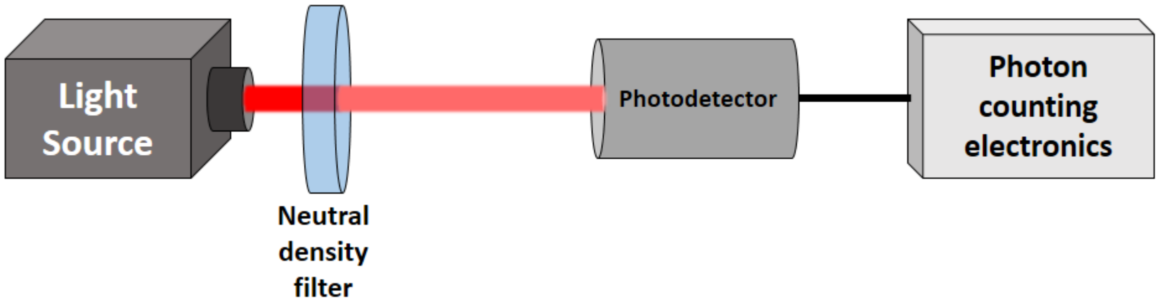

Fig. 1.1 Experimental setup for studying the photon statistics of a light source.

flux, is given by

$$\Phi = \frac{P}{\hbar\omega} \tag{1.19}$$

where P and ω are the optical power and the frequency of the light beam respectively. Photon detectors are characterized by their quantum efficiency η, which is defined as the ratio of number of photon counts registered in the detector to the number of photons incident on the detector. Therefore, the average number of photon counts recorded by the detector in a given time interval t, is given by

$$n_{pd}(t) = \eta\Phi t \tag{1.20}$$

In photon statistics, we find the probability, $\mathscr{P}(n)$, of finding n photons within a beam of certain length. Then we look what is the variation of the probability for different n values. Light sources are classified based on the distribution of this probability. For a coherent light source such as a laser, the distribution is Poissonian in nature where the variance of photon distribution is equal to the average number of photons in the distribution ($(\Delta n)^2 = \bar{n}$). All the other light sources are classified by comparing their photon statistics with that of the light source having Poissonian distribution. The classification is listed in Table 1.1 [18].

Photon statistics	**Example**	**Nature of intensity**	$(\Delta n)^2$
Sub-Poissonian	Single photon sources	Constant	$< \bar{n}$
Poissonian	Laser	Constant	$= \bar{n}$
Super-Poissonian	Thermal light source	Time varying	$> \bar{n}$

Table 1.1 Classification of light sources based on photon statistics

1.3 Quantum Sources of Light

Simply speaking, for a light source to have a quantum nature, it needs to emit photons that do not 'stick' to each other. This is called anti-bunching. To prove that the source is quantum, we need to device an experiment that gives evidence to the particle nature of light. That is, one has to confirm that the same photon cannot be present in two different locations in space at the same time. Consider a light source emitting single photons, *i.e.* one photon at a time. The photons are passing through a 50:50 beam splitter (BS), as shown in Fig. 1.2(a). Two single photon detectors D_1 and D_2 are kept at transmitted and reflected ports of the BS at equal distances. The detectors are connected to a coincidence counter that counts the simultaneous detection of photons at D_1 and D_2. When the source

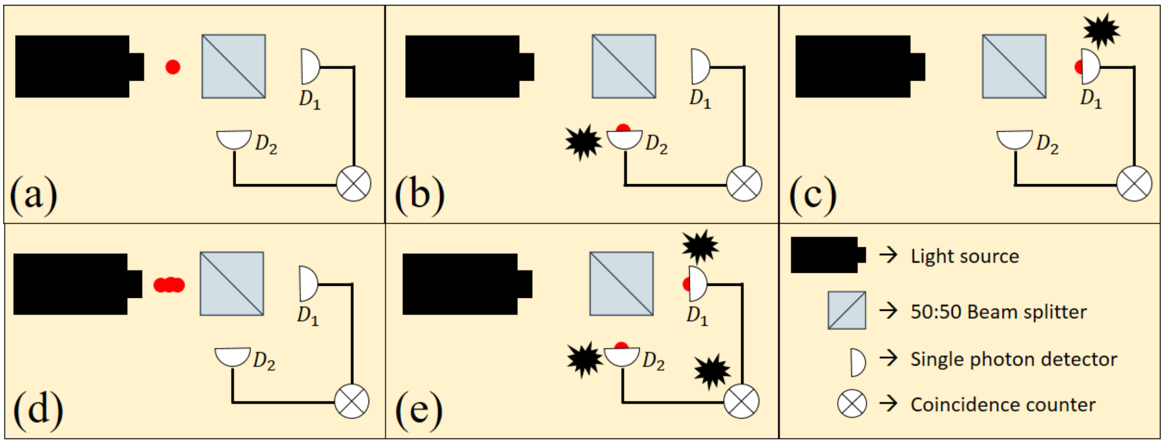

Fig. 1.2 Experimental setup for studying the quantum nature of a light source.

is emitting truly single photons, there is 50% probability of detecting the photon in each detectors at a given time (Fig. 1.2(b,c)) and therefore this will not give any coincident count at any instant. That confirms the anti-bunching nature of the photons. The experiment can be understood more clearly by introducing an anti-correlation parameter A, given by

$$A = \frac{P_{12}}{P_1 P_2} \tag{1.21}$$

where P_1 and P_2 are the probabilities of individual detection of photons at D_1 and D_2. P_{12} is the probability of coincident detection. In the case of a pure single photon source, as there are no coincidences, $A = 0$. If the detectors detect photons randomly and independently of each other, then there will be random appearances of coincident detection. According to the theory of probability, the probability of two independent random events occurring together is the product of their individual probabilities, therefore, $P_{12} = P_1 P_2$ and $A = 1$. For $A > 1$, the probability of simultaneous clicks of both detectors is more than that of a randomly clicking event. This happens when the photons come as clusters that show bunching effect, as shown in Fig. 1.2(d,e).

Suppose the counting experiment lasts for a time T, giving total number of individual counts N_1 and N_2 at detectors D_1 and D_2 respectively. N_{12} is the number of coincidence counts within the time interval Δt. Then the measured probability is given by

$$P_{12} = \frac{N_{12}}{\left(\frac{T}{\Delta t}\right)} \tag{1.22}$$

and the anti-correlation parameter is written as

$$A = \frac{N_{12}}{N_1 N_2}\left(\frac{T}{\Delta t}\right) \tag{1.23}$$

1.4 Quantum Entanglement

The basic unit of information is called a ‘bit’. A classical bit has two possible states, 0 and 1, in binary structure. However, a quantum bit or ‘qubit’, along with being in either $|0\rangle$ or $|1\rangle$, can also be in the superposition of both. A qubit is the fundamental unit of quantum information. A two-level system can be represented by a qubit. A qubit can be represented as

$$|\psi\rangle = \alpha|0\rangle + \beta|1\rangle \tag{1.24}$$

where α and β are complex probability amplitudes of the eigenstates $|0\rangle$ and $|1\rangle$ respectively, with the condition of normalization, $|\alpha|^2 + |\beta|^2 = 1$. The capabilities of a qubit over a classical bit lies in quantum superpositions, which give an infinite possibilities of other qubits.

One of the most popular candidate for qubit is photon [19]. For example, polarization of a single photon can be represented as

$$|\psi_{\text{pol}}\rangle = \alpha|H\rangle + \beta|V\rangle \tag{1.25}$$

where $|H\rangle$ (horizontal polarization) and $|V\rangle$ (vertical polarization) constitute the eigen-basis for the state.

Quantum entanglement is one of the key feature in quantum mechanics. The mathematical definition of a quantum entangled state is as follows: Consider a system represented by the state $|\psi\rangle$ and let the system consists of two sub-systems represented by states $|\psi_1\rangle$ and $|\psi_2\rangle$. The state $|\psi\rangle$ is said to be entangled if it cannot be written as a direct product of the states of sub-systems, *i.e.*

$$|\psi\rangle \neq |\psi_1\rangle|\psi_2\rangle \tag{1.26}$$

Then we say that there is entanglement between the two sub-systems. As an example, consider two photons labelled 1 and 2. Classically, the two photons can be in any one of the four possible polarization states $|H\rangle_1|H\rangle_2$, $|H\rangle_1|V\rangle_2$, $|V\rangle_1|H\rangle_2$ and $|V\rangle_1|V\rangle_2$. However in quantum mechanics, the superposition principle provides the possibility of constructing the state

$$|\psi\rangle = \alpha|H\rangle_1|H\rangle_2 + \beta|H\rangle_1|V\rangle_2 + \gamma|V\rangle_1|H\rangle_2 + \delta|V\rangle_1|V\rangle_2 \tag{1.27}$$

which is entangled in polarization. Here, the polarization state of either photon cannot be separated from the other, even if the two photons are physically separated. Any measurement carried out on one photon will modify the whole state as well as the state of the other photon. So the information about the polarization is distributed between the two photons. The four possible states with maximum entanglement are called Bell states. They are

$$|\psi^{+}\rangle = \frac{1}{\sqrt{2}}(|H\rangle_1|V\rangle_2 + |V\rangle_1|H\rangle_2), \tag{1.28}$$

$$|\psi^{-}\rangle = \frac{1}{\sqrt{2}}(|H\rangle_1|V\rangle_2 - |V\rangle_1|H\rangle_2), \tag{1.29}$$

$$|\phi^{-}\rangle = \frac{1}{\sqrt{2}}(|H\rangle_1|H\rangle_2 - |V\rangle_1|V\rangle_2), \tag{1.30}$$

$$|\phi^{-}\rangle = \frac{1}{\sqrt{2}}(|H\rangle_1|H\rangle_2 - |V\rangle_1|V\rangle_2). \tag{1.31}$$

1.5 Concept of Modes in Optics

The concept of modes is well-known in the field of optics. Basically, modes are orthogonal solutions of the wave equation that represent the propagation of light. Since they are orthogonal, they do not interfere. Number of photons in a particular mode determines the transfer of energy or information. The transverse characteristics of a mode are determined by boundary conditions and the longitudinal characteristics are determined by the coherence length. Some of the properties of modes are [20]:

- Since all the modes are orthogonal to one another, they do not interfere.
- Only photons having same mode interfere and therefore they are said to be coherent.
- The quality of the light source is characterized by the number of photons N, in a single mode considered. For a laser source, $N >> 1$ and for a thermal source, $N << 1$.
- Although the shape of modes may change after light propagates through or interacts with some passive optical elements (such as lens, mirror, prism etc.), the number of photons per mode does not change.

There are basically two types of modes. One category contains the spatial modes that are transverse to the direction of propagation, which determines the transverse characteristics of light. The other is called temporal modes which are along the direction of propagation and defines the spectral characteristics of light. The superposition of two spatial modes can give new modes. For example, superposition of two Laguerre-Guassian (LG) modes [21] of azimuthal indices +1 and -1 gives a first order Hermite-Gaussian (HG) mode, and vice versa. The transformation of corresponding normalized modes is given as

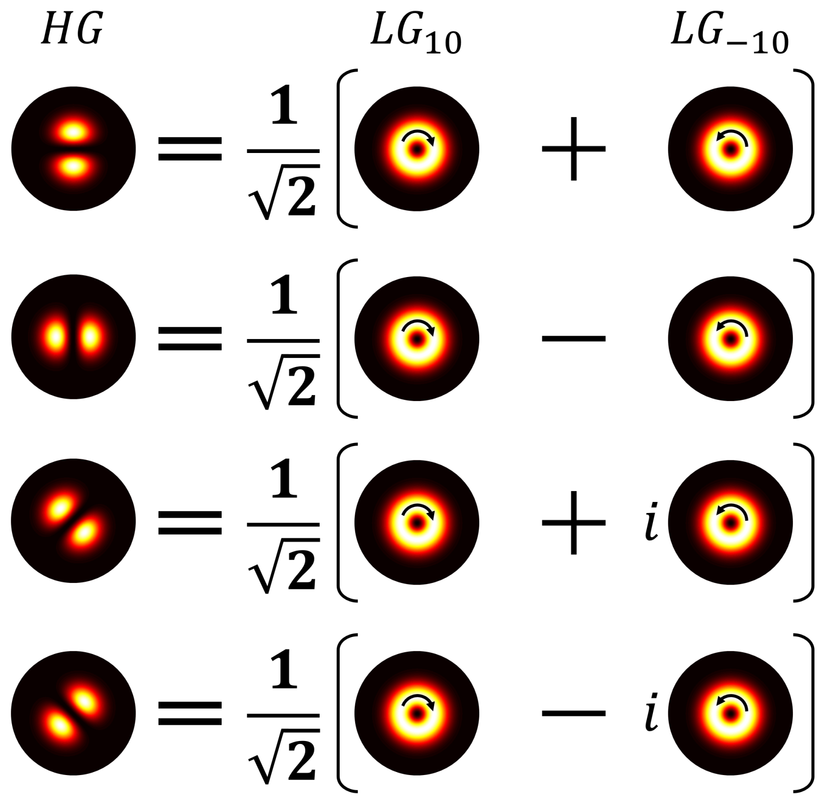

(1.32)

Different spatial modes show different properties of light that are utilized for various applications. For example, the joint spatial modes of two photons generated in spontaneous parametric down conversion is used to determine the orbital angular momentum (OAM) correlations and thus the OAM entanglement between them.

1.6 Objective of the Thesis

Photons have been used for realizing different protocols in quantum information. Developing a versatile source of single photons with lesser technical challenges is always desirable for the ease of applications. Spontaneous parametric down conversion is one of the well-known methods used to generate 'heralded' single photons by defining the quantum correlations between the twin photons generated. Our main objective is to generate and characterize the single photons produced in SPDC. First, we study the spatial characteristics of individual SPDC photons (without heralding) and compare the spatial distribution of SPDC for different pump modes. The stability of the quantum source of light generated by SPDC depends mainly on pump characteristics and the non-linear crystal dimensions. We generate heralded single photons and study how pump and crystal affect the heralding efficiency. We also generate heralded twisted single photons with different pump modes carrying orbital angular momentum (OAM) and compare them to see which pump could be used to give better heralding efficiency. All the above studies help us in determining the optimum experimental configuration for the efficient generation of heralded single photons. Finally, we study the OAM correlations present in SPDC biphoton modes. We experimentally demonstrate tuning of OAM biphoton states in multiple OAM eigenbases by controlling the OAM spectrum of the pump profile in the pump superposition.

1.7 Overview of the Thesis

The thesis is presented in six chapters. Chapter 1 gives a brief introduction on the classical and quantum nature of light along with the discussion on different properties of light such as interference, diffraction and polarization. A small description about the classification of light sources based on their photon statistics is given, as well as a brief description on quantum sources of light. The spatial modes of light are also explained. Chapter 2 provides the detailed theory of spontaneous parametric down conversion (SPDC) of light. The process is compared in both classical and quantum mechanical picture. A well used semi-classical theory is discussed with a brief derivation of joint spectral modes of SPDC. The phase-matching conditions for SPDC are explained along with the dispersion relations for refractive indices. A brief description of the non-classical effects in SPDC is also provided in Chapter 2. Chapter 3 deals with the spatial characteristics of SPDC photons with different pump modes. In this chapter, the angular spectrum of SPDC with different pump modes starting from Gaussian beams to light beams carrying orbital angular momentum (OAM) is explained. Also, the effects of pump and crystal parameters on the angular spectrum are discussed. In Chapter 4, the

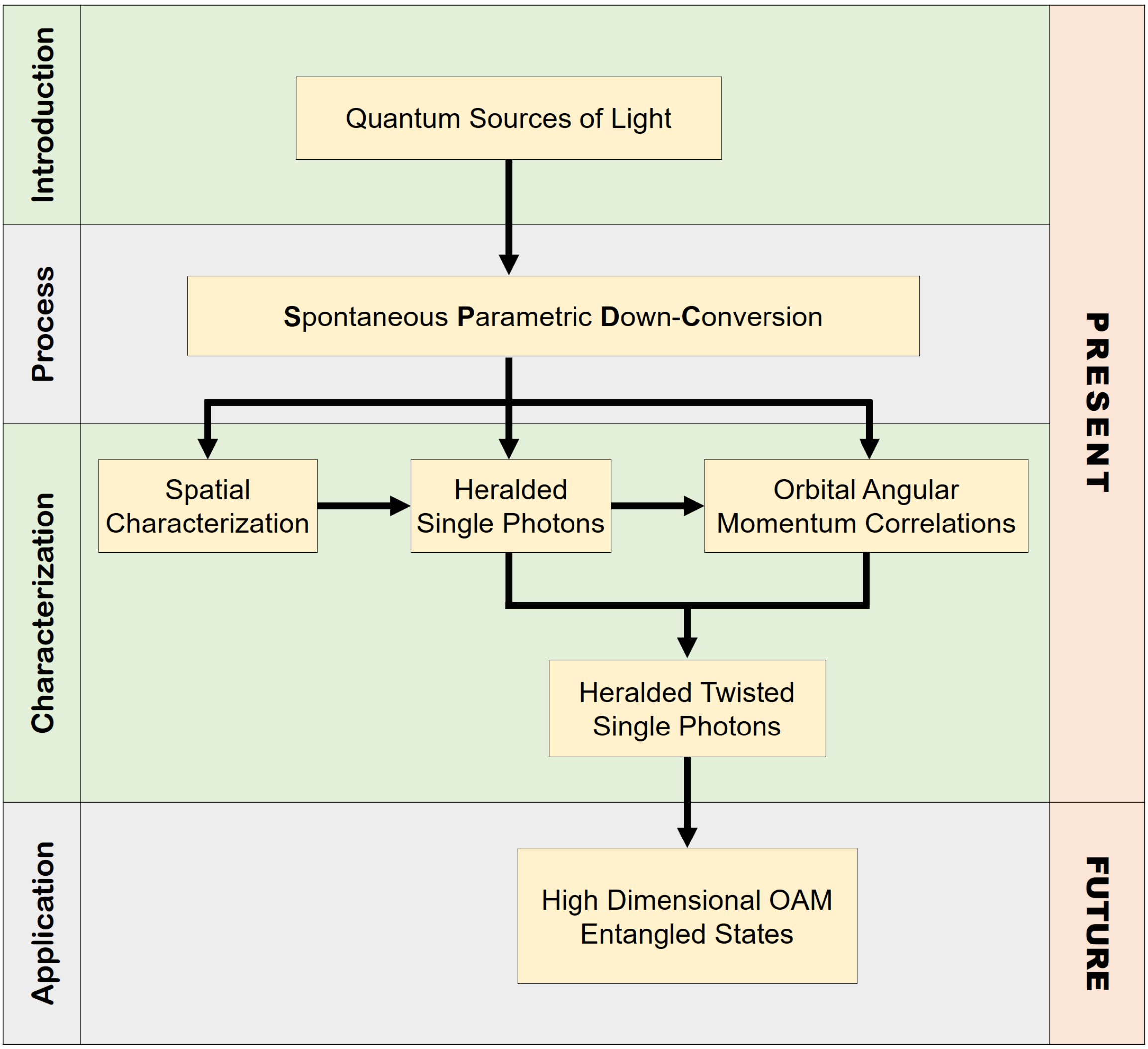

Fig. 1.3 Flowchart showing the distribution of thesis.

generation of heralded single photons from SPDC light source is discussed and the effect of pump focusing on the coupling efficiency is studied. The chapter also gives a comparative study of the heralding efficiency of the single photons carrying OAM generated using different pump modes. In Chapter 5, the correlations between SPDC signal and idler in OAM degree of freedom is discussed. Using the conventional method of analysing the biphoton OAM modes in SPDC, experimental results of the controlled generation of biphoton OAM modes in different OAM subspaces are presented. Conclusions and an outlook on future work are given in Chapter 6. An outline of the thesis is illustrated using a flowchart given in Fig. 1.3.

Chapter 2

Spontaneous Parametric Down Conversion of Light

Spontaneous parametric Down Conversion (SPDC) is a non-linear optical process in which a higher energy photon is converted into two lower energy photons. Historically the photon input to the medium is called as *pump* and the generated output photons are called as *signal* and *idler*. The process happens in a non-linear medium under certain conservation laws of energy and momentum. The process in *spontaneous* as there are no final states in the initial configuration. The term *parametric* refers to the fact that the interaction medium does not add or subtract energy or momentum in the process. SPDC is one of the easily realizable processes with clear manifestation of the quantum mechanical behaviour of light.

In the beginning after the first theoretical investigation [22] and experimental observation [23] of parametric Down Conversion in late 1960s, the process was commonly referred as parametric fluorescence or parametric scattering. In earlier days, the process of SPDC was used to measure non-linear optical coefficients of different materials [24]. The advantage of using this method over other processes like second harmonic generation is that the Down Conversion efficiency is independent of the pump power and therefore the measurement of absolute power of pump and signal is not required for the determination of optical non-linearity [25]. As the signal and idler photons are generated simultaneously inside a non-linear medium, correlations and entanglement have been defined between the photons in various degrees of freedom. Due to this, the process has become a versatile source of entangled photons for utilization as quantum states of light in quantum optics and quantum information. According to the conservation of energy and momentum in SPDC process, the photon pairs generated may be entangled in various degrees of freedom. Entanglement of SPDC photon pairs in space [26], time [27], frequency [28], polarization [29, 30] and orbital angular momentum [31] has been realized in recent years.

In this chapter, we give a detailed theoretical description of SPDC with the conditions for the process to occur in a non-linear medium. The conditions that drive parametric Down Conversion process is mainly the conservation of momentum, which is often known as *phase-matching*. In most of the cases, the phase matching is achieved using the birefringence property of the non-linear anisotropic crystal. In the last part of the chapter, we discuss different methods to observe non-classical effects between the photons generated in SPDC, and the entanglement in polarization and orbital angular momentum.

2.1 Non-linear Optics

In general, a light source propagating in free-space does not experience any change in its frequency. The frequency, which is a fundamental characteristic of light, changes when it passes through certain media. Such media are referred to non-linear media and the study of light propagation in non-linear media is termed as non-linear optics. The non-linear optical effects arise due to the polarization or dipole moment per unit volume induced by the electric field of the light propagating through the medium. The dielectric polarization induced by the electric field of the propagating wave is generally written as

$$P = \chi^{(1)}E_1 + \chi^{(2)}E_1E_2 + \chi^{(3)}E_1E_2E_3 + ... \tag{2.1}$$

where $\chi^{(n)}$ is the n^{th} -order susceptibility of the medium, which is generally an $(n+1)^{\text{th}}$ rank tensor. $\chi^{(1)}$ in Eqn. 2.1 describes light propagating in a linear media where the polarization varies linearly with electric field of the light. Light propagating through air, glass, water, lens etc. are some examples that show linear effects of light.

A non-linear medium will have higher order susceptibilities that will result in the change in the frequency of the light passing through it. Depending on how the input light is interacting in a non-linear media, new frequency components can be generated by addition or subtraction of frequency components of the input light waves. In a second order non-linear medium, frequencies can be added, subtracted and doubled. In a third order non-linear medium, the refractive index of the light in the medium is dependent on the the intensity of light. This shows third order non-linear effects like Kerr effect, self focusing, third harmonic generation etc. Here, we are interested in second order non-linearity. The second order term of polarization is written in tensor notation as

$$P_i^{(NL)} = \varepsilon_0 \sum_{j,k=1,2,3} \chi_{ijk} E_j E_k \tag{2.2}$$

The above equation is used to derive the electric fields of the output light in a second order process.

2.2 Theory of SPDC: Classical versus Quantum Treatment

In the classical description of SPDC, all the pump, signal and idler are described as monochromatic waves and the non-linear part of the polarization induced by respective electric fields is included in Maxwell's equations, which is given by

$$\nabla^2 \mathbf{E} - \frac{n^2}{c^2}\frac{\partial^2 \mathbf{E}}{\partial t^2} = \frac{1}{\varepsilon_0 c^2}\frac{\partial^2 \mathbf{P}^{(\mathrm{NL})}}{\partial t^2} \tag{2.3}$$

where c is the speed of light in vacuum and n is the refractive index of non-magnetic media. In the low-gain regime, the efficiency of parametric Down Conversion is very low. So, the amplitude of the pump field is assumed to be constant over the interaction. Under this case, the coupled wave equations for the amplitudes of generated fields E_s (signal) and E_i (idler) under slowly varying envelope approximation (SVEA) are derived from Eqn. 2.3 as

$$\frac{dE_s}{dz} = \frac{2i\omega_s^2 d_{\text{eff}}}{k_s c^2} E_p E_i^* e^{i\Delta kz}, \tag{2.4a}$$

$$\frac{dE_i}{dz} = \frac{2i\omega_i^2 d_{\text{eff}}}{k_i c^2} E_p E_s^* e^{i\Delta kz}. \tag{2.4b}$$

where $\Delta k = k_p - k_s - k_i$ is the phase mismatch. For solving the coupled equations, a perfectly phase-matched interaction ($\Delta k = 0$) is assumed. So the general solution of the differential equations 2.4b has identical forms for both signal and idler

$$E_j(z) = c_1 \sinh(\eta z) + c_2 \cosh(\eta z) \tag{2.5}$$

where

$$\eta^2 = \frac{4\omega_j^2 \omega_p^2}{k_j k_p c^4} |E_p|^2 \tag{2.6}$$

with $j = s, i$, denoting signal and idler respectively. The constants of integration c_1 and c_2 are determined from the boundary conditions. As there are no generated fields at the input of SPDC, the boundary conditions are $E_s(0) = E_i(0) = 0$. Therefore, the final solution is given as

$$E_s(z) = E_s(0)\cosh(\eta z) - iE_i(0)^* \sinh(\eta z) \tag{2.7a}$$

$$E_i(z) = E_i(0)\cosh(\eta z) - iE_s(0)^* \sinh(\eta z) \tag{2.7b}$$

With the boundary conditions of SPDC, there are no output fields generated in the process, according to Eqn. 2.7b. Although feeble, the down converted photons are created as the amplification of vacuum fluctuations that cannot be explained using classical theory. So, quantum mechanical theory has to be manifested for the proper justification of SPDC process. In the case of a parametric Down Conversion process, as only the pump field is present initially, a complete classical treatment of the interaction cannot explain the generation of down converted light. Based on the second quantization formalism in Quantum Field Theory, a zero-point vacuum fluctuation gives rise to the frequencies ω_1 & ω_2, which

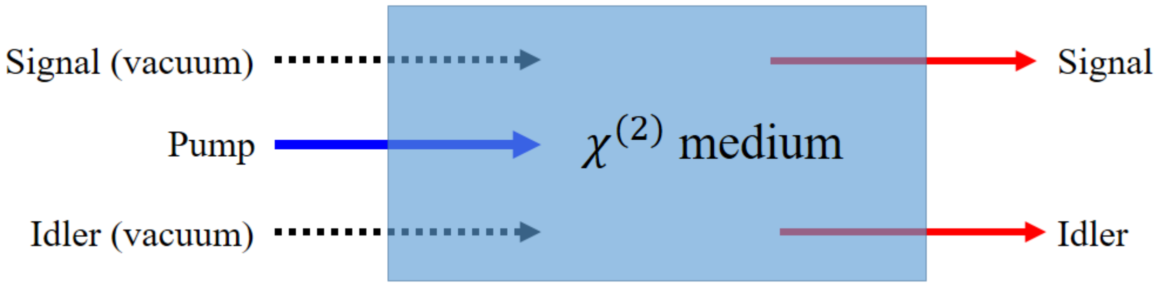

Fig. 2.1 Four-port model of spontaneous parametric Down Conversion process in a $\chi^{(2)}$ medium. The dashed arrows represent the initial vacuum states that involve in interaction with pump in the medium.

will be amplified by the interaction with the pump field in the non-linear medium. In other words, the process can be viewed as a four-port model given in Fig. 2.1.

In the quantum mechanical description of parametric Down Conversion, the electric fields given by Eqn. 2.5 are replaced by its quantum operators as $E_j(z) \rightarrow \hat{a}_j(z)$ where $\hat{a}_j(z)$ is the annihilation operator and $j = s, i$. The annihilation and creation operators must satisfy commutation relations

$$[\hat{a}_k(z), \hat{a}_l^\dagger(z)] = \delta_{kl} \tag{2.8a}$$

$$[\hat{a}_k(z), \hat{a}_l(z)] = 0 \tag{2.8b}$$

where $\{k,l\} = \{s,i\}$. The photon flux density operator, which gives the mean number of photons per unit area, is given as $\hat{I}_j(z) = \hat{a}_j^\dagger(z)\hat{a}_j(z)$. The time independent quantum mechanical Hamiltonian of SPDC has the form

$$\hat{\mathscr{H}}_I = \hbar\chi^{(2)}(\hat{a}_p^\dagger\hat{a}_s\hat{a}_i + \hat{a}_p\hat{a}_s^\dagger\hat{a}_i^\dagger) \tag{2.9}$$

where the operators $\hat{a}_p, \hat{a}_s, \hat{a}_i$ and $\hat{a}_p^\dagger, \hat{a}_s^\dagger, \hat{a}_i^\dagger$ are the annihilation and creation operators for pump, signal and idler fields respectively. Assuming the pump to be in a coherent state $E_p(t) = E_{p0}e^{-i\omega_p t}$, Eqn. 2.9 is modified as

$$\hat{\mathscr{H}}_I = \hbar\chi^{(2)}(E_p^*\hat{a}_s\hat{a}_i + E_p\hat{a}_s^\dagger\hat{a}_i^\dagger) \tag{2.10}$$

According to Heisenberg picture in quantum mechanics, the signal field is evolved in time as

$$\begin{aligned}\frac{d\hat{a}_s}{dt} &= -\frac{i}{\hbar}[\hat{a}_s, \mathscr{H}_I] \\ &= -i\chi^{(2)}\left(\hat{a}_s\left(E_p^*\hat{a}_s\hat{a}_i + E_p\hat{a}_s^\dagger\hat{a}_s^\dagger\right) - \left(E_p^*\hat{a}_s\hat{a}_i + E_p\hat{a}_s^\dagger\hat{a}_s^\dagger\right)\hat{a}_s\right) \\ &= -i\chi^{(2)}E_p\hat{a}_i^\dagger\end{aligned} \tag{2.11}$$

Similar equation can be derived for idler photon in the same manner

$$\frac{d\hat{a}_i}{dt} = -i\chi^{(2)}E_p\hat{a}_s^\dagger \tag{2.12}$$

Equations 2.11 and 2.12 form coupled differential equations identical to that in the classical description. The solution can be directly written as

$$\hat{a}_s(t) = \hat{a}_s(0)\cosh(\chi^{(2)}E_pt) - i\hat{a}_i^\dagger(0)\sinh(\chi^{(2)}E_pt) \tag{2.13a}$$

$$\hat{a}_i(t) = \hat{a}_i(0)\cosh(\chi^{(2)}E_pt) - i\hat{a}_s^\dagger(0)\sinh(\chi^{(2)}E_pt) \tag{2.13b}$$

Although the above solution looks similar to that with classical approach, the presence of the creation operators in the second term on the right-had side drives the generation of signal and idler photons even if the input states are vacuum.

According to classical electrodynamics, the displacement vector **D** is given by $\mathbf{D} = \varepsilon_0\mathbf{E} + \mathbf{P}$ where **P** is the polarization. Then the classical Hamiltonian for electric field is written as [32]

$$\mathscr{H}_{EM} \propto \int \mathbf{E}(\mathbf{r},t)\cdot\mathbf{D}(\mathbf{r},t)d^3r \tag{2.14}$$

Considering only the the second-order non-linear part in **D**, the interaction Hamiltonian for the process is given by the volume integral

$$\mathscr{H}_I \propto \int_V \chi^{(2)}E_p(r,t)E_s(r,t)E_i(r,t)d^3r \tag{2.15}$$

In the multimode perturbative description of SPDC,

$$\mathscr{H}_I^{(SPDC)} \propto \int_V \chi^{(2)} \hat{E}_p^{(+)}(r,t) \hat{E}_s^{(-)}(r,t) \hat{E}_i^{(-)}(r,t) d^3r + h.c \tag{2.16}$$

where p, s & i are labelled as pump, signal and idler fields respectively. The plus and minus signs in the superscript corresponds to positive and negative frequency parts of the fields respectively. Although the quantum mechanical Hamiltonian explains some characteristics of the SPDC process, it cannot give proper description in some other cases, as the down converted fields can be far away from monochromatic behaviour. Although the sum of signal and idler frequencies gives almost a single value, each signal or idler photon can have wider bandwidth, and thus it behaves mostly as a wave-packet. Therefore, for more realistic treatment of the process, we consider a plane wave mode series expansion of each field and take pump field to be classical

$$E_p^{(+)} = E_p^{(-)*} = \int d\omega_p \alpha(\omega_p) \exp[i(k_p(\omega_p)z - \omega_p t)] \tag{2.17}$$

$$\hat{E}_{s,i}^{(+)} = \hat{E}_{s,i}^{(-)\dagger} = A \int d\omega_{s,i} \exp[i(k_{s,i}(\omega_{s,i})z - \omega_{s,i}t)] \hat{a}_{s,i}(\omega_{s,i}) \tag{2.18}$$

where $\alpha(\omega_p)$ is the amplitude spectral function of the pump field. Based on Shrödinger picture in quantum mechanics, the generated output state of the photons at later time, t, of interaction, is given by a unitary operator acting on the initial state $|\Psi(0)\rangle$

$$|\Psi(t)\rangle = \exp\left[-\frac{i}{\hbar}\int_0^t dt' \mathscr{H}_I^{SPDC}(t')\right]|\Psi(0)\rangle \tag{2.19}$$

In the case of SPDC, the initial states are vacuum states, $|0\rangle_s|0\rangle_i$. Taking the perturbative expansion of Eqn. 2.19 and truncating it to first order, we obtain

$$|\Psi(t)\rangle = |0\rangle_s|0\rangle_i - \frac{i}{\hbar}\int_0^t dt' \mathscr{H}_I^{SPDC}(t')|0\rangle_s|0\rangle_i \tag{2.20}$$

The first term in Eqn. 2.20 describes the generation of vacuum state. The photon pair emission is described in the second term. The neglected higher order terms in the expansion corresponds to the emission of more than two photons and their probability is too small if the input pump is not so intense. Using equations 2.16, 2.17, 2.18, 2.20 and performing a z-integral, we get

$$\int_0^t dt' \mathscr{H}_I^{SPDC}(t') = B \int_0^t dt' \int\int\int d\omega_p d\omega_s d\omega_i \alpha(\omega_p) \mathrm{e}^{-i\Delta\omega t'} L\mathrm{sinc}\left(\frac{\Delta kL}{2}\right) \hat{a}_s^\dagger(\omega_s)\hat{a}_i^\dagger(\omega_i) + h.c \tag{2.21}$$

where $\Delta\omega = \omega_p - \omega_s - \omega_i$ is the frequency mismatch derived from the energy conservation. The $\Delta k = k_p - k_s - k_i$ is the wave-vector mismatch obtained from momentum conservation. All the constants outside the time integral are absorbed in the constant, B. The time integration in Eqn. 2.21 can be performed by extending the limits from $-\infty$ to ∞, as we can consider the state of PDC long before and after the crystal. The time integral will result in a delta function $2\pi\delta(\Delta\omega)$. Integrating over ω_p and simplifying Eqn. 2.21, we obtain the final state of SPDC as

$$|\Psi\rangle_{SPDC} = |0\rangle_s|0\rangle_i + B' \int\int d\omega_s d\omega_i \phi(\omega_s,\omega_i)\hat{a}_s^\dagger(\omega_s)\hat{a}_i^\dagger(\omega_i)|0\rangle_s|0\rangle_i \tag{2.22}$$

where

$$\phi(\omega_s,\omega_i) = \alpha(\omega_s+\omega_i)\mathrm{sinc}\left(\frac{\Delta k(\omega_s,\omega_i)L}{2}\right) \tag{2.23}$$

is the joint spectral amplitude (JSA) of SPDC photon pairs. The new scaling factor B' outside the integral in Eqn. 2.22 is proportional to the product of the amplitude of the pump field E_p and the crystal length L.

2.3 Phase-Matching in Parametric Down Conversion

A degenerate SPDC process can be apparently considered as the inverse of second harmonic generation. For the SPDC to occur, the energy conservation must satisfy

$$\omega_\mathrm{p} = \omega_\mathrm{s} + \omega_\mathrm{i} \tag{2.24}$$

where ω_p, ω_s & ω_i are the angular frequencies of pump, signal & idler fields respectively. This is not the only condition for SPDC to occur. The down converted photons generated at one location inside the non-linear medium may interfere destructively with photons generated in other locations inside the medium so that no effective Down Conversion happens. Therefore, for the process to occur, the photons generated at different locations in the medium have to be phase matched, which is expressed as

$$\mathbf{k}_{\mathrm{p}} = \mathbf{k}_{\mathrm{s}} + \mathbf{k}_{\mathrm{i}} \tag{2.25}$$

where $\mathbf{k}_{\mathrm{j}}$ are the wave-vectors of the interacting waves with frequencies ω_{j} $(\mathrm{j} = \mathrm{p}, \mathrm{s}, \mathrm{i})$. The magnitude of the wave-vectors is given by

$$k_{\mathrm{j}} = |\mathbf{k}_{\mathrm{j}}| = \frac{\omega_{\mathrm{j}} n_{\mathrm{j}}(\omega_{\mathrm{j}})}{c} \tag{2.26}$$

where $n_{\mathrm{j}}(\omega_{\mathrm{j}})$ are the refractive indices of the interacting waves and c is the speed of light in vacuum. Considering $\omega_{\mathrm{i}} \leq \omega_{\mathrm{s}} \leq \omega_{\mathrm{p}}$, the effect of normal dispersion gives $n_{\mathrm{i}} \leq n_{\mathrm{s}} \leq n_{\mathrm{p}}$. Substituting Eqn. 2.26 in Eqn. 2.25 and simplifying, we obtain

$$\omega_{\mathrm{p}} n_{\mathrm{p}}(\omega_{\mathrm{p}}) = \omega_{\mathrm{s}} n_{\mathrm{s}}(\omega_{\mathrm{s}}) + \omega_{\mathrm{i}} n_{\mathrm{i}}(\omega_{\mathrm{i}}) \tag{2.27}$$

Combining equations 2.25 and 2.27 we can write the following expression

$$(n_{\mathrm{p}} - n_{\mathrm{s}})\omega_{\mathrm{p}} = (n_{\mathrm{i}} - n_{\mathrm{s}})\omega_{\mathrm{i}} \tag{2.28}$$

where $n_{\mathrm{j}} \equiv n_{\mathrm{j}}(\omega_{\mathrm{j}}), (\mathrm{j} = \mathrm{p}, \mathrm{s}, \mathrm{i})$. For normal dispersion, the inequalities $(n_{\mathrm{p}} - n_{\mathrm{s}}) > 0$ and $(n_{\mathrm{i}} - n_{\mathrm{s}}) < 0$ must be satisfied. This cannot be achieved in normal dispersive materials. However, the phase-condition given in Eqn.2.27 can be realized in materials showing anomalous dispersion where the refractive index decreases with increasing frequency. Using the birefringence present in anisotropic crystals, one can achieve perfect phase-matching. Birefringence (or double refraction) is the property of a material which has a refractive index dependent on the polarization as well as the propagation direction of light. There are two refracted light beams in a birefringent material with refractive indices $n^{(o)}$ and $n^{(e)}$ corresponding to ordinary (o) and extra-ordinary (e) polarizations of light, respectively.

The refractive index in anisotropic crystals is generally defined as a tensor having three different principal components $n_{\mathrm{j}}, (\mathrm{j} = 1, 2, 3)$, each along three axes X, Y, Z respectively [33]. For biaxial crystals, $n_1 \neq n_2 \neq n_3$. For uniaxial crystals, $n_1 = n_2 = n_o$ corresponding of ordinary light and

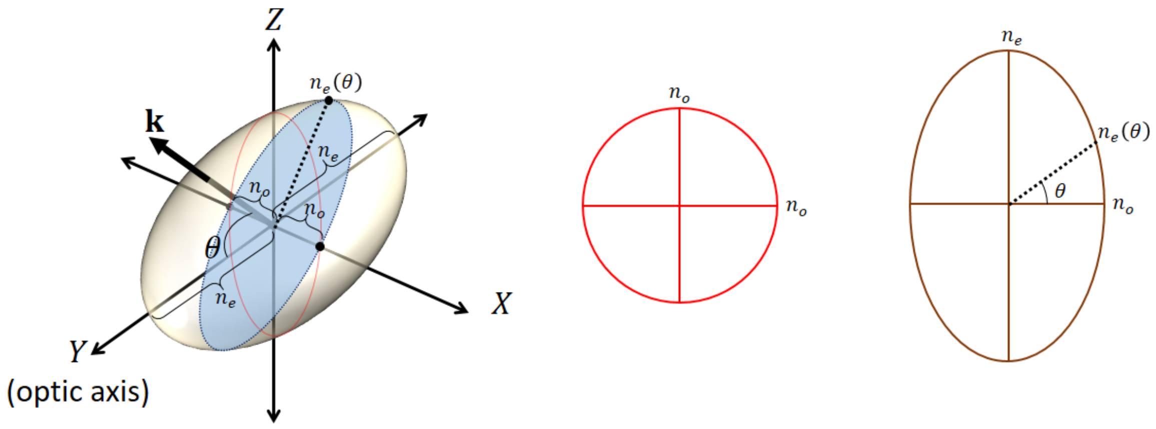

(a) (b) (c)

Fig. 2.2 (a) Index ellipsoid, the graphical representation of refractive indices along different directions, in a uniaxial crystal. (b) Due to rotational symmetry of the ellipsoid, the circular portion of the ellipsoid in the XZ-plane intersect the shaded ellipse at two points, defining the value of n_o. (c) The value of $n_e(\theta)$ is defined by the semi-axis of the index ellipse lying in the principal plane (plane containing wave-vector **k** and optic axis) of the crystal.

$n_e = n_3 \neq n_o$ corresponding to extra-ordinary light. For positive uniaxial crytal, $n_e > n_o$ and for negative uniaxial crystal, $n_e < n_o$. The difference between ordinary and extra-ordinary refractive indices gives the amount of birefringence in the crystal.

In uniaxial crystals, principal plane is defined as the plane containing the wave-vector **k** and optic axis of the crystal. An ordinary light is polarized perpendicular to the principal plane and an extra-ordinary light is polarized in the principal plane. The ordinary refractive index is independent of the direction of propagation of light, whereas the extra-ordinary refractive index depends on the direction, i.e. $n_e = n_e(\theta)$. where θ is the angle of the wave-vector with respect to the optic axis. The values of ordinary and extra-ordinary refractive indices in crystal coordinate space are graphically represented as an index ellipsoid, as shown in Fig. 2.2 for a uniaxial crystal. Due to the rotational symmetry of the ellipsoid around the optic axis (Y-direction in Fig. 2.2(a)), the radius of the circle cut out from the portion of ellipsoid in XZ-plane defines the value of n_o, shown in Fig. 2.2(b). The semi-major and semi-minor axes of the ellipse shaded in blue (Fig. 2.2(a) cut out from ellipsoid, perpendicular to the wave-vector, gives the values of $n_e(\theta)$ and n_o respectively. The values of $n_e(\theta)$

for different θ can be obtained by considering the index ellipse along the principal plane (plane containing wave-vector $\mathbf{k}$ and optic axis) of the crystal shown in Fig. 2.2(c), with the ellipse equation

$$\frac{1}{n_e(\theta)^2} = \frac{\sin^2\theta}{n_e^2} + \frac{\cos^2\theta}{n_o^2} \tag{2.29}$$

To achieve phase-matching condition in uniaxial crystals, the pump has to be polarized in the plane having the lowest among the two refractive indices and atleast one among the down converted photons must be orthogonally polarized to the pump. In this regard, there can be two types of phase-matching in uniaxial crytals - Type-I and Type-II. In Type-I phase matching, both signal and idler have same polarization whereas they are orthogonally polarized in Type-II phase-matching. Table 2.1 gives different types of SPDC phase-matching schemes for positive and negative uniaxial crystals.

Type	**Positive uniaxial** $(n_e > n_o)$	**Negative uniaxial** $(n_e < n_o)$
Type-I	$n_o^{(\mathrm{p})}\omega_\mathrm{p} = n_e^{(\mathrm{s})}\omega_\mathrm{s} + n_e^{(\mathrm{i})}\omega_\mathrm{i}$	$n_e^{(\mathrm{p})}\omega_\mathrm{p} = n_o^{(\mathrm{s})}\omega_\mathrm{s} + n_o^{(\mathrm{i})}\omega_\mathrm{i}$
Type-II	$n_o^{(\mathrm{p})}\omega_\mathrm{p} = n_o^{(\mathrm{s})}\omega_\mathrm{s} + n_e^{(\mathrm{i})}\omega_\mathrm{i}$	$n_e^{(\mathrm{p})}\omega_\mathrm{p} = n_e^{(\mathrm{s})}\omega_\mathrm{s} + n_o^{(\mathrm{i})}\omega_\mathrm{i}$

Table 2.1 Phase-matching conditions for different types of uniaxial crystals. The labels o and e denotes ordinary and extra-ordinary polarizations, respectively.

Practically, the values of n_o and n_e are calculated from Sellmeier equations, given by

$$n_{o,e}^2(\lambda) = A_{o,e} + \frac{B_{o,e}}{\lambda^2 - C_{o,e}} + D_{o,e}\lambda^2 \tag{2.30}$$

where λ is the wavelength of light in μm. The coefficients A, B, C & D are determined from spectrometric measurements using the crystal and are given in literature [34]

Consider the case of a degenerate SPDC where a pump of frequency ω_p is down converted to two signal and idler, each having frequency $\omega_\mathrm{p}/2$ ($\omega_\mathrm{s} = \omega_\mathrm{i} = \frac{\omega_\mathrm{p}}{2}$). Substituting these in Eqn. 2.26 and using it in Eqn.2.25, we get the phase-matching condition as

$$n(\omega_\mathrm{p}) = n(\frac{\omega_\mathrm{p}}{2}) \tag{2.31}$$

In most of the birefringent crystals, angle tuning is the commonly used method to match the refractive indices of the interacting waves. In some crystals like lithium niobate, the birefringence is

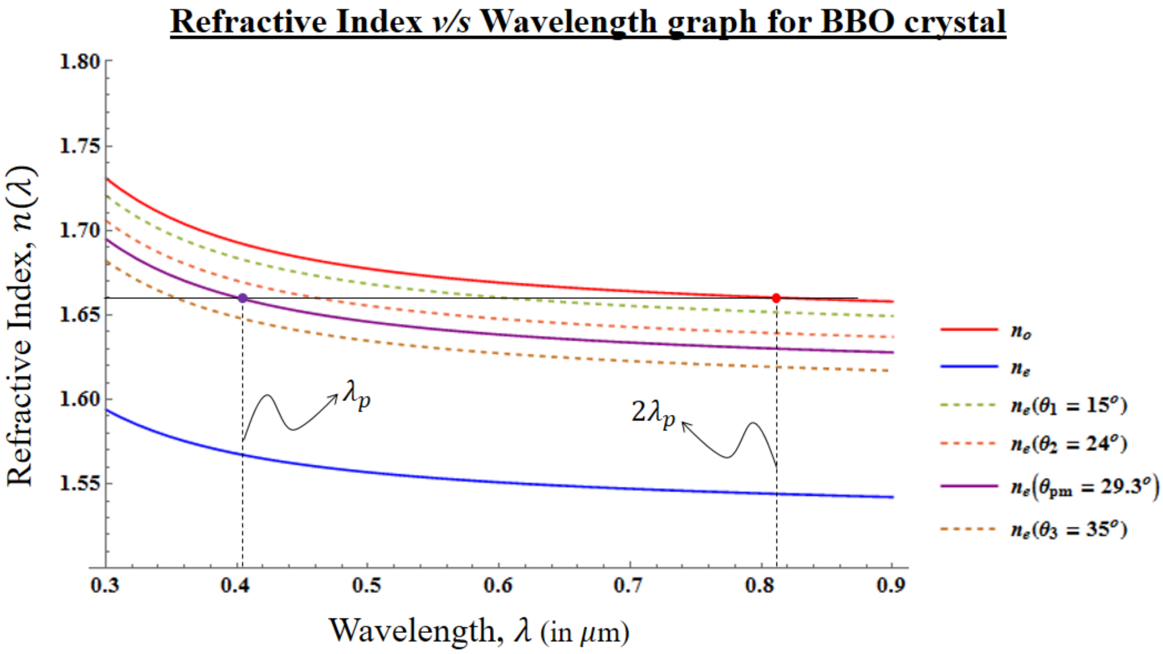

Fig. 2.3 Plot of refractive index of o-wave and e-wave with wavelength for different phase-matching angles, based on the Sellmier equations. At the perfect phase-matching angle, $\theta_{\mathrm{pm}} = 29.3^{\mathrm{o}}$, the $n_e(\lambda_p = 405nm)$ matches with $n_o(2\lambda_p = 810nm)$ with an approximate value of 1.66. The dashed plots are the index curves for other angles.

strongly dependent on temperature of the crystal and therefore a temperature tuning is done to achieve phase-matching. The birefringent crystals used in our lab are β-Barium Borate (BBO) and Bismuth Barium Borate (BiBO) fabricated for a degenerate SPDC of a pump photon of wavelength 405 nm to two 810 nm photons. The Sellmier equations for BBO crystal are

$$n_o(\lambda) = \sqrt{2.7359 + \frac{0.01878}{\lambda^2 - 0.01822} + 0.01354\lambda^2} \tag{2.32}$$

$$n_e(\lambda) = \sqrt{2.3753 + \frac{0.01224}{\lambda^2 - 0.01667} + 0.01516\lambda^2} \tag{2.33}$$

$$n_e(\lambda, \theta) = n_o(\lambda)\sqrt{\frac{1 + \tan^2\theta}{1 + \left(\frac{n_o(\lambda)}{n_e(\lambda)}\tan\theta\right)^2}} \tag{2.34}$$

Here, λ is in μm. BBO is a negative uniaxial crystal. The phase-matching can be achieved by calculating the phase-matching angle of the crystal, θ_{pm}, for which $n_e(\omega_p, \theta_{\mathrm{pm}}) = n_o(\omega_p/2)$

2.4 Non-Classical Effects in Parametric Down Conversion

Suppose, one of the SPDC pair photons is separated and detected using an avalanche photo-diode (APD), it will confirm the presence of the other photon, known as heralding. So, SPDC acts as a source of single photons, called as heralded single photon source, with each photon from the pair being detected simultaneously at two different APDs. Taking an ensemble of photon pairs, study of the photon statistics shows that the photon pair source generated in SPDC is indeed a non-classical source [35]. However, to prove the true quantum nature of the source, one has to prove the simultaneity of the generation of signal and idler in a generated SPDC pair. This can be proved by recombining the signal and idler photon at a 50:50 beam splitter and show the bunching of the photons. A beam splitter is a useful tool in quantum optics, as it helps in observing interference effects between weakly interacting fields. So, they can be used to illustrate the bosonic nature of single photons. Consider a beam splitter, shown in Fig. 2.4, having reflection and transmission coefficients, R and T respectively. The output modes can be written in terms of input modes as

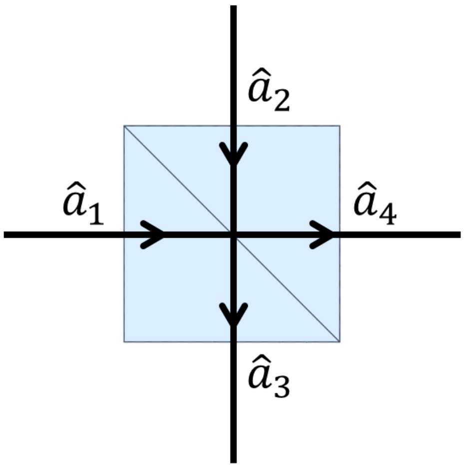

Fig. 2.4 Four port model illustrating the input and output modes of a beam splitter.

$$\hat{a}_3 = R\hat{a}_1 + T\hat{a}_2 \tag{2.35a}$$

$$\hat{a}_4 = T\hat{a}_1 - R\hat{a}_2 \tag{2.35b}$$

The minus sign in second equation is coming from the maintenance of energy conservation at the beam splitter interface so that R and T are real. Using the energy conservation relation $R^2 + T^2 = 1$, the creation operators for input modes in terms of that of the output modes can be written as

$$\hat{a}_1^\dagger = R\hat{a}_3^\dagger + T\hat{a}_4^\dagger \tag{2.36a}$$

$$\hat{a}_2^\dagger = T\hat{a}_3^\dagger - R\hat{a}_4^\dagger \tag{2.36b}$$

For the case of a single photon incident at each input port of a beam splitter, the output state is

$$\begin{aligned}
|\psi\rangle &= \hat{a}_1^\dagger\hat{a}_2^\dagger|0\rangle \\
&= (R\hat{a}_3^\dagger + T\hat{a}_4^\dagger)(T\hat{a}_3^\dagger - R\hat{a}_4^\dagger)|0\rangle \\
&= (RT\hat{a}_3^\dagger\hat{a}_3^\dagger + T^2\hat{a}_4^\dagger\hat{a}_3^\dagger - R^2\hat{a}_3^\dagger\hat{a}_4^\dagger - TR\hat{a}_4^\dagger\hat{a}_4^\dagger)|0\rangle
\end{aligned} \tag{2.37}$$

For a 50:50 beam splitter, $R = T = 1/\sqrt{2}$ and $T^2 - R^2 = 0$. Also the operators $\hat{a}_3^\dagger$ and $\hat{a}_4^\dagger$ does commute. So, Eqn. 2.37 is simplified to give

$$|\psi\rangle = \frac{1}{\sqrt{2}}(\hat{a}_3^\dagger\hat{a}_3^\dagger - \hat{a}_4^\dagger\hat{a}_4^\dagger)|0\rangle \tag{2.38}$$

The four possible output configurations for two photons, one incident on each input port of a 50:50 beam splitter are demonstrated in Fig. 2.5. As mathematically proven, the cases in Fig. 2.5(b) & (c) cancel out, for the quantum interference to happen. That is, if the two photons are in the same mode they both 'stick' together and travel either in transmitted or reflected output (Fig. 2.5 (a) & (d))

Hong *et.al* [27] proved the quantum nature of SPDC with their famous *HOM interference* experiment. In this experiment, the signal and idler in a pair are recombined at a 50:50 beam splitter with a very small delay in one with respect to the other. For zero delay, the coincidence became

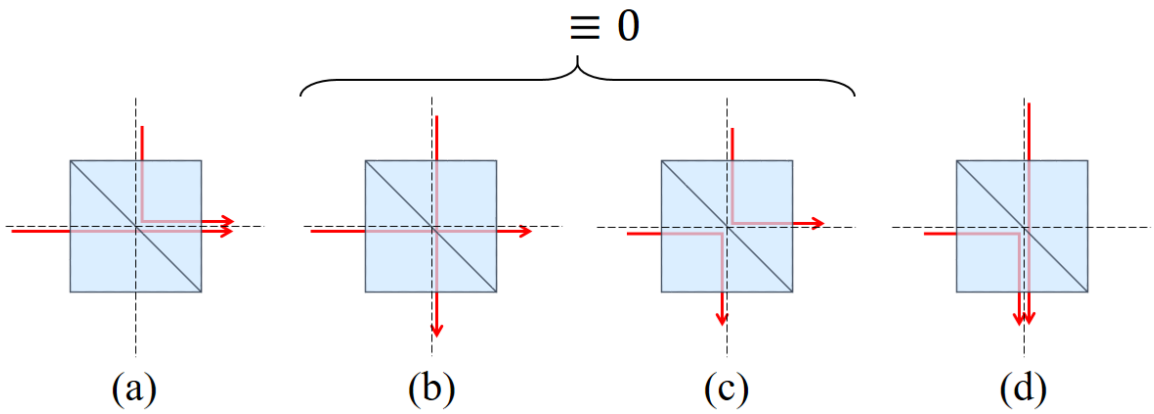

Fig. 2.5 The four possible configurations of output of two photons, one incident on each input port of a 50:50 beam splitter.

zero and for all other non-zero delays, there was a non-zero coincidence, which showed the quantum interference of two photons at a beam splitter.

2.5 Preparing Entangled States in Parametric Down Conversion

2.5.1 Polarization Entanglement

When a Type-I phase-matched crystal is pumped with a vertically polarized light, the signal and idler will have horizontal polarization. So, the joint state of SPDC photons in polarization degree of freedom is written as

$$|\psi\rangle_{\text{SPDC}} = |H\rangle_s|H\rangle_i \tag{2.39}$$

and for a horizontally polarized pump, the state becomes

$$|\psi\rangle_{\text{SPDC}} = |V\rangle_s|V\rangle_i \tag{2.40}$$

In the beginning, polarization entanglement with SPDC photons was realized using a single Type-I crystal source [1, 36]. A schematic diagram of the experiment is given in Fig. 2.6. Initially, the signal

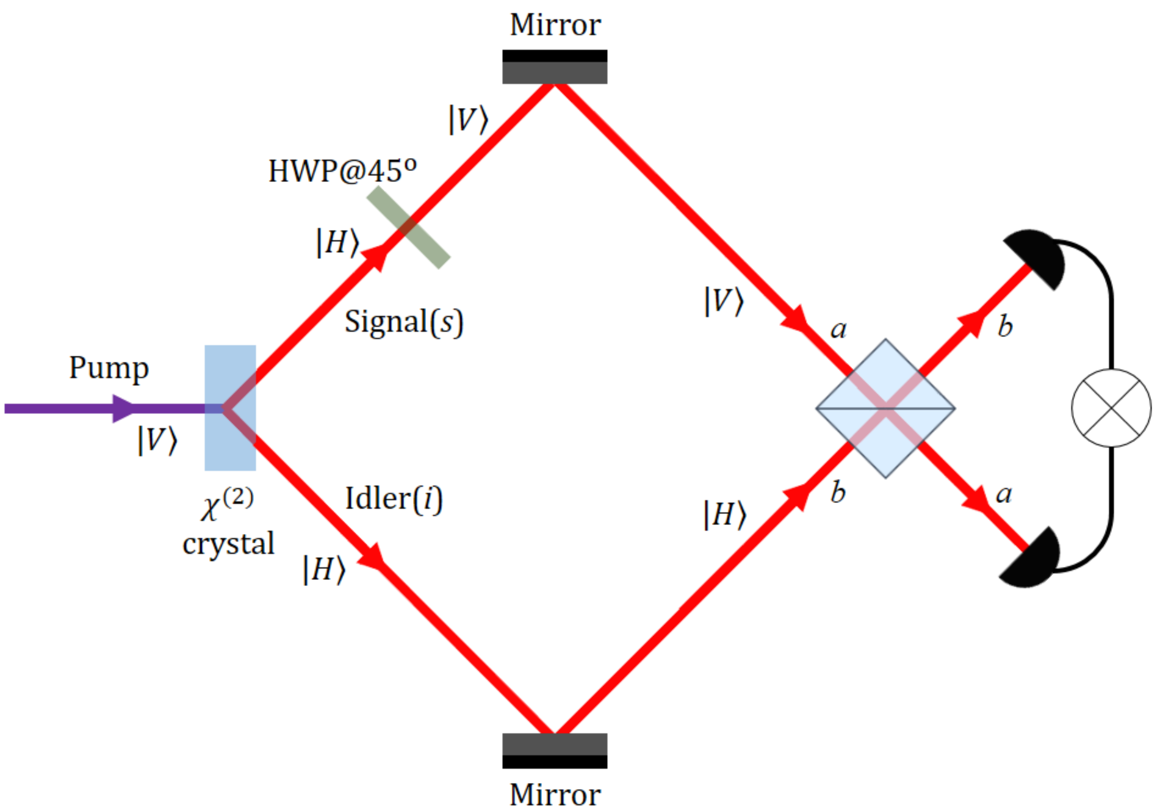

Fig. 2.6 Experimental scheme given in [1] for the generation of polarization entangled photons from SPDC using a single Type-I crystal. Here HWP - Half-wave plate.

and idler are horizontally polarized. The polarization of one photon among the pair is changed to vertical by using a half-wave plate at 45° in that photon arm. The photons from both arms are brought together to interfere at a 50:50 beam splitter. The joint polarization state at two output modes of the BS is given by

$$\begin{aligned} |\psi\rangle_{\text{SPDC}} &= \frac{1}{\sqrt{2}}(i|H\rangle_a + |H\rangle_b) \otimes (|V\rangle_a - i|V\rangle_b) \\ &= \frac{i}{\sqrt{2}}(|H\rangle_a|V\rangle_a - |H\rangle_b|V\rangle_b) + \frac{1}{\sqrt{2}}(|H\rangle_a|V\rangle_b + |H\rangle_b|V\rangle_a) \end{aligned} \tag{2.41}$$

The state given in Eqn. 2.41 is not a polarization entangled state. However, if we consider the photon pairs that are detected simultaneously at the two output ports of the BS, the final state becomes

$$|\psi\rangle = \frac{1}{\sqrt{2}}(|H\rangle_a|V\rangle_b + |H\rangle_b|V\rangle_a) \tag{2.42}$$

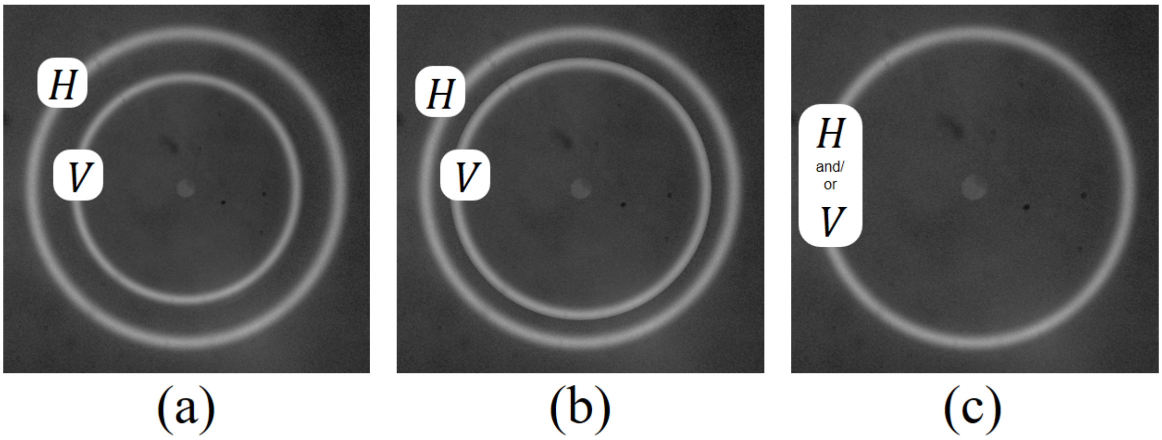

Fig. 2.7 SPDC ring distribution for two Type-I crystals stacked together. The H-polarized ring from one crystal gets overlapped to the V-polarized ring from the second crystal to give a ring distribution indistinguishable in polarization.

which is a polarization entangled state. Even though this method gives polarization entanglement, half of the signal and idler photons cannot be utilized for the entanglement, which made the scheme less popular.

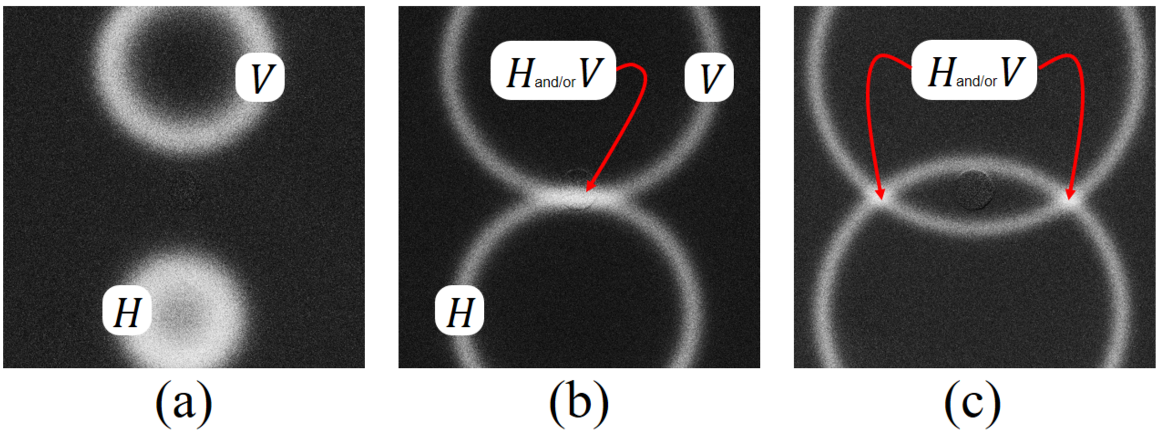

Fig. 2.8 SPDC ring distribution of Type-II crystal for (a) signal and idler separated (b) collinear and (c) non-collinear geometry.

If two Type-I crystals are stacked together with their optic axes orthogonal to each other and pumped with a diagonal (or anti-diagonal) polarization, the first crystal will down convert horizonatally polarized part in the pump and the other crystal will down convert the vertically polarized part of the pump. So, the SPDC annular distribution from both the crystals overlap each other such that one cannot distinguish from which crystal the photon is generated, and information about polarization of the photons cannot be obtained without projective measurements. The geometry of the SPDC ring for two stacked crystals is shown in Fig. 2.7. The joint polarization entangled state of SPDC with two crystals is written as

$$|\psi\rangle_{\text{SPDC}} = c_1|H\rangle_s|H\rangle_i + c_2|V\rangle_s|V\rangle_i \tag{2.43}$$

where H and V represent horizontal and vertical polarization respectively. If $c_1 = c_2 = 1/\sqrt{2}$, then the state is maximally entangled. This method of generating entangled states was first demonstrated by Kwiat *et.al.* [37].

In Type-II crystals, where the signal and idler having orthogonal polarizations, their annular distributions do not overlap one another at every point on the distribution. However, by tuning the angle of the pump with respect to the optic axes of the crystal, we can overlap signal and idler at two points on the annular ring as shown in Fig. 2.8. In collinear configuration, the two annular rings touch each other at a single point (Fig. 2.8(b)). In non-collinear configuration, the photons from a pair are situated at the two overlapping points, where the individual polarization cannot be defined (Fig. 2.8(c)). Thus the joint polarization state of signal and idler chosen from these points is given by

$$|\psi\rangle_{\text{SPDC}} = c_1|H\rangle_s|V\rangle_i + c_2|V\rangle_s|H\rangle_i. \tag{2.44}$$

Again, for $c_1 = c_2 = 1/\sqrt{2}$, the above state will become maximally entangled. Polarization entanglement using Type-II crystal source was first discussed in [38].

2.5.2 Orbital Angular Momentum Entanglement

In SPDC process, relatively very less number of photon pairs are generated from a non-linear crystal due to very low non-linear coefficient. Also, the process of generation of photon pairs in the crystal is random. With this reasons, we observe that the individual photons (signal or idler) are incoherent in nature. Along with the conservation of energy and linear momentum in an SPDC, there is conservation in orbital angular momentum (OAM) of the interacting photons [39], given as

$$l_p = l_s + l_i \tag{2.45}$$

where l_p, l_s & l_i are the OAM of pump, signal and idler respectively. The OAM conservation is coming from the fact that the angular spectrum of the pump gets transferred to the transverse correlation properties of signal and idler [40]. The OAM state of individual signal or idler photon will be

$$|\psi\rangle_{s/i} = \sum_{l_{s/i}=-\infty}^{\infty} c_{l_{s/i}} |l_{s/i}\rangle \tag{2.46}$$

which is an incoherent mixture of all OAM states. However, once the signal OAM is determined, the idler photon from the same pair will have a definite OAM, according to Eqn. 2.45. Thus the joint OAM state of signal and idler is

$$|\psi\rangle_{\text{SPDC}} = \sum_{l_s=-\infty}^{\infty} c_{l_s,l_p-l_s} |l_s\rangle |l_p - l_s\rangle \tag{2.47}$$

where c_{l_s,l_p-l_s} is the probability amplitude of the state $|l_s\rangle|l_p - l_s\rangle$. For example, when a pump beam carrying no OAM ($l_p = 0$) is considered, the above state becomes

$$\begin{aligned} |\psi\rangle_{\text{SPDC}} &= c_{0,0}|0\rangle|0\rangle \\ &+ c_{1,-1}|1\rangle|-1\rangle + c_{-1,1}|-1\rangle|1\rangle \\ &+ c_{2,-2}|2\rangle|-2\rangle + c_{-2,2}|-2\rangle|2\rangle. \end{aligned} \tag{2.48}$$

From the above state, using proper projection techniques in OAM, a biphoton state entangled in OAM can be prepared if $c_{l,-l} = c_{-l,l} = c$ for a given l. The entangled state prepared is given by

$$|\psi\rangle = c(|l\rangle|-l\rangle + |-l\rangle|l\rangle), \tag{2.49}$$

which can be normalized to get a Bell state. OAM entanglement in SPDC biphoton modes was first verified experimentally by Mair *et.al.* [31]. The analysis of OAM biphoton state in SPDC and the projection techniques are discussed further in Chapter 5.

Chapter 3

Spatial Characterization of SPDC Photons

To utilize SPDC for generating different quantum states, it is important to study the spatial profile of down converted photons and how the pump and crystal parameters affect the transverse amplitude and phase of heralded single photons. The spatial distribution of SPDC signal (or idler) photons in momentum space is termed as SPDC angular spectrum. The spatial distribution of signal in momentum space when the idler is heralded or projected into a particular mode is called as the conditional angular spectrum (CAS) of signal. Monken *et. al.* [40] theoretically and experimentally showed that the biphoton state generated in SPDC contains information about the pump. It has been experimentally verified that the amplitude as well as the phase of the pump gets transferred to the SPDC 'heralded' single photon [41]. Further, the classical non-separable state has been transferred to joint states of SPDC photon pair [42].

Although the signal photon and corresponding idler photon are correlated to each other in space, in general, there are no signal-signal or idler-idler correlations. In other words, the generated signal or idler is incoherent. In this chapter, we study the angular spectrum of SPDC with different structured pump beams. First we study the angular spectrum of SPDC with Gaussian pump and the effects of pump focusing and crystal parameters on it. We show that the inherent asymmetry of SPDC ring distribution due to pump focusing can be reduced by replacing the spherical lens with a cylindrical one and orienting lateral axis of the lens along the optic axis of the crystal. Further, we study the angular spectrum of SPDC with different structured light beams such as optical vortex beams, dark hollow beams, Bessel-Gaussian beams and perfect optical vortex beams. Even though the partial signature of pump is observed in the total angular spectrum of SPDC [43], it does not give a conclusive information about the pump mode. However, we numerically and experimentally show that the signal or idler photon mimics the amplitude distribution of the pump mode, when the individual SPDC photons are filtered from the total distribution and imaged. Phase measurements confirm that the observed distribution does not follow the transverse phase of the pump.

3.1 Joint Spatial Mode Function of SPDC Biphotons

In general, output of a parametric down conversion process is represented by a joint biphoton mode function. A biphoton mode function of momentum and frequency is derived from the quantum state of down converted output [44]. The mode function gives the information about the process such as pump beam characteristics and crystal phase matching conditions. Using the mode function, we can quantify spatial and spatio-temporal correlations among the down converted modes without actually doing the state tomography [44]. The mode function has a one-to-one correspondence with the coincidence counts that we measure in experiment.

In the perturbative treatment of spontaneous parametric down conversion process, interaction of pump (p), signal (s) and idler (i) modes in a medium (non-linear $\chi^{(2)}$ crystal) is represented by an interaction Hamiltonian, $\mathscr{H}_I$. The initial state is a vacuum state $|0\rangle_s|0\rangle_i$, therefore the output state of SPDC is approximated as

$$|\Phi\rangle \approx \left(1 - \frac{i}{\hbar}\int_0^\tau \mathscr{H}_I(t)dt\right)|0\rangle_s|0\rangle_i \tag{3.1}$$

The biphoton mode function of the generated twin photons in transverse momentum coordinates ($\mathbf{k}$) is obtained as

$$\Phi(\mathbf{k}^\perp) = \langle \mathbf{k}_s^\perp|\langle -\mathbf{k}_i^\perp|\Phi\rangle \tag{3.2}$$

where $\mathbf{k}_s^{\perp}$ and $-\mathbf{k}_i^{\perp}$ represent the transverse position in the momentum coordinates for signal and idler respectively. On simplification, the biphoton mode function in transverse momentum coordinates is given by

$$\Phi(\mathbf{k}_s^{\perp}, \mathbf{k}_i^{\perp}, \Delta k) = E_p(\mathbf{k}_p^{\perp}) L \mathrm{sinc}\left(\frac{\Delta k L}{2}\right) exp\left(i\frac{\Delta k L}{2}\right) \tag{3.3}$$

where $E_p(\mathbf{k}_p^{\perp})$ represents the pump transverse amplitude distribution, $\mathbf{k}_p^{\perp}(= \mathbf{k}_s^{\perp} + \mathbf{k}_i^{\perp})$ is the angular coordinate of the pump, $\Delta k(= k_{pz} - k_{sz} - k_{iz})$ is the longitudinal phase mismatch, and L is the thickness of the crystal. The exponential factor in Eqn. 3.3 is a global phase term.

Consider a degenerate ($2\omega_s = 2\omega_i = \omega_p = \omega$) Type-I SPDC using a β-Barium Borate (BBO) crystal of thickness L, with $e \rightarrow o + o$ phase-matching. Here, ω_x ($x = p, s, i$) are the frequencies of pump, signal and idler modes respectively. The signal (s) and idler (i) photons have ordinary polarization and the magnitude of the longitudinal wave-vector is given by their dispersion relation [45]

$$k_{s,i}^z(\mathbf{k}_{s,i}^{\perp}) = \sqrt{k_o^2 - |\mathbf{k}_{s,i}^{\perp}|^2} \tag{3.4}$$

Here $k_o = \frac{n_o \omega}{2c}$ and $n_o \equiv n_o(\omega/2)$ is the ordinary refractive index of signal/idler and c is the speed to light in vacuum. The extra-ordinary refractive index of the pump leads to the dispersion relation [45]

$$k_p^z(\mathbf{k}_s^{\perp}, \mathbf{k}_i^{\perp}) = -\beta(k_s^y + k_i^y)\sin\theta + k_{\text{eff}}\sqrt{1 - \frac{\left((k_s^x + k_i^x)^2 + (k_s^y + k_i^y)^2\right)c^2}{\omega_p^2}\eta} \tag{3.5}$$

$$\eta = \frac{1}{\varepsilon_{\perp} + \Delta\varepsilon\cos^2\theta} \tag{3.6}$$

$$n_{\text{eff}} = \sqrt{\varepsilon_{\perp}\varepsilon_{\parallel}\eta} \tag{3.7}$$

$$\beta = \eta\Delta\varepsilon\cos\theta \tag{3.8}$$

where $\Delta\varepsilon = \varepsilon_{\parallel} - \varepsilon_{\perp}$ is the difference between the parallel ($\varepsilon_{\parallel}$) and perpendicular ($\varepsilon_{\perp}$) components of permittivity coefficients with respect to the optic axis of the crystal. $\varepsilon_{\perp}$ and $\varepsilon_{\parallel}$ are related to ordinary and extra-ordinary refractive indices of the pump respectively as $\varepsilon_{\perp} = n_o^2(\lambda_p)$ and $\varepsilon_{\parallel} = n_e^2(\lambda_p)$, obtained from Sellmeier equations (Egn. 2.32 & 2.33) with wavelength of pump $\lambda_p = 405nm$.

$k_{\text{eff}} = \frac{\omega n_{\text{eff}}}{c}$ is the magnitude of the wave-vector of extra-ordinary pump wave. θ is the angle of pump propagation direction with respect to the optic axis defined by the vector, $\mathbf{a} = (0, \sin\theta, \cos\theta)$. θ is also called as the cut angle of the crystal. The term β describes the walk-off effect, the deviation of Poynting vector from the pump direction [46], which is one of the reasons for the asymmetry in SPDC annular distribution. The term η explains astigmatic effects [47]. The phase mismatch is then given by

$$\Delta k(\mathbf{k}_s^{\perp}, \mathbf{k}_i^{\perp}) = k_p^z(\mathbf{k}_s^{\perp}, \mathbf{k}_i^{\perp}) - k_s^z(\mathbf{k}_s^{\perp}) - k_i^z(\mathbf{k}_i^{\perp}) \tag{3.9}$$

To find an approximate expression for Δk, we expand the right-had side of Eqn. 3.9 in Taylor series and truncate to first order. On simplification, the phase mismatch is rewritten as

$$\Delta k(\mathbf{k}_s^{\perp}, \mathbf{k}_i^{\perp}) \approx k_{\text{eff}} - 2k_o - \frac{k_{sx}k_{ix} + k_{sy}k_{iy}}{k_o} - \beta \sin\theta (k_{sy} + k_{iy}) \tag{3.10}$$

3.2 Angular Spectrum of SPDC

The generated signal and idler photons in SPDC propagate in space according to the phase matching condition given in Eqn. 2.26. The locus of all points in space that satisfies phase-matching condition comes out to be an annular ring distribution where the signal and idler photons in a pair are present. The angular spectrum of the down converted signal photons for frequency, ω_s, is obtained by tracing the biphoton mode function over all idler photons [45]

$$R_s(\mathbf{k}_s^{\perp}) = \int d\mathbf{k}_i^{\perp} |\Phi(\mathbf{k}_s^{\perp}, \mathbf{k}_i^{\perp}, \Delta k)|^2. \tag{3.11}$$

The above equation is used to calculate angular spectrum for Type I SPDC in β-Barium Borate (BBO) crystal (cut angle 29.97°) for pump wavelength 405 nm and plotted in momentum space. The observed spectrum is ring-shaped as expected. It is already observed that ring width of the spectrum depends on input pump beam radius, cut angle and thickness of the crystal [48, 45]. It has been also studied in Ref. [45] that a small pump beam can generate asymmetry in spectrum. Therefore the pump beam radius is kept as large as possible, which is around $700\mu m$, to avoid this asymmetry.

The basic experimental setup to record the angular spectrum of SPDC with different pump beams is shown in Fig. 3.1. A pump beam of wavelength $(405 \pm 2)nm$ from a continuous-wave diode laser (TOPTICA iBeam Smart) of $50mW$ power, is incident on a $\chi^{(2)}$ crystal. The dashed box corresponds to the case-by-case method to prepare pump beams of different spatial characteristics, which are given in the sections below. A half-wave plate (HWP) is used to orient the pump polarization along the optic axis of the crystal. We use Type-I β-Barium Borate (BBO) crystals to generate SPDC. The

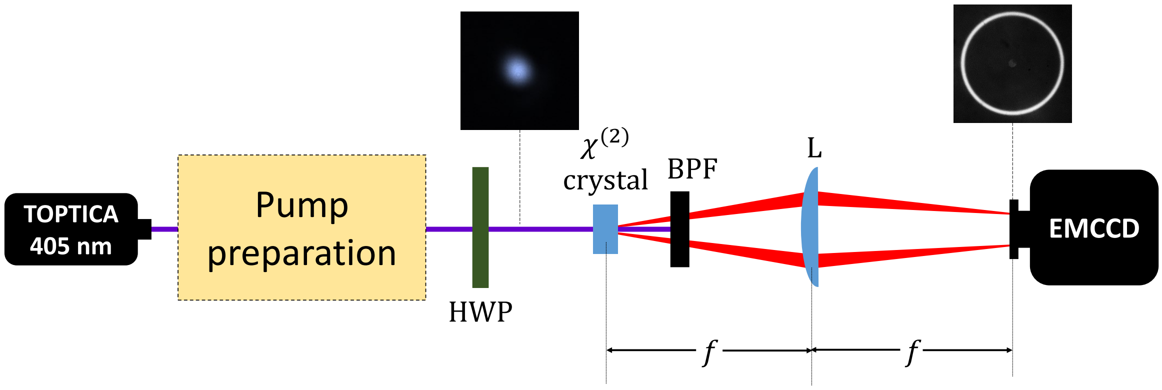

Fig. 3.1 Experimental setup to record the angular spectrum of SPDC photons generated by pumping a non-linear crystal with different pump beams.Figures in inset are the images of a Gaussian pump and the corresponding SPDC annular distribution in the angular spectrum.

down converted photons (signal & idler) of wavelength 810 nm each (degenerate) are generated in a non-collinear fashion at diametrically opposite points of the SPDC ring. A bandpass filter (BPF) of central wavelength 810 ± 5 nm is used to filter down converted photons and block the unconverted pump beam after the crystal. A $2f$-imaging configuration with a plano-convex lens (L) of focal length 50mm is used to image the SPDC in **k**-space. The angular spectrum of SPDC is recorded using an EMCCD camera with a gain x100 and the addition of 100 frames each having exposure time of 0.5 s. The EMCCD camera has an imaging area of 512×512 pixels with a pixel size of 16 μm. The angular spectrum of SPDC shown in figures throughout the chapter are recorded using $2f$-imaging with a plano-convex lens (L) of focal length 50 mm.

3.2.1 Angular Spectrum with Gaussian pump

Most of the commercial lasers used in optics laboratory give an output field amplitude as a fundamental TEM_{00} mode. A typical field amplitude of a Gaussian beam is given as [49]

$$E_p(x,y,z) = E_0 \frac{w_0}{w(z)} \exp[-\frac{r^2}{w^2(z)}] \exp[-i\frac{kr^2}{2R(z)}] \exp(-i[kz - \phi(z)]) \tag{3.12}$$

where $w(z)$ is the radius of the beam at a distance z from the waist position having radius w_0. k is the wave number, $R(z)$ is the radius of curvature of the wave-front and $\phi(z)$ is the z-dependent Gouy phase. The parameters w_0, $w(z)$, $R(z)$ and $\phi(z)$ are related to the Rayleigh range z_R as

$$w(z) = w_0 \sqrt{1 + (\frac{z}{z_R})^2}, \tag{3.13}$$

$$R(z) = z + \frac{z_R^2}{z}, \tag{3.14}$$

$$\phi(z) = \arctan\left(\frac{z}{z_R}\right). \tag{3.15}$$

The effect of tuning the angle of pump with respect to the optic axis is shown in Fig. 3.2. Here, $\Delta\theta$ is the increment/decrement in the angle of pump with respect to optic axis of the crystal.

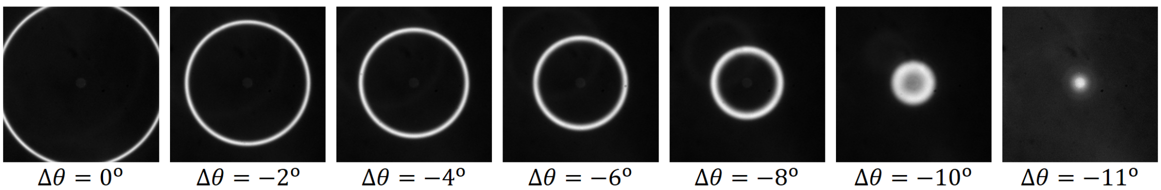

Fig. 3.2 Angular spectra of SPDC generated by pumping a Type-I BBO crystal of thickness 5mm with a Gaussian beam and the angle of pump with respect to optic axis.

To study the effect of pump focusing on the angular spectrum, we recorded the AS for different focusing conditions. Fig. 3.3 shows the numerical and experimental angular spectra of SPDC generated by pumping a Gaussian beam focused at the crystal using lenses of focal lengths 50, 100, 150, 200, 300, 400, 500 & 750 mm. Focusing of pump using a lens introduces asymmetry in the SPDC annular ring. Asymmetry is more for a tightly focused pump.

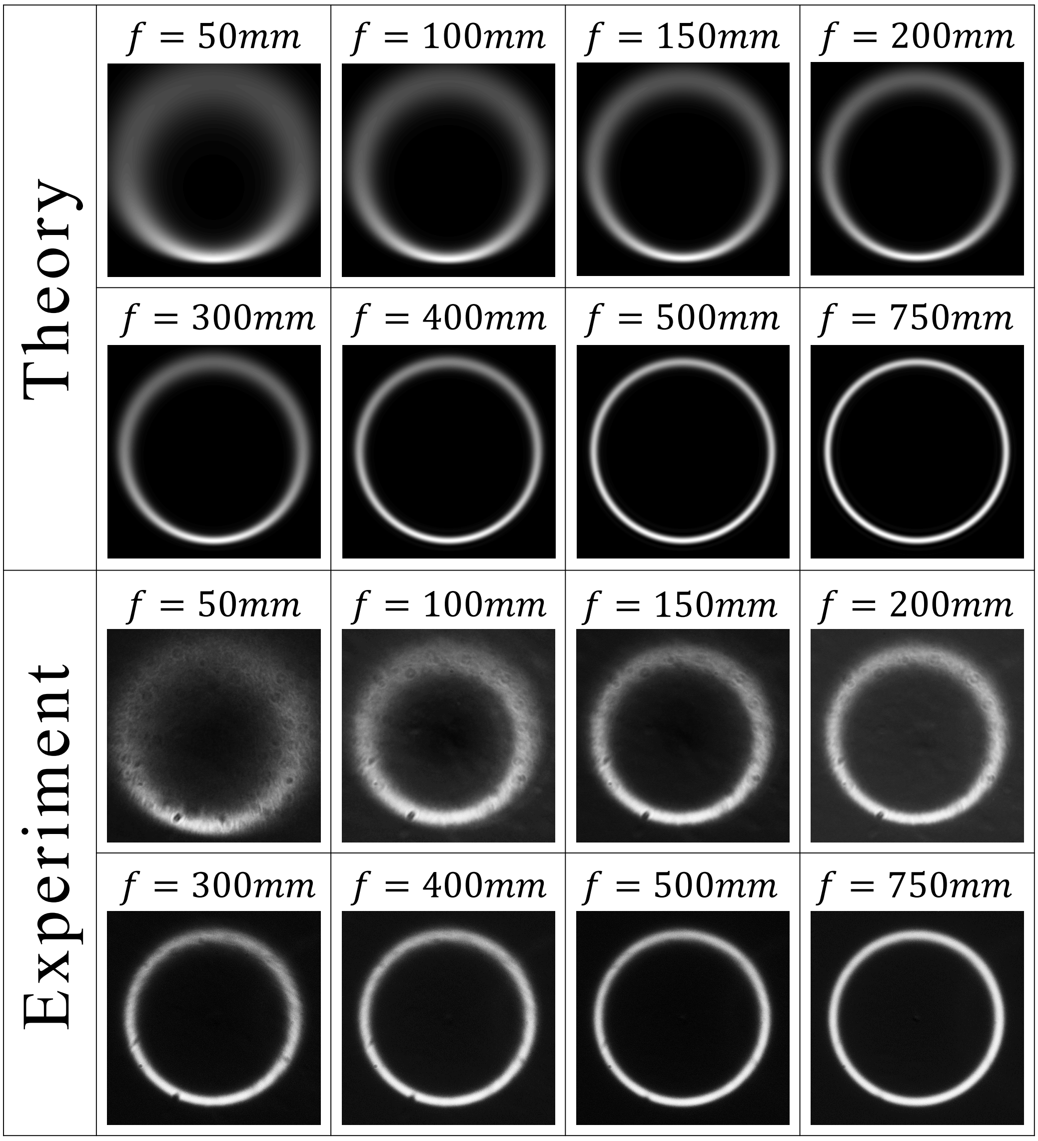

Fig. 3.3 Numerical and experimental angular spectra of SPDC generated by pumping a Type-I BBO crystal of thickness 2mm with a Gaussian beam focused at the crystal plane.

We recorded the angular spectrum of Type-I BBO crystals having thicknesses 2 mm, 5 mm and 10 mm (Fig. 3.4) pumped with a Gaussian beam focused at the crystal using a lens of focal length 100 mm (Top row of Fig. 3.4) as well as a collimated beam (Bottom row of Fig. 3.4). The annular ring width of SPDC decreases as the crystal length increases, as seen from the images. Focusing of the pump onto a thin crystal increases the ring width as well as asymmetry in the SPDC distribution. This asymmetry is less in the case of pumping a focused beam onto a thicker crystal.

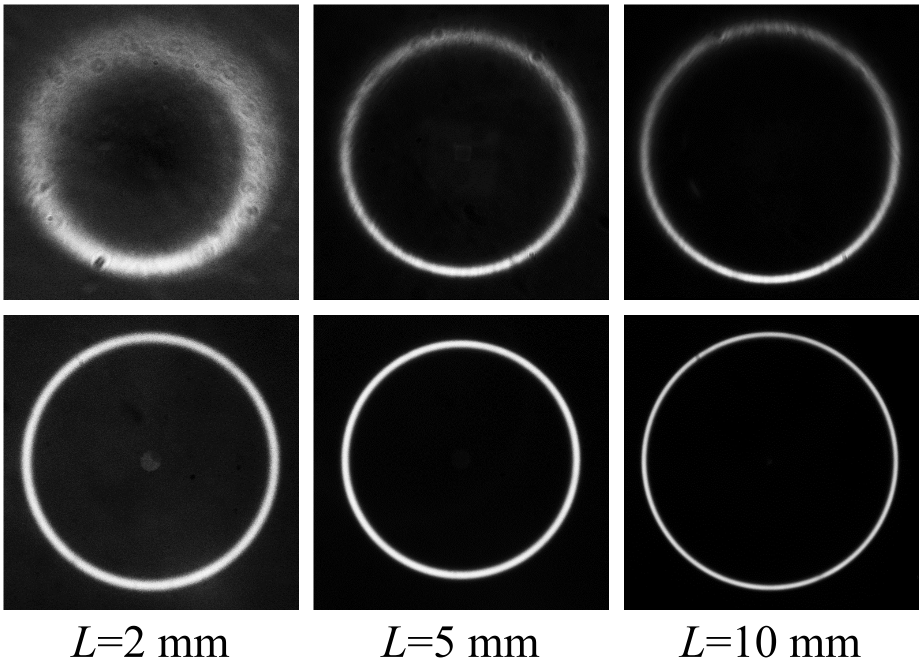

Fig. 3.4 Experimental angular spectra of SPDC generated by pumping a Type-I BBO crystal of thicknesses 2mm, 5mm and 10mm pump with a Gaussian beam focused at the crystal plane using 100mm lens (Top row), and collimated (Bottom row).

We studied the effect of ellipticity of the Gaussian beam on the SPDC angular spectrum. We generated elliptic Gaussian beams in the pump using cylindrical lenses. The action of a cylindrical lens makes the circular Gaussian beam elliptical. Figure. 3.5 & 3.6 show the numerical and experimental images of pump and SPDC for the case of pumping a Type-I BBO of 2mm thickness with elliptical Gaussian beams generated using 50mm and 200mm cylindrical lenses, respectively. Figure. 3.7 & 3.8 show the numerical and experimental images of pump and SPDC for the case of pumping a Type-I BBO of 5 mm thickness with elliptical Gaussian beams generated using 50 mm and 200 mm cylindrical lenses, respectively.

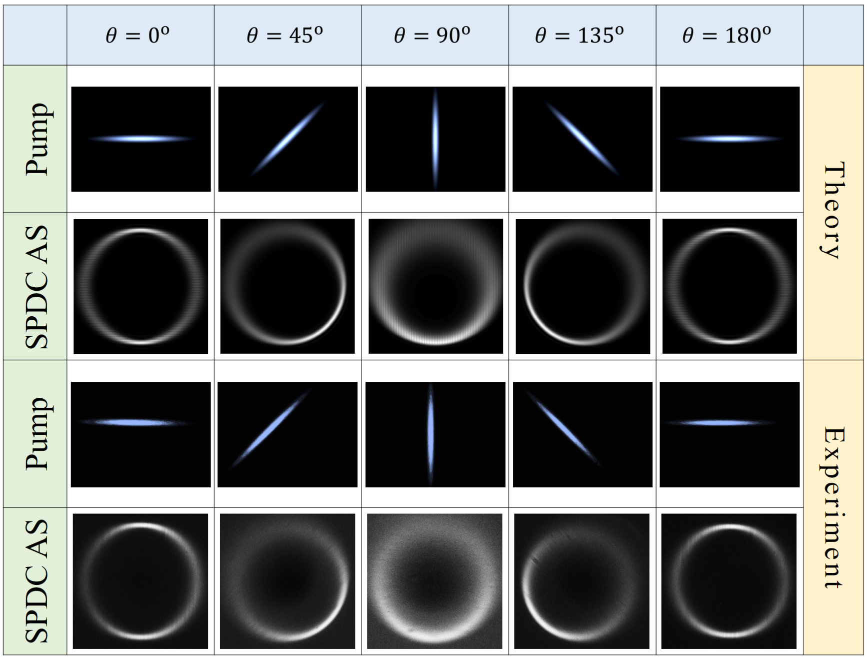

Fig. 3.5 Numerical and experimental angular spectra of SPDC generated by pumping a Type-I BBO crystal of thickness 2 mm with a Gaussian beam focused at the crystal plane using 50 mm cylindrical lens.

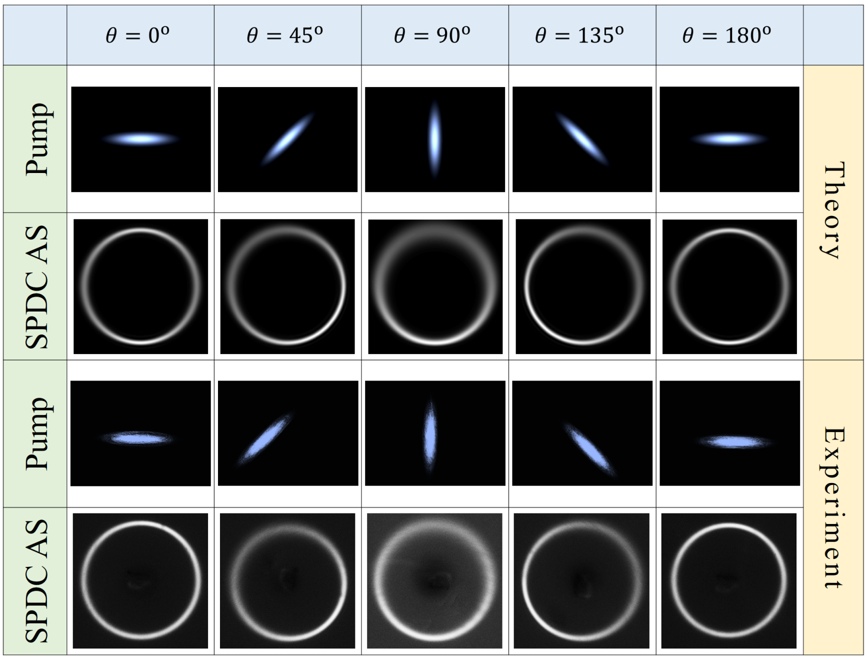

Fig. 3.6 Numerical and experimental angular spectra of SPDC generated by pumping a Type-I BBO crystal of thickness 2 mm with a Gaussian beam focused at the crystal plane using 200 mm cylindrical lens.

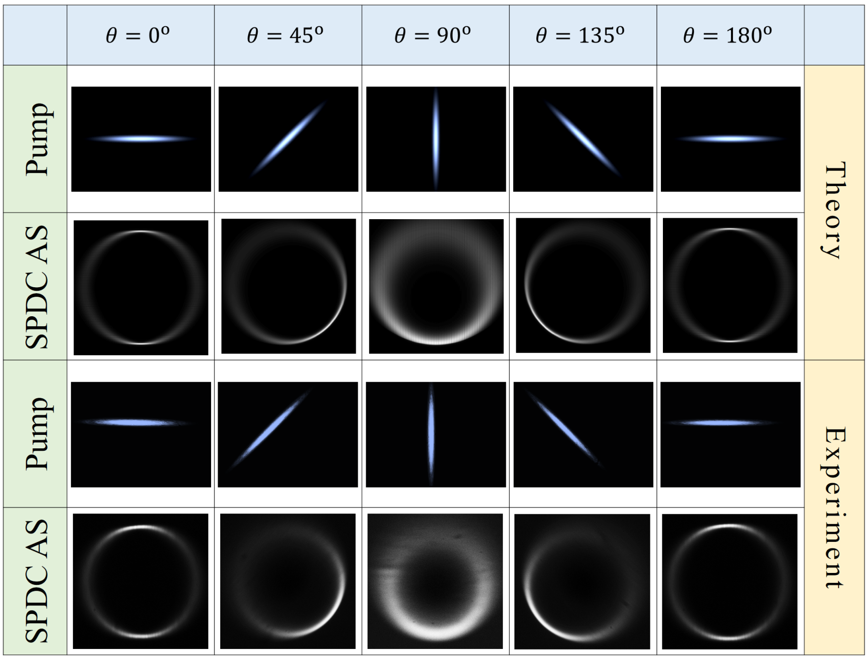

Fig. 3.7 Numerical and experimental angular spectra of SPDC generated by pumping a Type-I BBO crystal of thickness 5 mm with a Gaussian beam focused at the crystal plane using 50 mm cylindrical lens.

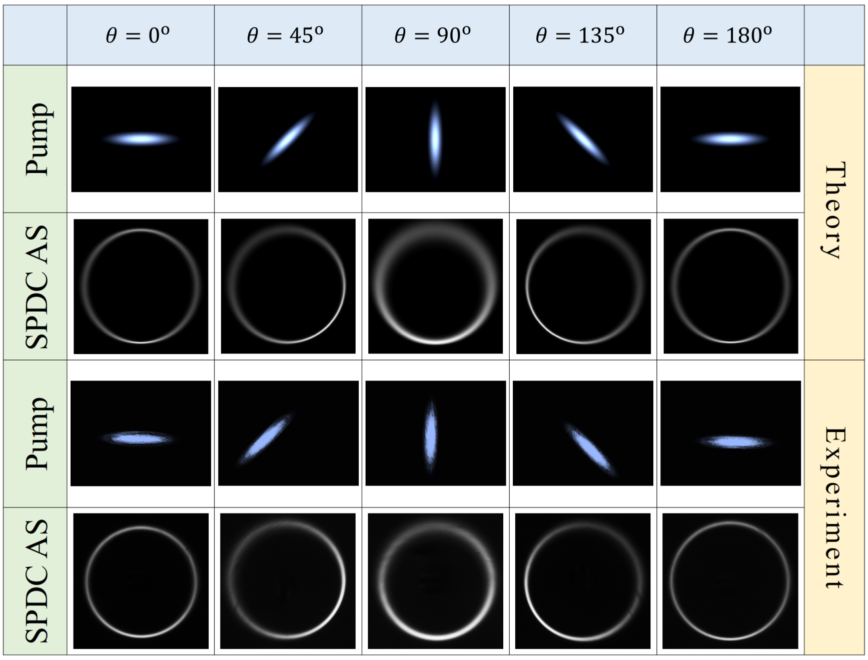

Fig. 3.8 Numerical and experimental angular spectra of SPDC generated by pumping a Type-I BBO crystal of thickness 5 mm with a Gaussian beam focused at the crystal plane using 200 mm cylindrical lens.

3.2.2 Angular Spectrum with optical vortex pump

Optical vortex, a light beam having doughnut-like transverse intensity distribution, is a class of structured light beams carrying orbital angular momentum. Unlike a Gaussian beam having uniform

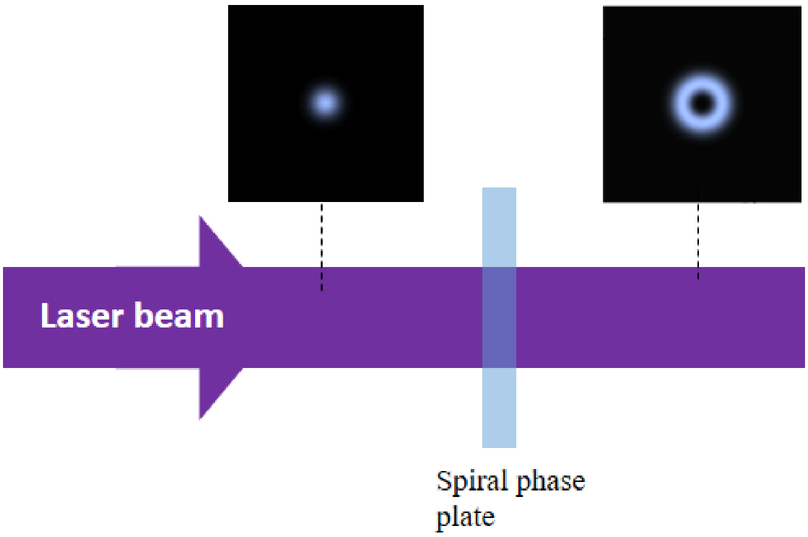

Fig. 3.9 Experimental setup to generate optical vortex from Gaussian beam using spiral phase plate.

phase distribution, the transverse phase of a vortex beam varies azimuthally from zero to maximum in steps of $2\pi l$, which gives an orbital angular momentum $l\hbar$ per photon to the beam. A typical electric field distribution of an optical vortex can be written as [50]

$$\begin{aligned} E_p(x,y) &= \left(\frac{x+iy}{w_g}\right)^l \exp\left(-\frac{x^2+y^2}{w_g^2}\right) \\ &= \underbrace{\left(\frac{r}{w_g}\right)^l}_{\text{`size effect'}} \underbrace{\exp(il\theta)}_{\text{azimuthal phase}} \underbrace{\exp\left(-\frac{r^2}{w_g^2}\right)}_{\text{Gaussian envelope}} \end{aligned} \tag{3.16}$$

where $r = \sqrt{x^2+y^2}$ and $\theta = \tan^{-1}(y/x)$.

As shown in Fig. 3.9, we experimentally generated optical vortex beam of order l by passing a Gaussian beam through a spiral phase plate (vortex lens) of order l. The generated optical vortex is pumped to Type-I BBO crystal of thickness 5mm. Figure 3.10 shows the numerical and experimental images of pump and SPDC AS for orders 0, 1, 2 & 3. As the order of the vortex increases, the

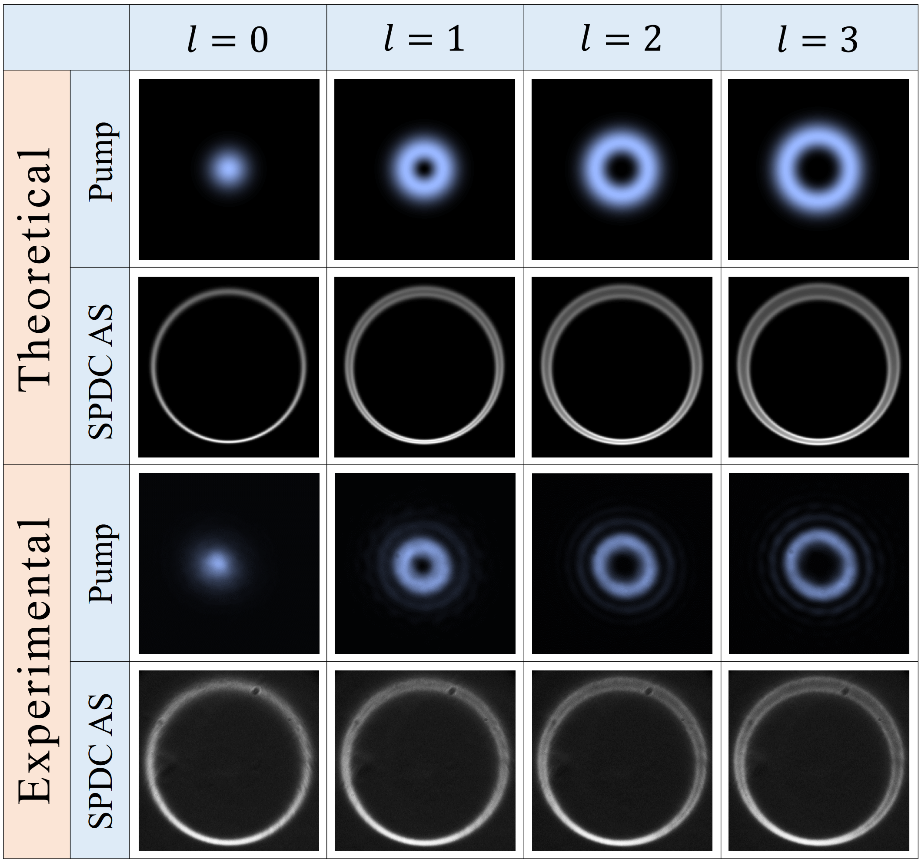

Fig. 3.10 Numerical and experimental images of pump and angular spectra of SPDC photons generated by pumping optical vortex beam of azhimuthal order l to a Type-I BBO crystal of thickness 2mm.

radius of the doughnut distribution increases. For a normal optical vortex pump, the SPDC annular distribution will look like a double ring and the distance between two peaks increases with the order of the pump vortex. The asymmetry in the SPDC distribution is due to the larger spatial walk-off within the thick crystal used.

3.2.3 Angular Spectrum with Bessel-Gaussian pump

Most of the light beams used in laboratory show diffraction effects during their propagation in free-space, which is undesirable for most of the cases. It was predicted earlier that there exist some non-diffracting solutions to paraxial-wave equation [51]. Bessel beams are a class of such beams that exhibit non-diffracting nature [52] as well as self-healing property [53], when propagated in space. The field distribution of a Bessel beam is written as

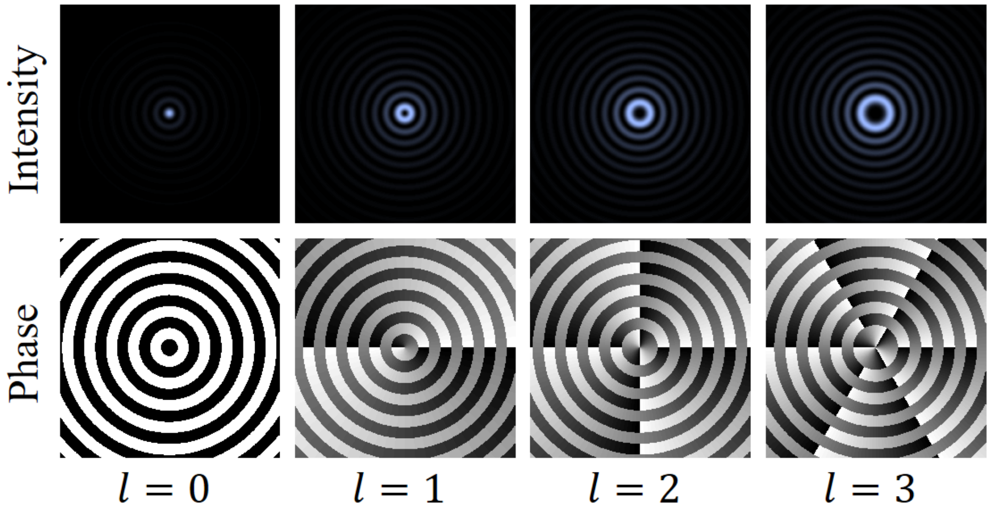

Fig. 3.11 Intensity and transverse phase distribution of Bessel-Gaussian modes of orders 0,1,2 & 3.

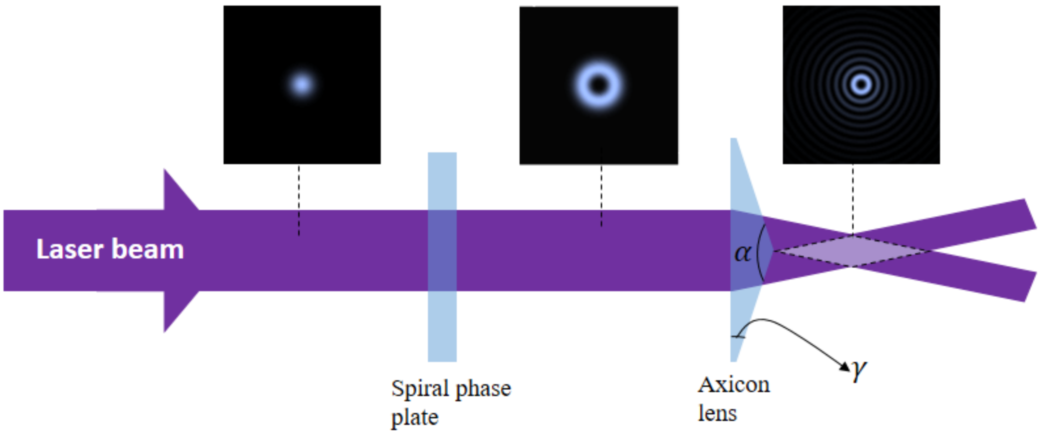

Fig. 3.12 Experimental setup to generate Bessel-Gaussian beam of different orders using spiral phase plate (SPP) and an axicon lens.

$$E(r,\phi,z) = J_l(k_r r)\exp(ik_z z)\exp(il\phi) \tag{3.17}$$

where J_l is the l^{th} order Bessel function of first kind. k_r and k_z are the radial and longitudinal wave-vectors respectively, with $k = \sqrt{k_r^2 + k_z^2}$. Bessel beams of non-zero l-values have orbital angular momentum $l\hbar$ due to the presence of azimuthal phase term in Eqn. 3.17. Ideally, a Bessel beam will have infinite rings in the spatial profile, which cannot be realized in practice. In most of the practical cases, Bessel beams are generated on Gaussian envelope, which are called as Bessel-Gaussian (BG)

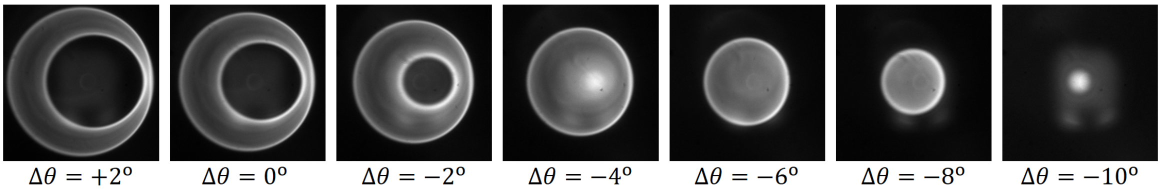

Fig. 3.13 Effect of angle of pump beam with respect to the optic axis, on SPDC angular spectrum. The pump is a zeroth order Bessel-Guassian beam.

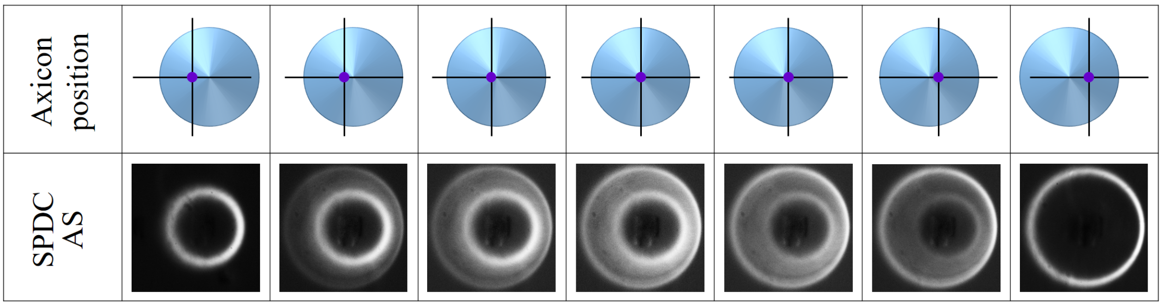

Fig. 3.14 Angular spectrum of SPDC of Bessel-Gaussian pump with the lateral shift of axicon with respect to the beam axis of the pump.

beams [54]. The field expression for a BG beam can be written as

$$E(r,\phi,z) = J_l(k_r r)\exp\left(-\frac{r^2}{w_g^2}\right)\exp(il\phi) \tag{3.18}$$

Figure 3.11 shows the intensity and transverse phase distribution of BG beams of orders 0, 1, 2 & 3. The generated BG beams are generally truncated to a certain spatial extent. Truncated Bessel beams are experimentally generated by passing a Gaussian beam through the center of an axicon lens (or a conical lens). Figure 3.12 depicts the experimental setup to generate BG beams using axicon. A Gaussian beam is passed through the axicon which creates two wavefronts from two parts of the beam. The two wavefronts start combining just after the axicon and the intensity at the center of the BG beam increases when propagated away from the axicon, to maximum. The intensity decreases on further propagation and distribution becomes an annular ring at larger distances.

The angular spectrum of SPDC with a BG pump will have a broad asymmetric ring distribution with higher photon densities at the boundaries of the ring. Figure 3.13 shows the effect of tuning angle of the crystal on the SPDC angular spectrum with a zeroth order BG pump beam. Here $\Delta\theta$ is the increment/decrement in the angle of the pump with respect to the optic axis. Next, to study the

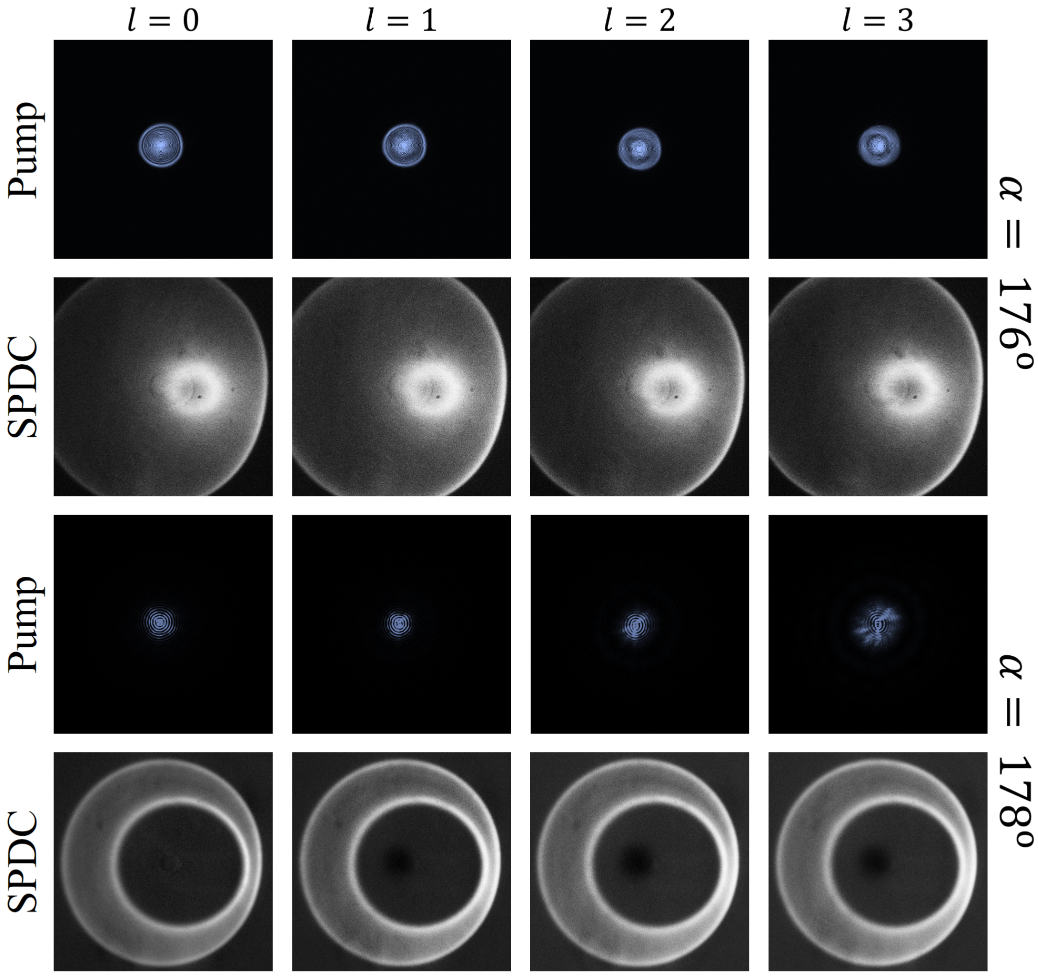

Fig. 3.15 Angular spectrum of SPDC for BG pump with different orders and for axicon having apex angles 176^o and 178^o.

effect of lateral shift of axicon lens with respect the beam axis on the angular spectrum, we recorded the SPDC angular spectrum for different shift positions, as shown in Fig. 3.14.

When the initial Gaussian beam is completely away from the center of axicon towards left, the angular spectrum shows the smaller ring at the inner boundary of the total distribution. When the pump beam shifts towards right, the angular spectrum shows bigger ring at the outer boundary of the total distribution. As the beam is moved towards the center of the axicon, both the rings appear together with a non-zero intensity in the space between the rings. The sizes of the two rings are different because the pump beam from left and right 'sees' the crystal at two different angles with respect to the optic axis.

The angular spectrum of SPDC is recorded for BG pump with two different axicons having apex angles 176^o and 178^o. The images for different OAM values are shown in Fig. 3.15. The angular spectrum remains the same for higher order BG pump. The annular ring of SPDC become smaller as the apex angle of the axicon is increased.

3.2.4 Angular Spectrum with perfect optical vortex pump

Conventional optical vortices have their limitations in applications involving transmission of OAM modes through optical fibers [55, 56] in communication [57], as the size of the optical vortex strongly depends on its topological charge [58]. Due to this, projective measurements based on 'phase-flattening' technique become difficult for higher order OAM modes [59]. A new class of optical vortex beam, termed as 'perfect optical vortex', was introduced by Ostrovsky *et.al.* that solves size effects of a normal vortex [60]. Conventionally, perfect optical vortices of order l are formed as a Fourier transform of Bessel-Gaussian beam of order l [61].

The field amplitude of a typical perfect optical vortex of order l is given as

$$E(r,\theta) = i^{l-1}\frac{w_g}{w_o} exp(il\theta)\exp\left(-\frac{(r^2+r_r^2)}{w_o^2}\right) I_l\left(\frac{2r_r r}{w_o^2}\right) \tag{3.19}$$

where w_g is the waist radius of the initial Gaussian beam, $w_o = 2f/kw_g$ is half of the ring width

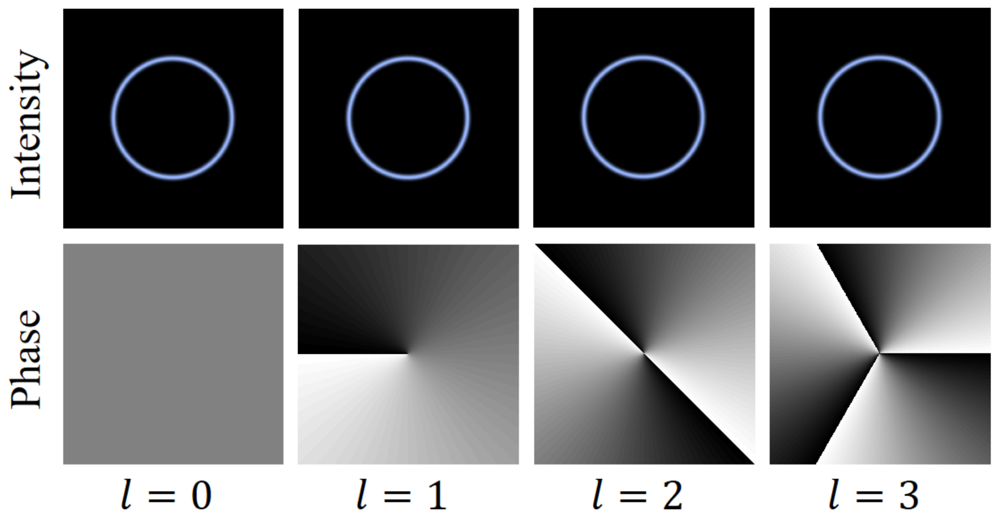

Fig. 3.16 Intensity and phase distribution of perfect optical vortex modes of orders 0, 1, 2 & 3.

and r_r is radius of the ring. Here f is the focal length of the Fourier lens and k is the magnitude of

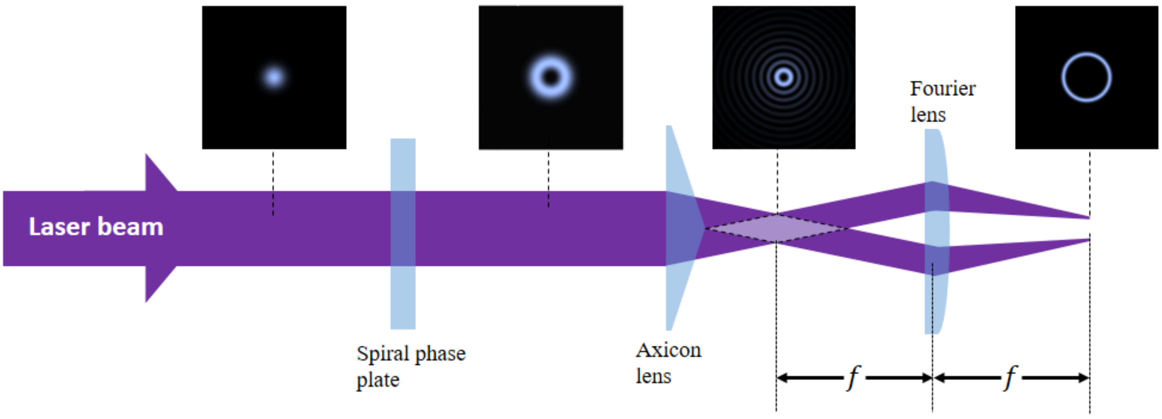

Fig. 3.17 Experimental setup to generate perfect optical vortex beam by the Fourier transformation of a Bessel-Gaussian beam.

the wave-vector of the light beam. Fig. 3.16 shows the intensity and transverse phase distribution of perfect vortex modes of different orders. The size of POV ring distribution remains the same for higher OAM values. In experiment, we generated POV beams of different orders by taking an optical Fourier transform of BG beam, which is given as in Fig. 3.17. We recorded the angular spectrum of

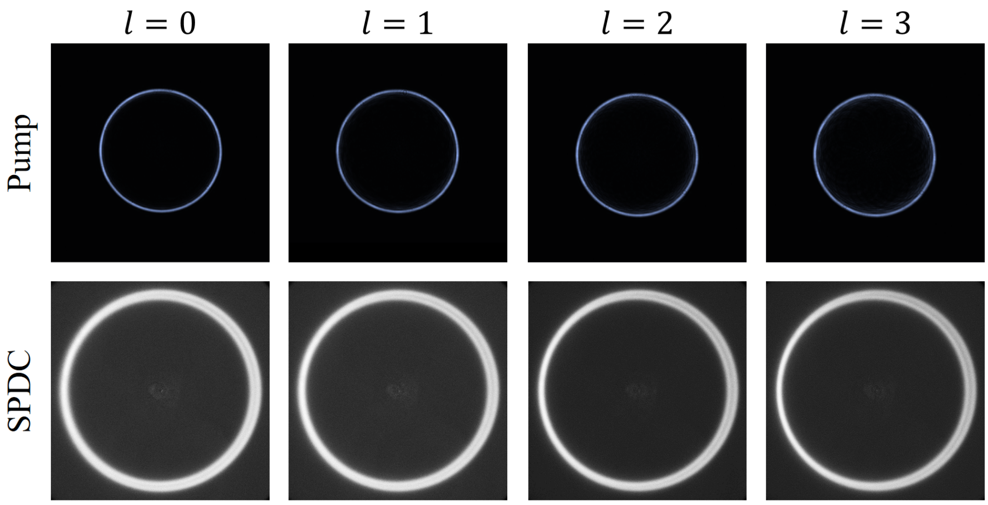

Fig. 3.18 Angular spectra of SPDC generated using perfect optical vortex beam of different orders. Top row shows the images of pump POV mode.

SPDC for POV beams of different orders. The recorded images of pump and SPDC is given in Fig. 3.18. Since the size of POV is independent of the order of the vortex, the angular spectrum of SPDC is identical for higher OAM values, just as in the case of SPDC with BG modes. The asymmetry in the angular spectrum is mainly due to the spatial walk-off of the thick crystal used.

3.2.5 Angular Spectrum with dark hollow pump

Dark hollow beams (DHB) are a class of laser beams having ring-like intensity distribution and a uniform transverse phase profile. DHBs find applications mainly in cooling and trapping of atoms [62]. DHBs can be generated using axicons [63], multimode light guides [64] and spiral phase plates [65]. Partially coherent hollow beams can be generated using multimode fibers [66]. DHBs are also generated from random light sources [67]. Intensity distribution of a typical DHB is given in cylindrical coordinates as [62]

$$I(r,z) = \frac{I_0}{\sqrt{2}\pi r_r w(z)} \left[\exp\left(-\frac{2(r+r_r)^2}{[w(z)]^2} \right) + \exp\left(-\frac{2(r-r_r)^2}{[w(z)]^2} \right) \right] \tag{3.20}$$

where $2r_r$ is the distance between two diametrically opposite peaks on the ring distribution. Here, we consider the ring-shaped DHB formed in the far-field of zeroth order Bessel-Gaussian beam, as pump. The field distribution of the beam is [61]

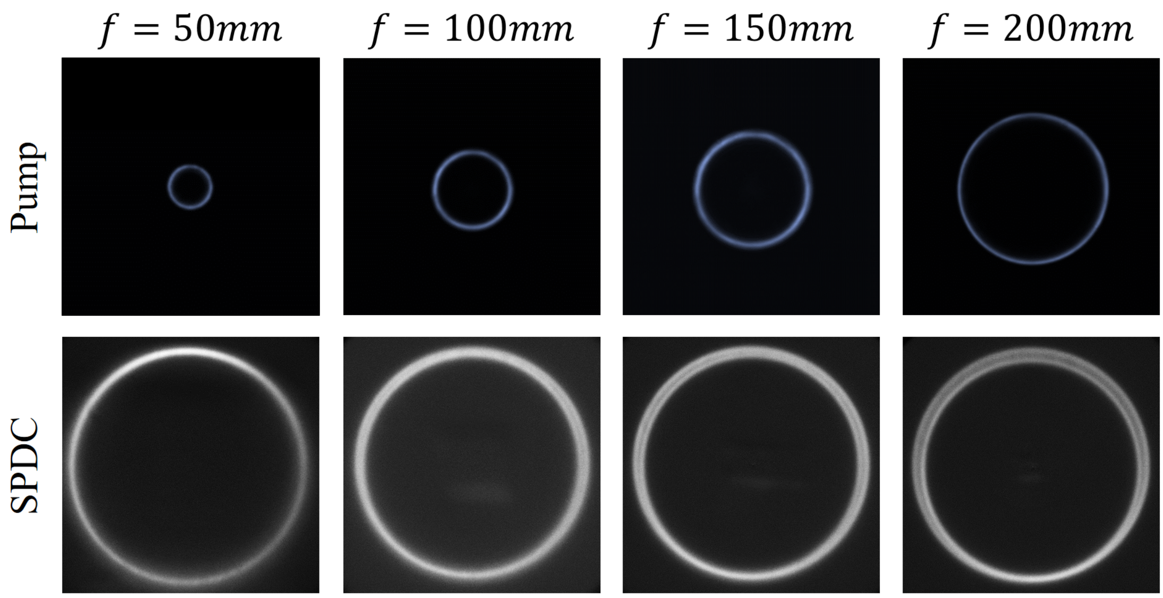

Fig. 3.19 Angular spectra of SPDC generated using dark hollow beam of different ring radii, generated using different Fourier lenses. Top row shows the images of pump DHB mode.

$$E(r,\theta) = \frac{w_g}{2i\sqrt{\pi}r_r r} \exp\left(-\frac{(r^2+r_r^2)}{w_o^2}\right) \exp\left(\frac{2r_r r}{w_o^2}\right) \tag{3.21}$$

where $2w_o$ and r_r are the ring width and radius respectively. $w_o = 2f/kw_g$ where w_g is the radius of the initial Gaussian beam, and f is focal length of the lens used to image the pump in far-field. $k = 2\pi/\lambda$ is the wave-vector amplitude of the light of wavelength λ.

We generate dark hollow beams using the configuration given in Fig. 3.17, but without any spiral phase plate. The size of the ring is varied by changing the focal length of the lens. Fig. 3.18 shows the angular spectra of SPDC for DHBs of different ring radii, generated by changing the focal length of the Fourier lens. Here, f is the focal length of the Fourier lens used.

3.3 Effect of Spatial Filtering on Angular Spectrum of SPDC

In general, the spatial distribution of individual photons (signal or idler) generated by spontaneous parametric down conversion (SPDC) does not evidently show any particular spatial mode structure because of their randomness in generation and the incoherent nature. Here, we numerically showed that all individual photons generated by SPDC process carry the transverse amplitude as that of the pump and then confirmed it experimentally. The pump amplitude is revealed in SPDC when individual photons are spatially filtered from the total SPDC distribution. This is observed simply by imaging the photons that are filtered using a minimum-sized aperture. Phase measurements showed that the observed mode distribution does not possess the transverse phase distribution as that of the pump.

The angular spectrum (AS) and the conditional angular spectrum (CAS) of SPDC photons are highly dependent on the angular spectrum of the pump beam and crystal parameters [48, 43]. It has been experimentally shown that the angular spectrum of the pump beam gets transferred to the twin photons generated in SPDC [40]. For example, it was shown that the amplitude as well as the helical phase of an optical vortex pump is transferred to the SPDC heralded single photon [41]. The helical phase of the single photon was verified by methods like triangular aperture diffraction [41] and interferometry [68]. It was also observed that the SPDC heralded single photons generated with

Bessel-Guassian pump show non-diffracting behaviour over a longer distance [69]. So, images of high contrast and resolution can be obtained at any distance from the light source by using heralded single photons [70]. Due to the incoherence of individual parametric down converted photons, their angular spectrum does not evidently show the signature of spatial properties of the pump.

3.3.1 Numerical Analysis

The angular spectrum of SPDC is calculated from the expression given in Eqn. 3.11. Here, the spatial distribution of the pump has been taken as Laguerre Gaussian (LG) modes with zero radial number which represent optical vortices [71]. The different coaxial superposition of vortices is obtained by

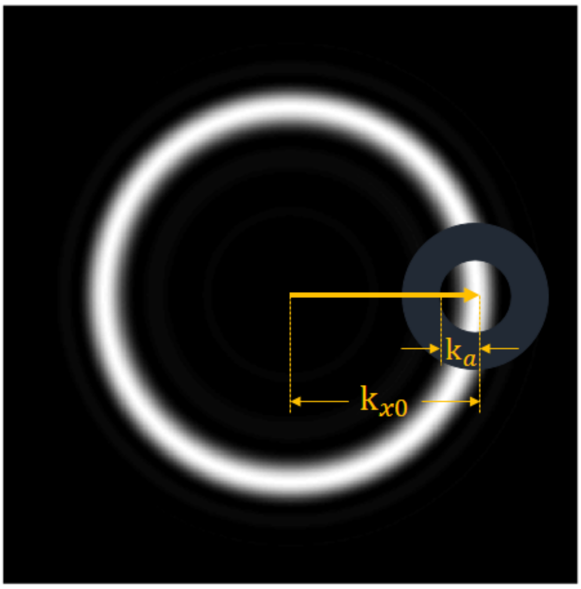

Fig. 3.20 Geometrical representation of an aperture placed on the SPDC annular distribution.

the addition and subtraction of the above field for different l values. To select photons from SPDC distribution, a circular aperture is placed at on portion of total SPDC annular ring, as shown in Fig. 3.20. The geometry of the aperture in signal coordinates $\mathbf{k}_s^{\perp} \equiv (k_{sx}, k_{sy})$, is given by the function

$$A(\mathbf{k}_s^{\perp}) = \begin{cases} 1, & \text{if} \sqrt{(k_{sx}-k_{x0})^2 + k_{sy}^2} \leq k_a \\ 0, & \text{if} \sqrt{(k_{sx}-k_{x0})^2 + k_{sy}^2} > k_a \end{cases}$$

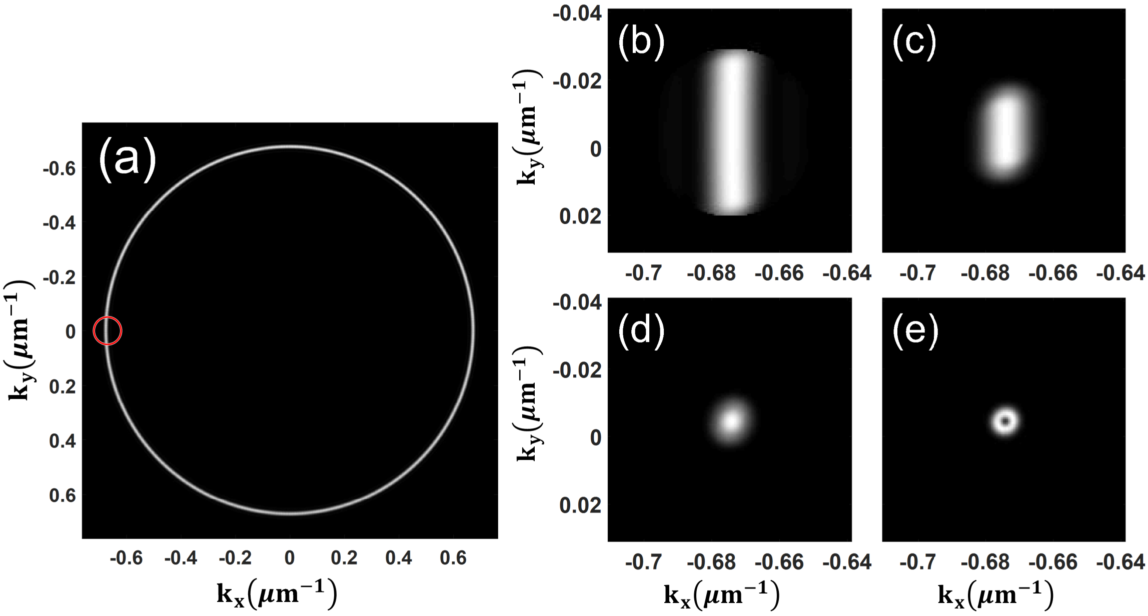

Fig. 3.21 a) Numerical total angular spectrum of SPDC for vortex beam ($l = 1$) as a pump, plotted in momentum coordinates. (b)-(e) Numerical angular spectrum of parametric down converted photons with gradual closure of the aperture on a portion of total distribution (circled in red) to a diameter of (b) 593 μm (c) 320 μm (d) 128 μm (e) 24 μm.

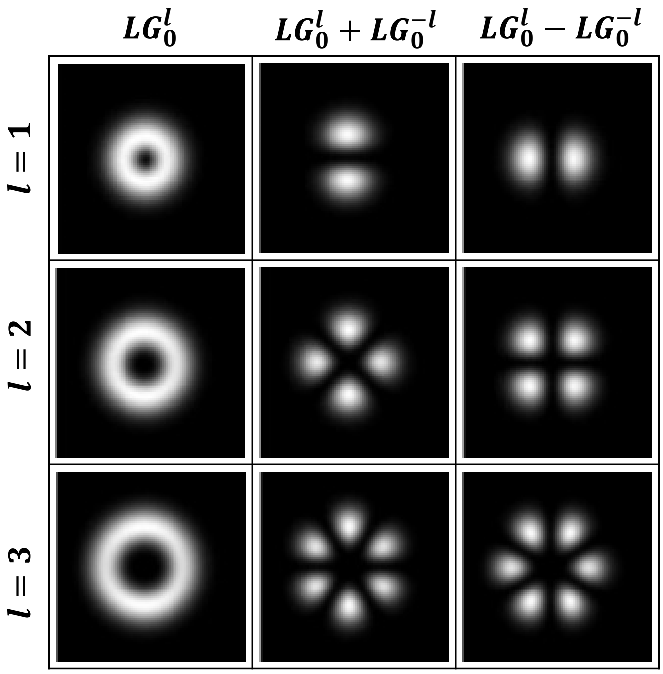

Fig. 3.22 Magnified images of numerical angular spectrum of spatially filtered parametric down converted photons when the non-linear crystal is pumped with vortices of orders 1, 2, 3 and their equal but oppositely charged coaxial superpositions.

where k_{x0} and k_a are radii of SPDC ring and aperture in momentum space, respectively. k_a is calculated from the Fourier relation $k_a = 2\pi x_a/\lambda f$, where x_a is the radius of aperture in real space, λ is the wavelength of down converted light and f is the focal length of the lens used in Fourier transformation. The aperture only allows small solid angled wave vector distribution defined by its diameter. One can expect that it may allow only wave vectors for single photons propagating through the same path and will eliminate wave vectors going in other directions. Indirectly, the spatial coherence is increased and have only one spatial mode which is expected to be the same as a pump.

When the SPDC photons are restricted by an aperture, the resultant angular spectrum, which is actually signal photon distribution, is written as

$$T_s(\mathbf{k}_s^{\perp}) = \int d\mathbf{k}_i^{\perp} |\Phi(\mathbf{k}_s^{\perp}, \mathbf{k}_i^{\perp}) A(\mathbf{k}_s^{\perp})|^2 \tag{3.22}$$

where $A(\mathbf{k}_s^{\perp})$ is the aperture function in spatial frequency coordinates. By controlling the diameter of the circular aperture, the SPDC amplitude distribution becomes identical to that of the pump as shown in Fig. 3.21(e). Amplitude transfer verified for different pump modes is shown in Fig. 3.22.

3.3.2 Experiment and Results

To verify the amplitude transfer experimentally, Type-I phase-matched BBO crystal of thickness 5 mm and transverse dimensions of 6 mm$\times$6 mm with an optic axis oriented at 29.97° is used. A pump beam of wavelength (405 ± 2) nm from a continuous-wave diode laser (TOPTICA iBeam Smart) of power density 4.4 W/cm^2 and a beam diameter 1.2 mm, incident on BBO crystal normally. Here, optical vortices of order 1, 2 & 3 and their equal but opposite coaxial superposition are used as different pump spatial modes. To generate the vortex superposition, a modified polarizing Sagnac interferometer [72, 73] is set up before the crystal, as shown in Fig.3.23. The first half-wave plate (HWP_1) is used to equalize the intensity of the counter-propagating beams inside the interferometer. A spiral phase plate (*SPP*) of desired order is introduced in the interferometer such that the counter-propagating beams acquire equal and opposite spiral phases before recombining at the polarizing beam splitter (*PBS*). In fact, the beam coming out of the interferometer is a vector vortex beam

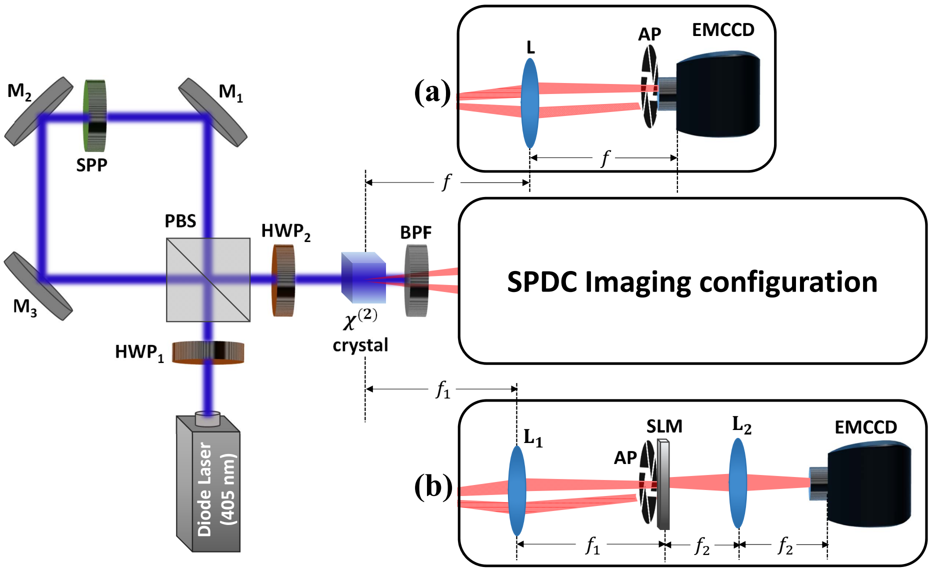

Fig. 3.23 Experimental setup for imaging parametric down converted photons restricted by an iris aperture. (a) Fourier imaging configuration. (b) 'Phase-flattening' configuration. Here, the focal length of lenses L_1 and L_2 are 500mm and 300mm respectively. HWP_1, HWP_2 - Half-wave plate, PBS - Polarizing beam splitter, SPP - Spiral phase plate, M_1, M_2, M_3 - Mirrors, BPF - Band pass filter, AP - Iris aperture, L, L_1, L_2 - Plano-convex lenses, SLM - Spatial Light Modulator, EMCCD - Electron Multiplying CCD Camera.

[74, 75]. Based on the orientation of the second half-wave plate (HWP_2) kept before the crystal, it will down convert only those modes whose polarization direction is along the optic axis of the crystal. The down converted photons (signal & idler) of wavelength 810 nm each (degenerate) are generated in a non-collinear fashion at diametrically opposite points of the SPDC ring. A bandpass filter (BPF) of central wavelength 810 ± 5 nm is used to filter down converted photons and block the pump beam after the crystal. The setup for collecting SPDC photons through an iris aperture is shown in Fig.3.23(a).

To show the effect of aperture on the spatial distribution of SPDC, the configuration shown in Fig.3.23(a) is arranged. As the AS ring generated from BBO crystal is very thin, one needs to use very small aperture, which is inconvenient. So AS ring has been allowed to propagate for a distance of 5 cm from the crystal before putting the aperture (ID15, THORLABS). To obtain the angular spectrum of SPDC, Fourier Transform property of the lens is used. A plano-convex lens (L) of focal length 10 cm is kept at a distance of 10 cm from aperture in the path of SPDC and the image is taken at a distance of 10 cm from the lens. For imaging the SPDC photons, an electron multiplying CCD

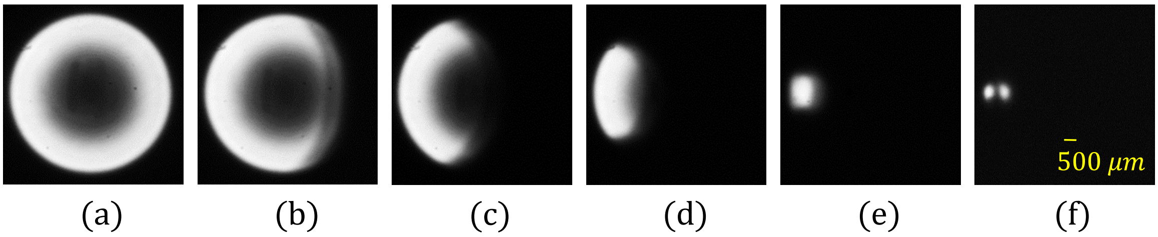

Fig. 3.24 Experimental angular spectrum of parametric down converted photons at the focal plane of the lens with gradual closure of the aperture to minimum ((a)-(f)). The pump used here is a superposition of equal and opposite first-order optical vortices.

(EMCCD) camera (Andor iXon3) of 512×512 pixels with a pixel size of 16×16 μm^2 is placed at the back focal plane. On selecting a portion of the ring, an intensity distribution identical to that of the pump is observed in the angular spectrum for small aperture size (Figure 3.24(f)). Here, the pump beam is a first-order Hermite-Gaussian (HG) mode formed by the superposition of optical vortices of orders +1 & −1 [76].

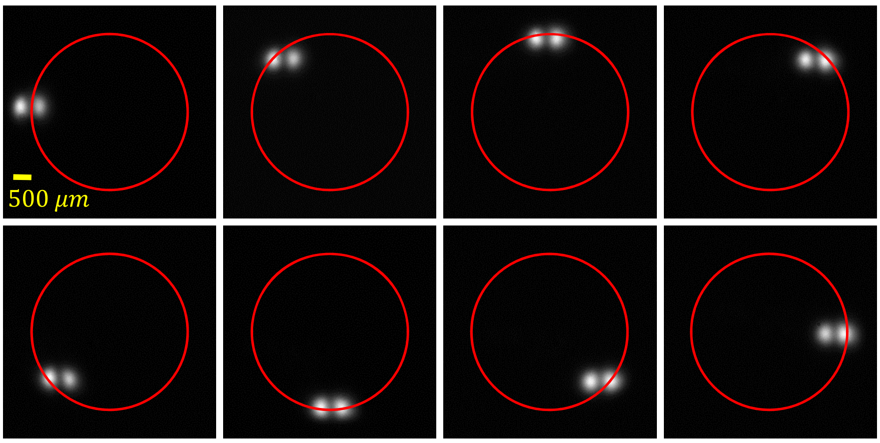

Fig. 3.25 Experimental angular spectrum of parametric down converted photons at the focal plane of the lens with aperture placed at eight different portions on the SPDC annular ring. A red circle is drawn on each sub-figure to show the position of the image corresponding to the portion selected on the SPDC ring.

Figure 3.24 (a-f) shows the images of the SPDC ring with gradual closure of the iris. Each image is recorded with the addition of 100 frames for an exposure time of 500 μs each. In the process, EMCCD was working in electron multiplying mode with a gain of x50. The same intensity pattern is observed irrespective of the portion selected from the SPDC ring. Figure 3.25 shows first order HG mode formed at eight different parts of the SPDC ring annular distribution. With the adjustment of the

HWP_2 and the use of different spiral phase plates in the interferometer, the SPDC image is observed for different pump modes. Figure 3.26 shows the experimental images of SPDC beam with minimal closure of iris for different pump polarization modes selected using HWP_2.

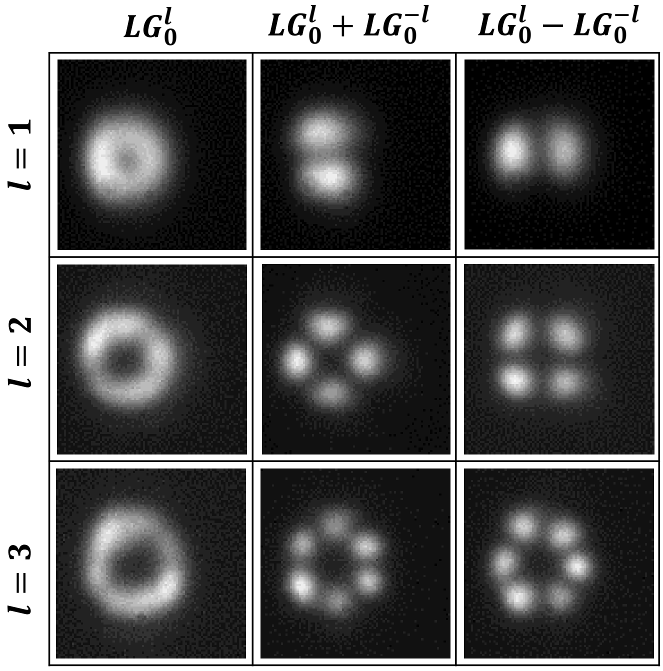

Fig. 3.26 Magnified images of experimental angular spectrum of parametric down converted photons when the non-linear crystal is pumped with vortices of orders 1, 2, 3 and their equal but oppositely charged coaxial superposition (same configuration as in Fig. 3.24(f)).

As we fix the center of the aperture at the point of maximum photon flux in the SPDC ring, the photons selected by minimal closure of the aperture will have propagation direction along the mean **k**-vector, satisfying phase-matching condition. These photons which are almost coaxial in propagation will sum up to give the pump mode distribution in the angular spectrum. When the aperture size is increased, the photons from the center of the aperture (paraxial photons) and the photons near to the edges of the aperture (marginal photons) superpose incoherently in the far-field, which reduces the contrast of the pump mode distribution present in the SPDC. With these arguments, one can consider SPDC annular distribution as an incoherent superposition of all photons that satisfy phase-matching condition, while the coincident detection of paired photons is a coherent process giving amplitude as well as the phase of the pump.

It is well known that the SPDC biphoton mode has a similar phase profile that of the pump. Here the phase profile of the signal or idler photon modes is studied without the heralding. A 'phase-

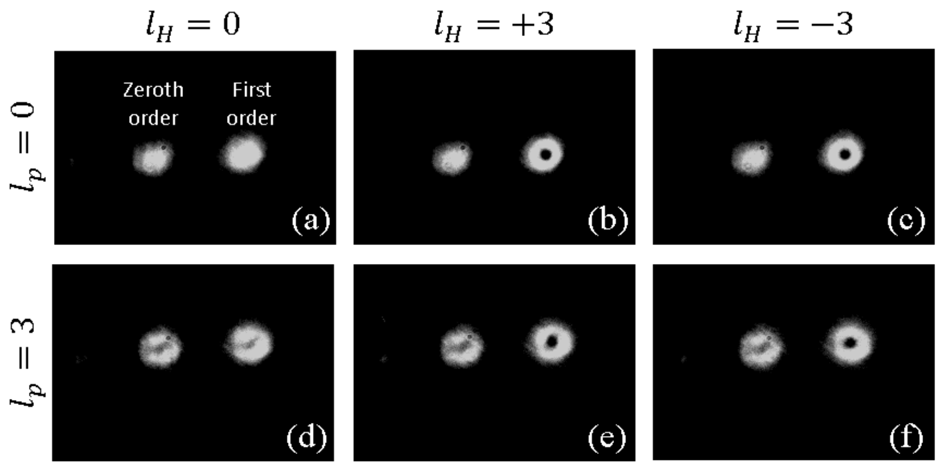

Fig. 3.27 Far-field zeroth and first order diffraction pattern of SPDC with a pump vortex beam of order l, and projected onto a forked hologram of order l_H.

flattening' method [59] is used to verify whether the observed mode distribution has an azimuthal phase when pumped with a vortex beam. The Fourier plane of the crystal is projected onto the holograms imprinted on a spatial light modulator (SLM - Hamamtsu LCOS) with an aperture kept closer to the SLM and the far-field diffraction pattern is imaged according to the configuration given in Fig.3.23(b). Figure 3.27(a)-(c) show the diffraction patterns of the SPDC pumped with Gaussian, and projected onto the forked holograms of order 0, $+3$ & -3 respectively. When a vortex of order 3 is pumped and the intensity distribution of the aperture plane is projected onto a $+3$ as well as -3 forked holograms, a Gaussian-like shape is not observed in the first-order diffraction pattern, which must be observed if the projected mode contains an azimuthal phase. This shows that the 'pump-mimicking' mode distribution of SPDC does not contain azimuthal phase corresponding to that of the pump. It is expected that the individual photons will not possess a particular azimuthal phase because they will be in a mixed OAM state while the two photons are entangled in OAM. However, the corresponding heralded single photons generated by SPDC process contain the azimuthal phase that has been well studied in the context of OAM entanglement [68, 31].

3.4 Conclusion

Starting with the angular spectrum of SPDC with Gaussian pump under focusing and collimating conditions, we have studied the angular spectrum of parametric down converted photons while pumping with normal optical vortex, Bessel-Gaussian and perfect optical vortex beams of different orders. For all three types of beams carrying OAM, the SPDC has a double ring distribution. For a normal vortex pump, the distance between the two peaks increases with the OAM, due to the increase in size of the vortex with order. However, for a Bessel-Gaussian or a perfect optical vortex beam, the size of vortex is independent of the order, and the angular spectrum of SPDC remains same for higher OAM values. The presented results are used for the efficient generation of heralded single photons carrying higher OAM values, as provided in Chapter 4.

We numerically and experimentally verified that all parametric down converted photons follow the transverse amplitude profile as that of the pump. Individual SPDC photons reveal the pump mode, when selected by a closed aperture and observed in the far-field. Increasing the spatial extent of the selected SPDC distribution by the aperture reduces the quality of the mode distribution observed, due to non-coaxial, incoherent superposition of paraxial and marginal photons from the aperture. Further, we show that the individual photons do not reveal anything about the transverse phase profile of the pump. The results will be useful in the engineering of SPDC entangled sources for applications in multi-dimensional quantum information schemes.

Chapter 4

Fiber Coupling of Biphoton Modes in SPDC

The photon pairs produced in SPDC are mainly used in the generation of single photons with the heralding of partner photon in the SPDC pair. Once the photon pairs are identified, it is important to couple the joint biphoton modes into fiber for the detection and measurement of correlation between photons in the pair. The spatial and temporal characteristics of heralded single photons [77] are utilized in fields such as quantum imaging [78] and testing fundamentals of quantum mechanics [79]. However, the individual signal or idler photons are incoherent in the absence of heralding.The propagation of biphoton state of SPDC with Fourier transforming elements has been studied earlier [80]. The two-photon correlation studies in SPDC have been carried out for various structured light pump beams [81–83]. In such cases, the two photon spatial modes obey the selection rules, giving rise to modal entanglement [39, 82, 84]. This can be measured by projecting the biphoton state to different modes using phase flattening techniques[59].

There have been many theoretical studies on effective fiber coupling of SPDC sources [85–89]. The main parameters that control the collection efficiency of photon pairs are thickness of the crystal used for down conversion, spatial walk-off, and mode field diameter of the optical fibers effectively imaged onto the crystal plane [85]. Coupling of SPDC photons with single-mode and multi-mode fibers were investigated [86] as a function of pump beam diameter, crystal thickness and walk-off. They observed entirely different behaviour between the coupling of SPDC photon pairs to the single-mode and multi-mode fibers by varying the pump beam diameter [87]. It was analytically shown that the coincidence spectrum becomes inseparable under strong pump focusing conditions so that the coincidence efficiency can be optimized [88]. It has been claimed that the important parameters for mode coupling in collinear parametric down conversion are the photon wavelength, the focal length of lens and the fiber diameter [89]. Use of single mode fiber attached detectors over direct spatial filtering of SPDC photons using a small slit is more advantageous, as in the former case, fringes smaller than the mode field diameter can be observed [90]. The results of numerical simulation [46] of heralded single photon purity and source brightness for pulsed pump source shows that an unengineered, pump focused, and filtered source gives higher number of fiber coupled photon pairs per pulse for smaller fiber collection mode radii. Similar work has been carried out for quasi-phase matched crystals, but coupling was investigated by considering the down converted output as a classical beam [91]. A numerical study was carried out for choosing birefringent crystals with appropriate cut angles for efficient down converted output in type-I phase-matching [45]. Dependence of photon coupling ratio on focusing parameter of pump and collection modes, and the crystal length in the case of periodically-poled crystals has been studied [92] with an emphasis on grating defects. A method for optimizing the collection of entangled photon pairs in type-II SPDC by controlling angular divergence of the collection modes has been discussed [93]. The theoretical framework of [70] shows that the optimum focusing conditions for maximum efficiency of collinear PDC are precisely same as that of sum frequency generation and parametric amplification using Gaussian beams [94]. This was experimentally verified using a collinear phase matched PPKTP crystal with collimating pump, signal and idler [95]. On the contrary, in [96], it has been shown that there is no significant change in the coupling efficiency of conditional biphoton modes with the focusing parameter. Also, it was experimentally shown that focusing of the pump beam enhances the photon pair detection efficiency in non-collinear type-II birefringent phase-matched [97] and collinear type-I quasi phase-matched [98] crystals.

4.1 Biphoton Sources

A biphoton source consists of a pair of photons coming from same or different photon generating systems. The pair is usually correlated in various degrees of freedom and the correlations will be present even at longer distances. Correlations and/or entanglement present in biphoton systems are articulated such that knowing the state of one photon reveals the information about the other. Therefore, correlated/entangled biphoton sources are used to study fundamental quantum mechanics as well as for applications in quantum information and communication.

A photon pair is entangled if its wavefunction cannot be written as a direct product of the wavefunctions of individual photons in the pair. As for the definition of entanglement, consider a system in Hilbert space represented by the state $|\psi\rangle$, consisting of two subsystems defined by orthonormal basis states $|\psi_1\rangle$ and $|\psi_2\rangle$. Now, let the state be written as

$$|\psi\rangle = \sum_{\psi_1,\psi_2} C(\psi_1,\psi_2)|\psi_1\rangle|\psi_2\rangle \tag{4.1}$$

where $C(\psi_1,\psi_2)$ is the probability amplitude of each $|\psi_1\rangle|\psi_2\rangle$ state. The state $|\psi\rangle$ is separable if $C(\psi_1,\psi_2)$ can be factorized to $C(\psi_1,\psi_2) = p(\psi_1)\times q(\psi_2)$. If $C(\psi_1,\psi_2) \neq p(\psi_1)\times q(\psi_2)$, then $|\psi\rangle$ is entangled.

All entangled photons are correlated. However, correlated photons may or may not be entangled. To understand the difference between correlation and entanglement, consider an example of two photons labelled A and B generated simultaneously at time t_1. The joint state of the photon pair generated is

$$|\psi\rangle \propto |\psi_A\rangle_{t_1}|\psi_B\rangle_{t_1} \tag{4.2}$$

The state given above is separable and correlated, *i.e.* measuring photon A will give the information about the time when photon B is created. Along with time t_1, if we consider another time t_2 when the two photons are generated again, we can write the state

$$|\psi\rangle \propto (|\psi_A\rangle_{t_1}|\psi_B\rangle_{t_1} + |\psi_A\rangle_{t_2}|\psi_B\rangle_{t_2}) \tag{4.3}$$

which is an entangled state in time. This state is also correlated in time.

4.2 Fiber coupling of SPDC biphotons

For setting up the experiment to generate and measure the correlated photon pairs, the following basic materials are required:

- Pump laser
- $\chi^{(2)}$ non-linear crystal to generate SPDC
- Single photon detectors: Single photon counting module (SPCM)
- Coincidence counter

A basic setup to generate and measure SPDC biphotons is given in Fig. 4.1(a). A laser of

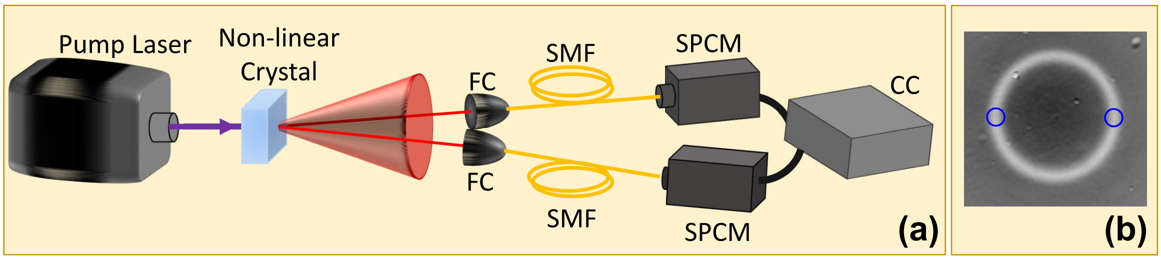

Fig. 4.1 Experimental setup to generate and measure correlated photon pairs in spontaneous parametric down conversion.

wavelength λ_p is used to pump a $\chi^{(2)}$ crystal which then gives SPDC photons as output in an annular distribution (Fig. 4.1(b), each having wavelength $2\lambda_p$ (degenerate case). Based on the phase-matching, the signal and idler photons are situated at the diametrically opposite points of the annular distribution. For convenience, we select those diametrically opposite points that are on the plane containing wave-vectors of pump, signal and idler, and that is parallel to the optic table (portions circled in blue on the SPDC ring, in Fig. 4.1(b)). The selected portions each can be either directly exposed to the CCD chip area on the single photon counting module (SPCM) using short focal lenses, or coupled to single-mode fibers that are attached to the SPCMs. To count the number of photon pairs, a coincidence counter is connected to both the SPCMs.

4.3 SPDC with focused pump beam

First, we study the effect of pump focusing on biphoton coupling efficiency of photon pairs obtained in a non-collinear SPDC process. We have experimentally verified that the coupling efficiency decreases asymptotically with the focusing parameter of the pump beam. We give theoretical explanation on how crystal thickness influences the behaviour of biphoton modes in pump focusing. We also give a physical reason for the decrease in coupling efficiency based on our experimental observation using the matching of conditional optical modes of down converted photons. We show that a loosely focused pump beam and a thin crystal are the best pre-detection conditions for the effective fiber coupling of entangled photons, as the former reduces the effect of SPDC ring asymmetry and the later reduces the walk-off effects inside the crystal. We also verify that the role of collection mode diameter on mode coupling to the fibers is more significant in tight pump focusing than in loose pump focusing.

4.3.1 Theory

Better sources of single photons by parametric down conversion require the efficient coupling of optical modes involved in the process, into the fiber. Before coupling, the down converted photons are spatially and spectrally filtered. The functions that represent the spatial and frequency (ω_c) filtering of down converted photons are given by

$$\Gamma_{spatial} = exp\left(-\frac{w_c^2}{2}|\mathbf{k}_c^2|\right), \tag{4.4}$$

$$\Gamma_{frequency} = exp\left(-\frac{(\omega_c - \omega_{c0})^2}{2B_c^2}\right) \tag{4.5}$$

where w_c and $\mathbf{k}_c$ are respectively the spatial collection mode width and the transverse momentum coordinate of collection mode. ω_{c0} and B_c are the central angular frequency and the bandwidth of the frequency filter respectively. In biphoton mode coupling, first we define a reference mode by imaging the single mode fiber-coupled idler photons onto the crystal. i.e., we project them into a single mode Gaussian

$$u(k_i^{\perp}) = exp\left(-\frac{w_i^2}{4}|\mathbf{k}_i^{\perp}|^2\right) \tag{4.6}$$

where $\mathbf{k}_i^{\perp}$ and w_i are respectively the transverse wave-vector and diameter of the idler mode. The conditional angular distribution of the down converted light in the signal arm has to be matched with this reference mode. Thus, the spatial distribution of heralded signal photon is given by the normalized mode function

$$\phi_s(\mathbf{k}_s^{\perp}, \Delta k) = N_s \int d\mathbf{k}_i^{\perp} \Phi(\mathbf{k}_s^{\perp}, \mathbf{k}_i^{\perp}, \Delta k) u(\mathbf{k}_i^{\perp}) \tag{4.7}$$

where N_s is the normalization factor. The conditioned spatial distribution of the idler photon, $\phi_i(\mathbf{k}_i^{\perp}, \Delta k)$, can also be obtained using similar calculations. A detailed comparative theoretical and numerical analysis of conditional angular distribution of the SPDC photons is given in [45]. In this, the effect of pump and crystal geometry on conditional angular spectrum has been studied separately along x and y directions.

Now, we study the effect of pump focusing on mode coupling efficiency. A focused Gaussian pump beam is characterized by a focusing parameter ξ_p [17], given by

$$\xi_p = \frac{L}{k_p w_p^2} \tag{4.8}$$

where k_p is the magnitude of wave vector for the pump beam, L is the crystal thickness and w_p is the pump beam waist located inside the crystal. Pumping a focused beam inside the crystal causes asymmetry in the spatial distribution of SPDC photons. Although the asymmetric broadening of SPDC ring looks identical in both positive and negative uni-axial crystals, the reason for broadening is different in both cases [99]. The pump walk-off is the main reason for asymmetry in negative uni-axial crystals where as SPDC photon's walk-off causes ring asymmetry in positive uni-axial crystals.

Perfect phase-matching is achieved for a plane-wave pumped normal to the crystal. As the pump is focused, there are contributions of pump wave-vectors non-normal to the optic axis of the crystal due to which phase mismatch effects appear. To reveal the nature of broadening along different directions along the crystal plane, we can use a cylindrical lens to focus the pump separately in the walk-off plane (the plane containing the pump wave-vector and the Poynting vector) and perpendicular to it [100]. Focusing the pump beam perpendicular to the walk-off plane broadens one part of the ring strongly, but hardly affects the corresponding diametrically opposite part while focusing the pump along the walk-off plane gives a uniform broadening. An analytical expression for calculating the broadening along both the directions is given in [101]. According to this, on performing angular scanning of the spatial distribution of SPDC photons along y-direction, there will be a simple y-shift of SPDC ring whereas scanning along x-direction shows x-shift as well as change in ring radii.

Coupling of biphoton modes into optical fibers is quantified using the quantity called biphoton mode coupling efficiency. A general expression for biphoton mode coupling efficiency is given by

$$\chi_{si} = \frac{C_{si}}{\sqrt{C_s C_i}} \tag{4.9}$$

where C_{si} is the measure of overlap of all the three modes - the correlated biphoton mode with the signal mode and the idler mode. C_s & C_i are the measures of overlap between the correlated biphoton mode and a single mode. In experiment, C_{si} turns out to be the coincidence counts and C_s, C_i are the singles count of signal and idler respectively. In terms of focusing parameters of pump and the diameter of the collection (signal & idler) modes, the coupling efficiency for a degenerate parametric down conversion under thin crystal approximation can be rewritten as [86]

$$\chi_{si} = \frac{4L(k_p \xi_p w_0^2 + L)}{(k_p \xi_p w_0^2 + 2L)^2} \tag{4.10}$$

where k_p is the magnitude of wave vector of the pump mode and w_0 is the diameter of each target modes.

The numerical plot of mode coupling efficiency vs pump focusing for different collection mode diameters (w_0) is given in Fig. 4.2. For a fixed value of focusing parameter, the coupling efficiency is more for smaller collection mode diameter. This behaviour is more pronounced in the loose focusing region ($\xi_p < 0.1$).

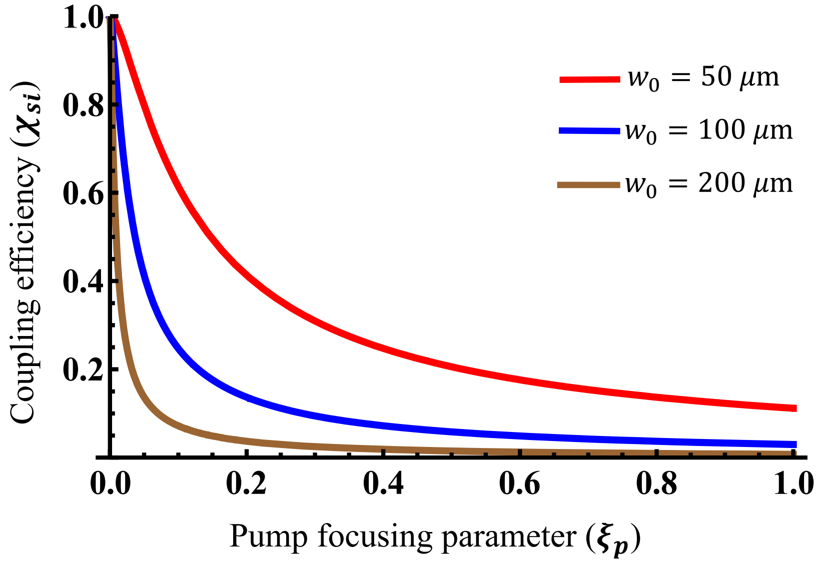

Fig. 4.2 Numerical plot of mode coupling efficiency versus pump focusing parameter with different collection mode diameters.

A crude estimation of the effective crystal length (L_{eff}) along which down conversion takes place is given in [46]. This effective crystal length depends on the pump focusing parameter, the orientation of propagation vectors of the down converted photons with respect to the pump beam, and the collection mode diameter (w_0). This is used to distinguish the behaviour of biphoton mode in different crystal length regimes [48]. In short crystal regime ($L < L_{eff}$), the biphoton mode is completely determined by the pump properties, i.e. the crystal length effects can be neglected. In the long crystal regime ($L > L_{eff}$), the biphoton mode depends on the pump as well as the crystal properties.

4.3.2 Experiment

The experimental setup used to verify the above theoretical arguments is given in Fig. 4.3. Here, we have used a UV diode laser (Toptica iBeam smart) of wavelength 405 nm and power 300 mW with a spectral band width of 2 nm, to pump the non-linear crystal, Type-I β-Barium Borate (BBO), of thickness 2 mm and transverse dimensions of 6 mm×6 mm with an optic axis oriented at 29.97° to the normal incidence. The combination of a polarizer and a half wave plate allows us to vary the pump beam polarization along the crystal axis. A plano-convex lens is used to focus the pump beam inside the crystal kept at the focal plane. For changing the focusing parameters, plano-convex lenses of focal lengths 50, 100, 150, 200, 250, 300 & 750 mm are used in our experiment. The down converted photons (signal & idler) of wavelength 810 nm each (degenerate) are generated in a non-collinear fashion at diametrically opposite points of the SPDC ring. The images of the down converted ring for different focusing conditions were taken using an Electron Multiplying CCD (EMCCD) camera (Andor iXon3) of 512×512 pixels with a pixel size of 16×16 μm^2.

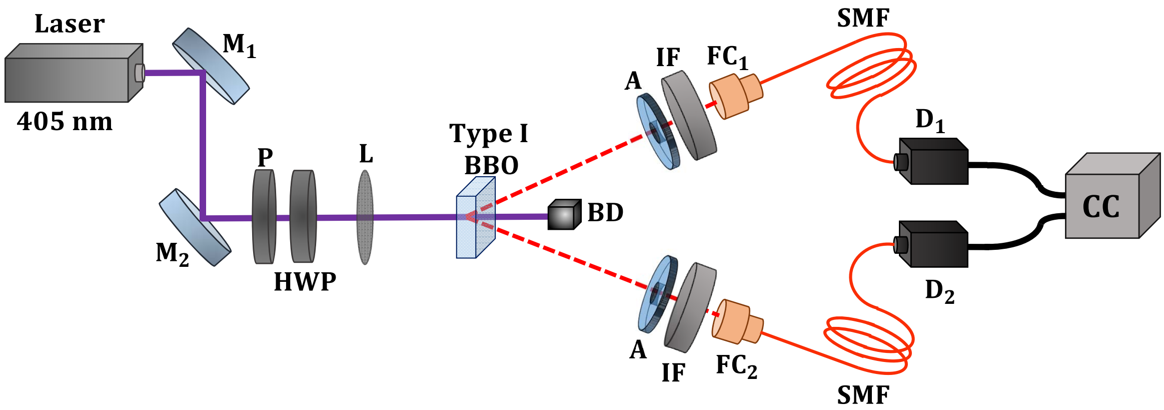

Fig. 4.3 Experimental setup used for generating the correlated photon pairs through SPDC process. Here, M_1,M_2 - Plane mirrors; P - Polarizer; HWP - Half Wave Plate; L - Plano convex lens; A - Aperture; IF - Interference filter; BD - Beam dump; FC_1,FC_2 - Fiber collimators; SMF - Single Mode Fiber; D_1, D_2 - Single photon counting modules(SPCM's); CC - Coincidence Counter.

To measure the number of photon pairs generated, two diametrically opposite portions of the SPDC ring at a given plane were selected using apertures (A) and the photons coming out of each aperture were collected using the fiber collimators FC_1 & FC_2 (CFC-5X-B, Thorlabs) of focal lengths 4.6 mm and a numerical aperture of 0.53. The fiber collimators are attached to the single mode fibers (P1-780A-FC-2, Thorlabs) each having a numerical aperture of 0.13 and a mode field diameter of 5±0.5 μm, which in turn are connected to the single photon detectors D_1 & D_2 (SPCM-AQRH-16-FC, Excelitas). The detectors have a timing resolution of 350 ps with 25 dark counts per second. Two interference filters (IF) of passband 810±5 nm are kept very close to the fiber collimators to make sure that other unwanted wavelengths are properly filtered out. To measure the number of correlated photon pairs, the two detectors are connected to a coincidence counter (CC), IDQuantique-ID800, having a time resolution of 81 ps.

4.3.3 Results

To study the effect of pump focusing on biphoton modes, first we study the effect of asymmetry present in the angular distribution of down converted photons obtained for different focusing parameters. For this, we image the ring of down converted photons using an Electron Multiplying CCD camera. These

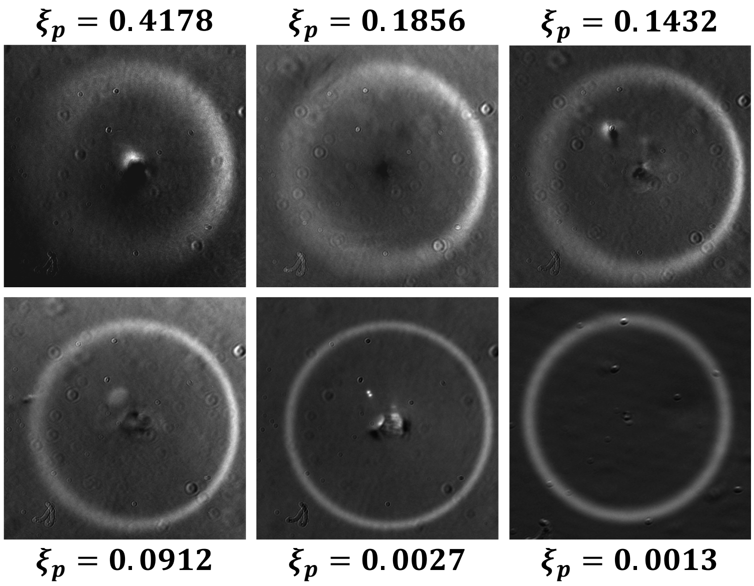

Fig. 4.4 Electron Multiplying CCD images of the down converted rings for different pump focusing parameters obtained using different lenses of focal lengths f=100, 150, 200, 300, 600 & 750 mm.

images are shown in Fig. 4.4 corresponding to the different pump focusing parameters obtained by focusing the pump beam on to the crystal using different plano-convex lenses of focal lengths 100, 150, 200, 300, 600 & 750 mm. The inhomogeneity in the spatial distribution of the down converted photons increases with the pump focusing parameter, i.e. with the decrease in the focal length of the lens used to focus the pump beam. The experimental results agree with the numerical simulation given in [99].

In order to quantify the asymmetry of a ring formed by the down converted photons, we introduce an asymmetry factor (AF), which is defined as [102]

$$AF = 1 - \frac{b}{a} \tag{4.11}$$

where a and b are the ring widths at two diametrically opposite ends of the down converted ring ($a > b$) as shown in inset of the Fig. 4.5. The asymmetry factor is calculated for different focusing

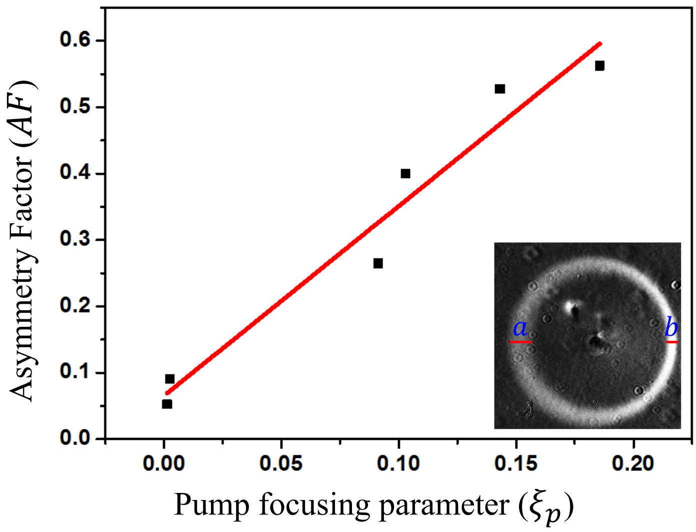

Fig. 4.5 Variation of SPDC ring asymmetry with pump beam focusing.

parameters of the pump beam and shown in Fig. 4.5. We found that the asymmetry increases with the increase in focusing parameter i.e. when we move from loose focusing to tight focusing of the pump beam. Also, we observed that the asymmetry is independent of the propagation of down converted photons from the crystal plane. The variation of asymmetry factor is linear with respect to the focusing parameter. To study the influence of the crystal chosen (L=2 mm), we calculated the effective crystal length (L_{eff}) [46] for each value of the pump focusing parameter used in the experiment. Under tight focusing condition ($\xi_p > 0.1$), L_{eff} is $\sim$12.3 mm and for loose focusing condition ($\xi_p < 0.1$), it is $\sim$13.9 mm. So, the range of pump focusing parameters we considered in the experiment were found to satisfy the condition $L < L_{eff}$ [48], i.e. the influence of crystal length on the asymmetry in the SPDC ring is negligible when compared with that of the pump focusing parameter.

For coincidence detection, we choose two diametrically opposite portions of the down converted ring using two apertures of same width as shown in Fig. 4.6. Because of the asymmetry of SPDC

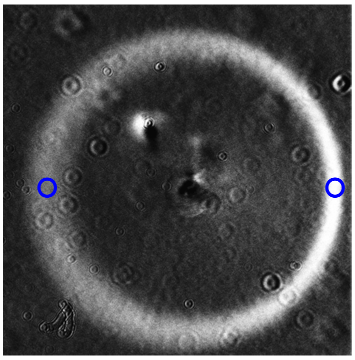

Fig. 4.6 EMCCD image of a ring of down converted photons. For coincidence counting setup, the two diametrically opposite points of the ring (shown in blue circles) are selected.

ring, the photon number densities (number of photons per unit area) of signal and idler in the selected areas are different due to which we are not able to select all the signal photons that correspond to the selected idler photons. This accounts for the asymptotic decrease in mode coupling efficiency of down converted photon pairs with pump focusing.

Now, in order to see how the difference in photon number densities of signal and idler affect the conditional coincidence images of down converted photons, we recorded the conditional spatial distribution of signal photons under two extreme pump focusing conditions, i.e. loose pump focusing (Fig. 4.7(a), (b)) and tight pump focusing (Fig. 4.7(c), (d)). To image conditional biphoton modes, the fiber collimators (FC_1 & FC_2) kept in signal and idler arms were mounted on XY translational stages. The fiber collimator in the idler arm was adjusted to get maximum individual counts. Then the fiber collimator in the signal arm was moved manually along X & Y directions with a step size of 1 mm. A total of 400 and 900 spatial points were considered for scanning in loose pump focusing and tight pump focusing cases respectively. The individual as well as the coincidence counts were recorded for each array point. Figures 4.7 (a), (b) and 4.7 (c), (d) show the numerical and the corresponding experimental results for the conditional coincidence imaging under both the conditions. The numerical results are obtained by plotting the density plots of normalized conditional signal mode function described by the Eqn. (4.7), for loose and tight pump focusing conditions respectively. It is clear from

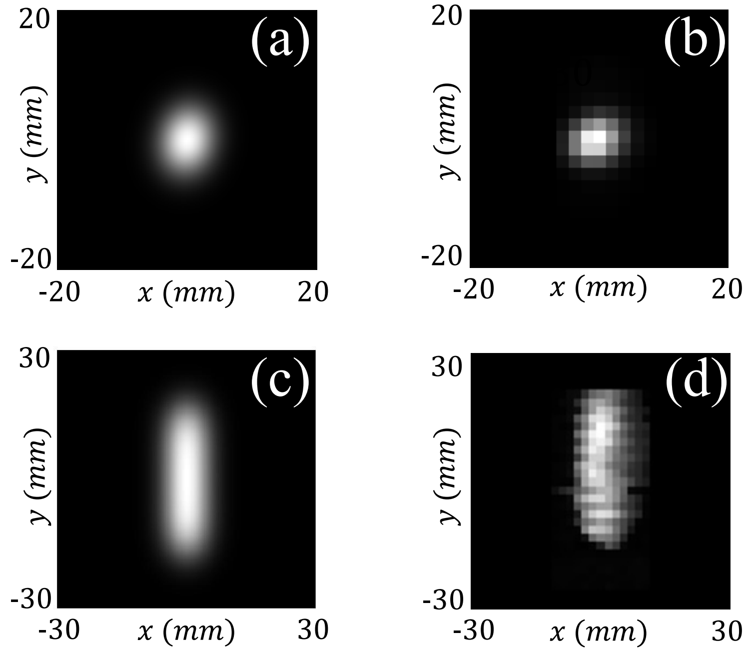

Fig. 4.7 (a) Numerical and (b) experimental plots of the conditional spatial distribution of signal photons under loose focusing condition of the pump beam, here $\xi_p \sim 0$ i.e. without using any lens. (c) Numerical and (d) experimental plots of the conditional spatial distribution of signal photons under tight focusing condition of the pump beam, here ξ_p=0.832 obtained using a lens of focal length f=50 mm.

the figure that the experimental results are in good agreement with the numerical simulations. We also observe that the overlap extent of conditional signal and idler modes decreases under tight focusing condition as one of the conditional modes becomes elliptic for a given idler coupled in a single mode fiber.

For observing the effect of pump focusing on biphoton modes, we tried to quantify the degree of overlap between conditional signal and idler modes in down conversion and its variation with pump focusing parameter. For this, we calculated the biphoton mode coupling efficiency (χ_{si} given in Eqn. (4.9)) for different pump beam focusing parameters. Fig. 4.8 shows the variation of experimentally obtained biphoton mode coupling efficiency (χ_{si}) with the pump beam focusing parameter and the corresponding numerical results. We achieved the maximum coupling efficiency of only 8%, which is attributed to the mismatch of the numerical aperture of fiber collimator (FC) and single mode fiber used for the experiment. To calculate the focusing parameter of the pump beam, we calculated the

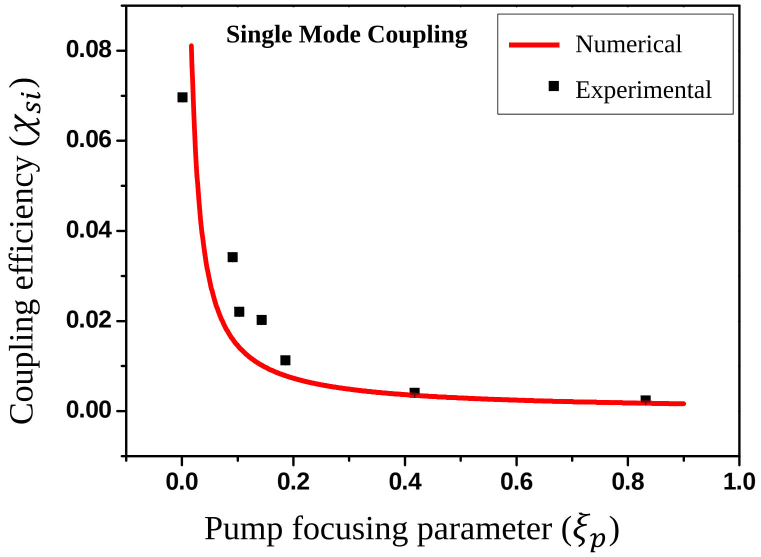

Fig. 4.8 Experimental plot of the variation of photon pair collection efficiency with respect to pump focusing parameter. Error bars have been subsumed by the thickness of the experimental points.

beam diameter at the focus. The diameters of two collection modes projected onto the crystal are calculated as w_0=456 μm. We observed an asymptotic decrease in coupling efficiency with the pump focusing parameter, which matches with the theory of intensity-based single mode fiber coupling of down converted photons given in [86]. From the numerical plot given in Fig. 4.2, it is clear that the influence of collection mode diameter is nominal under tight focusing condition ($\xi_p > 0.1$) where as it is significant for loose focusing condition ($\xi_p < 0.1$). From the graphs, one can also observe that the coupling efficiency is higher for loose focusing than tight focusing, which is also clear from our experimental results given in Fig. 4.8. In our experiment, we used the same crystal length and collection mode diameter in order to study the effect of focusing on the coupling efficiency. We observe that the coupling efficiency mainly depends on the overlap of two conditional modes and the asymmetry present in the ring of down converted photons. However, in the case of collinear phase-matching, the interaction length of pump and down converted photon modes are more, due to which the spatial walk-off does not necessarily restrict the collection efficiency of photon pairs even with thick crystals [103].

4.4 Generation of heralded twisted single photons in SPDC

In the previous sections, we have seen the method to optimize the heralding efficiency of single photons generated in SPDC. This section explains the method to generate heralded twisted single photons, *i.e.* the single photons carrying orbital angular momentum (OAM). The angular spectrum of pump gets transferred to the SPDC photon pairs [40]. Also, the azimuthal phase of the pump also gets transferred to the signal photon it the idler photon is projected to a simple Gaussian mode [41]. This comes from the conservation of OAM in an SPDC process [104].

4.4.1 Experiment

The experimental setup to generate heralded twisted single photons from SPDC is given in Fig. 4.9. Here, we have used a Blue diode laser (TOPEMODE) of wavelength 405 nm and power 20 mW with a spectral band width of 0.1 nm, to pump the non-linear crystal, Type-I β-Barium Borate (BBO), of thickness 5 mm and transverse dimensions of 6 mm$\times$6 mm with an optic axis oriented at 29.97° to the normal incidence. The combination of a polarizer and a half wave plate allows us to vary

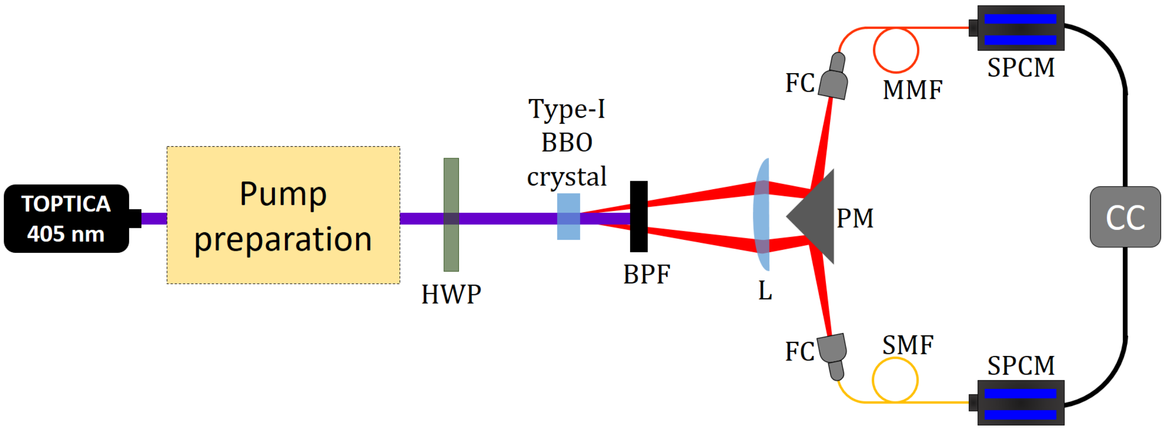

Fig. 4.9 Experimental setup to generate heralded twisted single photons from SPDC with different pump beams carrying OAM. Here, HWP - Half-wave plate; BPF - Band pass filter; L - Plano convex lens; PM - Prism mirror; FC - Fiber coupler; SMF - Single-mode fiber; MMF - Multimode fiber; SPCM - Single photon counting module

the pump beam polarization along the crystal axis. The dashed box in Fig. 4.9 corresponds to the case-by-case method to prepare pump beams of different spatial characteristics, which are given below. The down converted photons (signal & idler) of wavelength 810 nm each (degenerate) are generated in a non-collinear fashion at diametrically opposite points of the SPDC ring.

To measure the number of photon pairs generated, two diametrically opposite portions of the SPDC ring at a given plane were selected using apertures (not shown in the setup) and the photons coming out of each aperture were collected using the fiber collimators FC (CFC-2X-B, Thorlabs) of focal lengths 2 mm. The fiber collimator in idler arm is attached to a single mode fiber (P1-780A-FC-2, Thorlabs) having a numerical aperture of 0.13 and a mode field diameter of 5$\pm$0.5 μm, and that in the signal arm is attached to a multi-mode fiber (ML43L02, Thorlabs). The fibers are connected to the single photon detectors SPCMs (SPCM-AQRH-16-FC, Excelitas). The detectors have a timing resolution of 350 ps with 25 dark counts per second. To measure the number of correlated photon pairs, the two detectors are connected to a coincidence counter (CC), IDQuantique-ID800, having a time resolution of 81 ps.

4.4.2 Results

First we recorded the coincidences of signal and idler for normal optical vortex, Bessel-Gaussian, and perfect optical vortex pump for upto an OAM of 6. Figure 4.10 (a-c) show the coincidences for NOV, BG and POV pump beams with different orders. The coin As the size of the normal optical vortex increases with order, the singles counts in the signal arm (coupled to a multi-mode fiber) and idler arm (coupled to a single mode fiber) decreases and as a result, the coincidence counts also decreases. The variation of counts in the signal for different OAM values is slower than that in the idler arm. For a BG and POV pump beams, the variation in singles for signal and idler is less and due to this, the corresponding variation in the coincidence counts is also lesser than that with a normal vortex pump.

To compare the heralding of SPDC single photon for different pump modes, the normalized coincidence and the corresponding heralding efficiency (calculated using Eqn. 4.9) for different pumps is plotted in Fig. 4.10 (d) and 4.11 respectively. From the graph, we see that the variation of heralding efficiency is much lower for the heralded twisted single photons generated using BG and

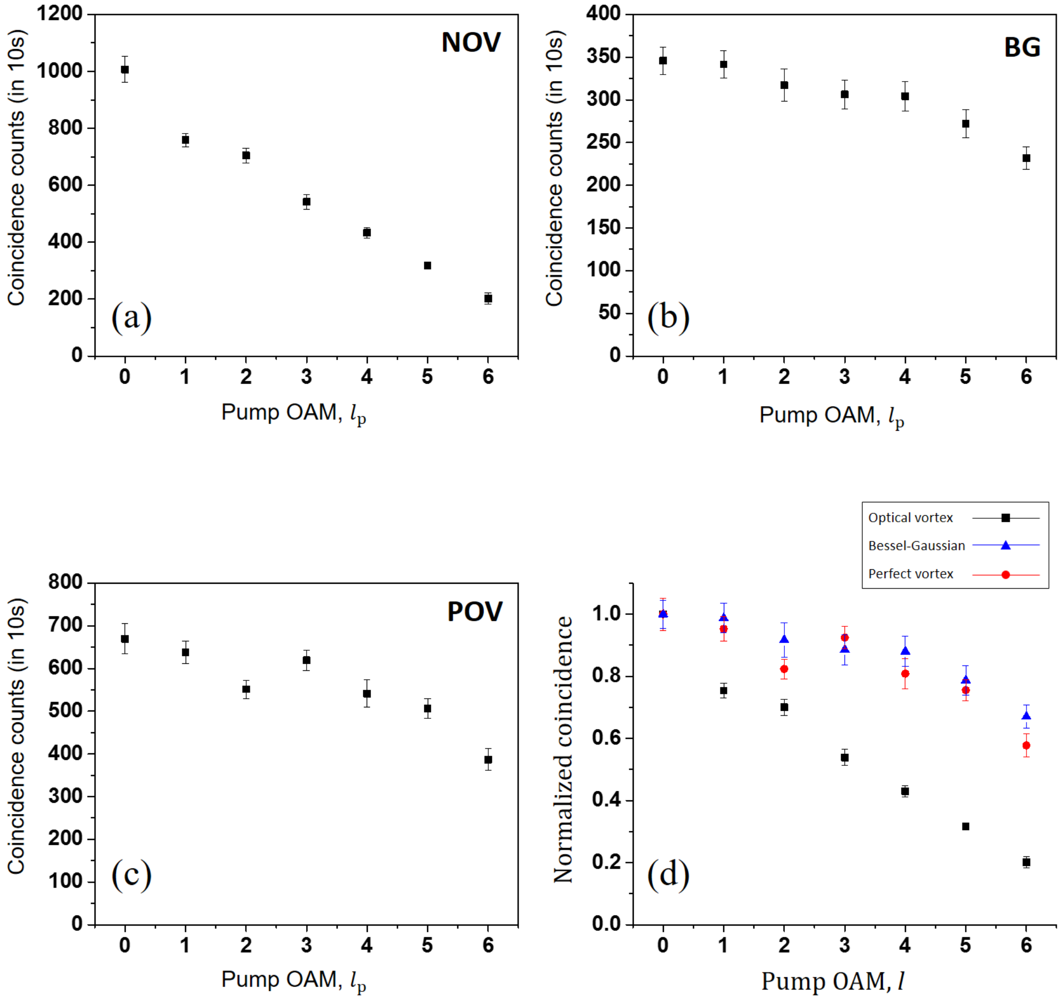

Fig. 4.10 Plots showing coincidence counts of SPDC photons pumped with (a) normal optical vortex (NOV) (b) Bessel-Gaussian (BG) and (c) perfect optical vortex (POV) pump beams of different orders. (d) Normalized coincidence of SPDC pairs with all pump modes.

POV pump beams than that of a normal optical vortex pump. So, the BG and POV pump can be used to generate efficient twisted single photons of higher OAM.

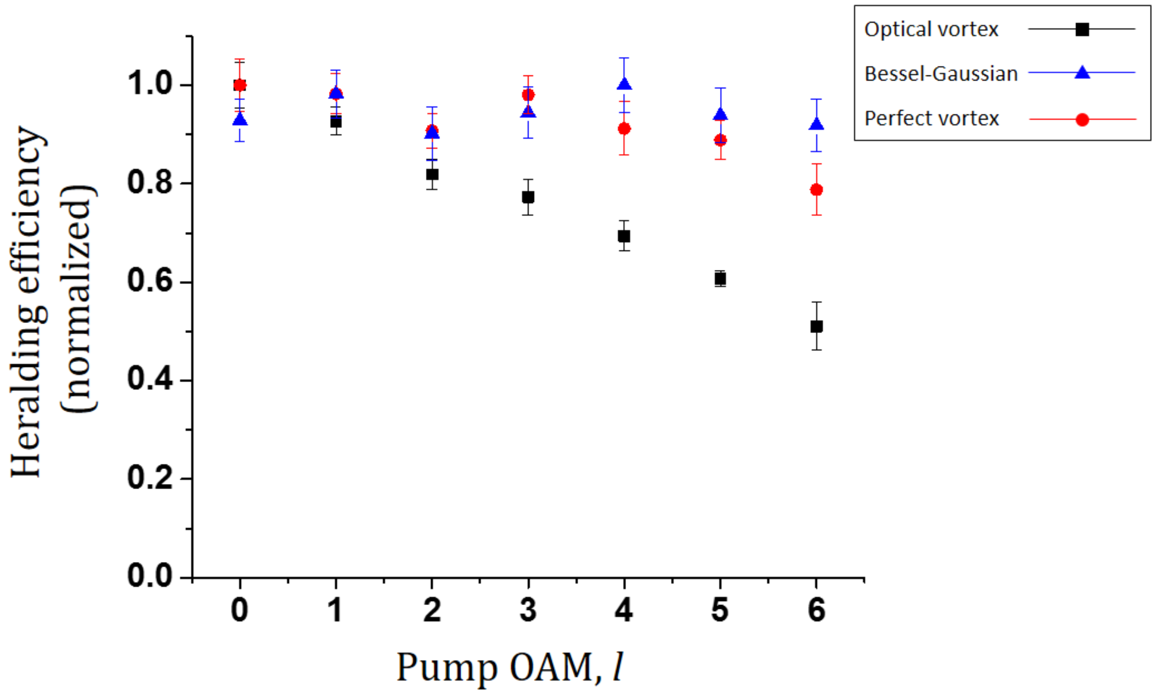

Fig. 4.11 Plot showing heralding efficiency of SPDC photons pumped with normal optical vortex, Bessel-Gaussian and perfect optical vortex pump beams of different orders.

4.5 Conclusion

We have studied the effect of pump beam focusing on photon pair coupling efficiency of signal and idler in Type I non-collinear spontaneous parametric down conversion. We have experimentally verified that the conditional coupling efficiency of the down converted biphoton modes into a single mode fiber varies asymptotically with the pump beam focusing parameter. This behaviour is attributed to the the asymmetry in the spatial distribution of down converted photons with the pump beam focusing parameter, due to which the conditional modes of down converted photons become elliptic. From our observations, we conclude that a loosely focused or almost collimated pump beam inside a thin crystal is the best pre-detection scenario for very good fiber coupled heralded single photon pairs. These mode coupling techniques will be very useful in generating better sources of heralded single photons for quantum information processing [105].

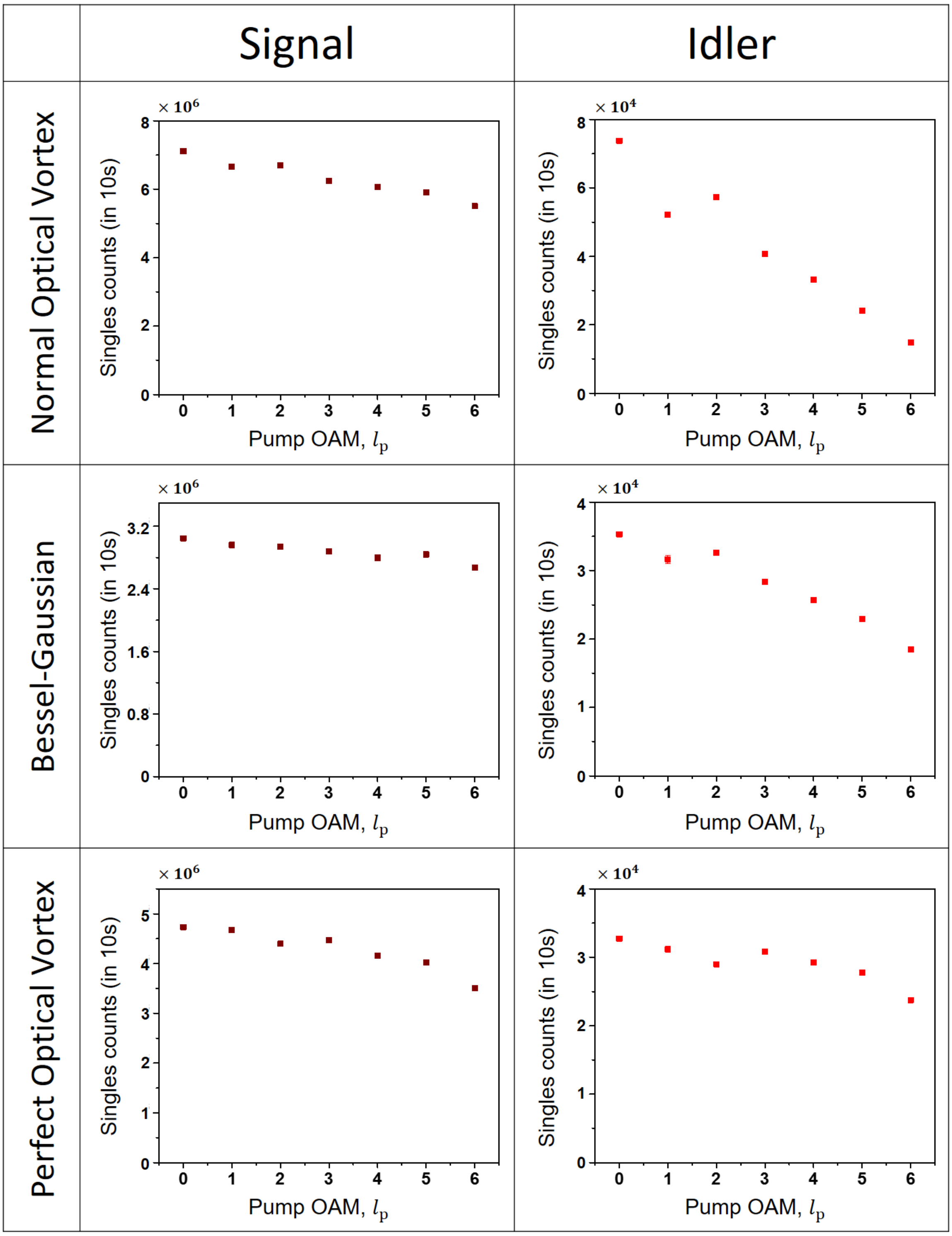

Fig. 4.12 Plots showing indivdual counts of SPDC photons pumped with normal optical vortex (NOV), Bessel-Gaussian (BG) and perfect optical vortex (POV) pump beams of different orders.

We also studied the effect of pumping different beams carrying orbital angular momentum (OAM) on the coupling efficiency of signal and idler in Type I non-collinear spontaneous parametric down conversion. Due to the increase in size of conventional optical vortex beams with order, the heralding efficiency of SPDC single twisted photons with normal optical vortex beams decreases with order of pump vortex. We have experimentally showed that the conditional coupling efficiency of the heralded twisted single photons for higher OAM values can be improved by using a Bessel-Guassian or perfect optical vortex beams as pump. The presented results may be utilized for the practical realization of efficient higher dimensional OAM entangled photons.

Chapter 5

Orbital Angular Momentum Correlations in SPDC

According to Maxwell's theory, an electromagnetic (EM) wave travels with speed of light and carries certain energy and momentum [106]. The momentum of light has both linear and angular part. Magnitude of the propagation vector of light gives its linear momentum. The angular part of light's momentum is again classified into spin and orbital parts. Spin angular momentum is associated with the polarization of light. Light has a spin of $\sigma = \pm 1$ if it is left/right circularly polarized, and has a zero spin if it is linearly polarized. Spin angular momenta was first introduced by Poynting [107] and experimentally realized by Beth [108]. The orbital angular momentum (OAM) of light is associated with its spatial modes [109]. For a light carrying OAM, the Poynting vector associated with the electromagnetic wave spirals around the propagation axis of the light beam.

After the successful realization of two dimensional entangled states with the polarization of down converted photons, the search for a system to set up entanglement in higher dimensions resulted in the generation of bipohoton OAM states in spontaneous parametric down conversion. Access to higher dimensions in Hilbert space makes OAM of light a suitable candidate for realizing new types of secure quantum information schemes [110]. Along with polarization, the down converted photons possess a definite OAM that comes from the OAM conservation, which is revealed when both the signal and idler are measured. The first experiment to illustrate the conservation of OAM in SPDC was carried out by Mair *et.al.* [31]. Higher dimensional entanglement for dimensions upto 12 was experimentally demonstrated by Dada *et.al.* [111]. Although, OAM modes corresponding to higher dimensions can be theoretically attained, effects of many experimental factors such as the mode sizes of interacting photons [112] as well as the length [113] and orientation [114, 115] of the non-linear crystal, make it difficult to achieve.

5.1 Orbital Angular Momentum of Light

Light beams having Laguerre-Gaussian (LG) intensity distribution with phase singularities possess an orbital angular momentum (OAM). During their propagation, the energy flows spirally about the beam axis. So, these beams are also called as optical vortices. An LG mode of radial and azimuthal indices p and l respectively, on a plane $z = 0$, is given by

$$LG_l^p(r,\phi) = \frac{C_{lp}}{w}\left(\frac{r\sqrt{2}}{w}\right)^{|l|} L_{|l|}^p\left(\frac{2r^2}{w^2}\right)\exp\left(-\frac{r^2}{w^2}\right)\exp\left(-ik\frac{r^2}{2R}\right)\exp(-il\phi) \tag{5.1}$$

where r and ϕ are the radial and azimuthal coordinates respectively, k is the magnitude of the wave

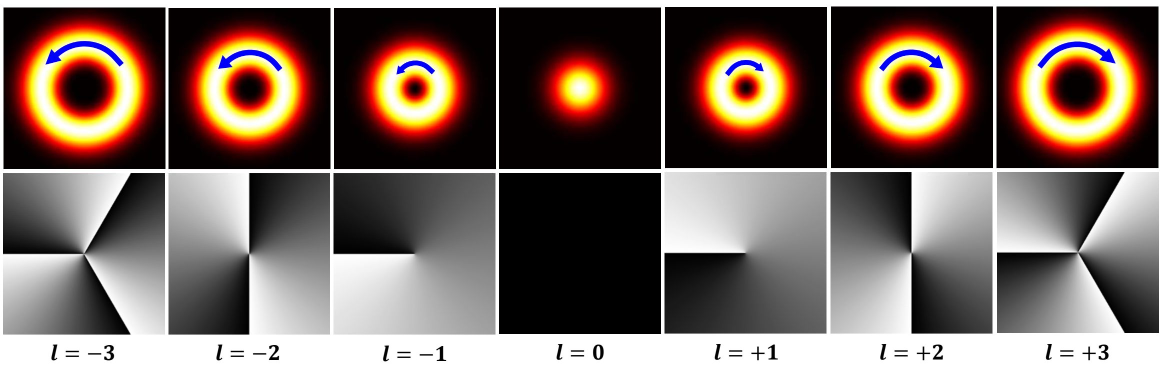

Fig. 5.1 Intensity distribution (upper row) and phase distribution (lower row) of optical vortices for topological charges $l = -3, -2, -1, 0, 1, 2$ & 3. The blue curved arrows show the direction of spiralling of energy flow of vortex around the beam axis.

vector, C_{lp} is the mode amplitude, w and R are the width of the beam and radius of curvature of the wavefront respectively. Fig. 5.1 shows the intensity and phase distribution of LG beams of different orders.

5.1.1 Generation of light carrying orbital angular momentum

Optical vortices can be generated by various methods. One of the methods is to use a spiral phase plate (SPP) (or 'vortex lens'). A spiral phase plate of topological charge l is a transparent optical element with spirally varying thickness with azimuthal angle [65]. Practically, it is difficult to make the gradual variation of thickness along azimuthal direction. So, the plate has a number of radial sectors with different thickness that increases as we move along the surface of the plate azimuthally. A Gaussian beam of wavelength λ, on passing through an SPP, introduces an azimuthally dependent phase shift given by

$$\delta = \frac{(n-1)t}{\lambda}\phi \tag{5.2}$$

where n is the refractive index of SPP material, t is the maximum thickness of the plate and ϕ is the azimuthal angle. The outgoing beam will have an OAM $l\hbar$ if the total phase delay around the SPP is an integral multiple of 2π, *i.e.* $2\pi l$, where l is an integer. So, by doing back calculation with Eqn. 5.2, we obtain the maximum thickness of the SPP as

$$t = \frac{l\lambda}{n-1} \tag{5.3}$$

Other methods to generate optical vortices are computer generated holograms (CGH) and spatial light modulators (SLM). Computer generated holograms are used for the generation as well as the analysis of OAM modes. CGHs are diffraction gratings printed on a transparent film based on a specific machine-calculated interference pattern formed by a reference plane wave and the desired beam that has to be generated. For example, if the reference beam is an optical vortex of charge l, its interference pattern with a plane wave to be imprinted on the hologram is made by a diffraction grating with l lines forming a multi-pronged fork. Fig. 5.2 shows the forked holograms for various orders. When a Gaussian beam is passed through the centre of the l^{th}-order grating, an optical vortex

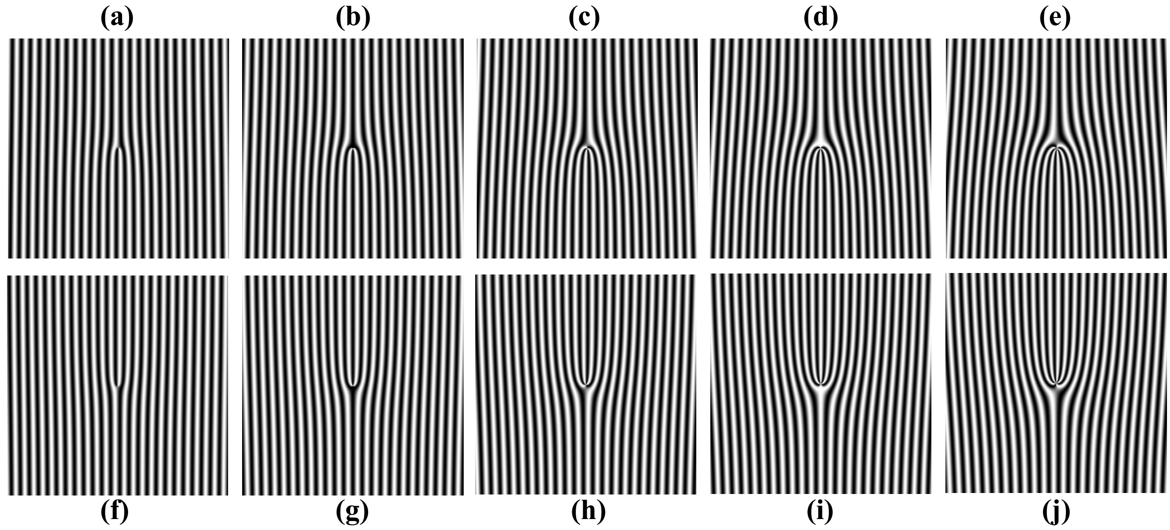

Fig. 5.2 (a)-(e) Computer generated holograms for topological charges $l = 1,2,3,4$ & 5. (f)-(j) Computer generated holograms for topological charges $l = -1,-2,-3,-4$ & -5.

of charge l is generated at the first diffraction order. In similar way, on can generate optical vortices with a Gaussian light beam incident on a forked grating displayed on an SLM.

5.1.2 Analysis of orbital angular momentum of light

The methods to detect and analyse the OAM content of a light beam are interferometry [116], tilted-lens technique [61], double-slit interference [117] and phase-flattening technique [59]. Out of these techniques, the later one works in classical as well as single-photon level. Here, we discuss about phase-flattening technique that is more effective in the analysis of OAM entangled states of light.

Spatial light modulators (SLM) are used to generate optical vortices of various topological charges. For a fundamental Gaussian beam having zero OAM incident on a forked diffraction grating of topological charge l imprinted on an SLM display, the first order diffracted light will have an annular intensity distribution with a helical phase represented by $\exp(il\phi)$. Looking in the reverse fashion, one can use these holograms to detect the OAM of incident mode. When a light beam of OAM l is diffracted by a forked hologram of topological charge $-l$, a fundamental Gaussian mode is generated at the far-field intensity distribution. This technique is known as 'Phase flattening'. In this technique, the helical phase of the incident beam is cancelled by the forked grating on the SLM.

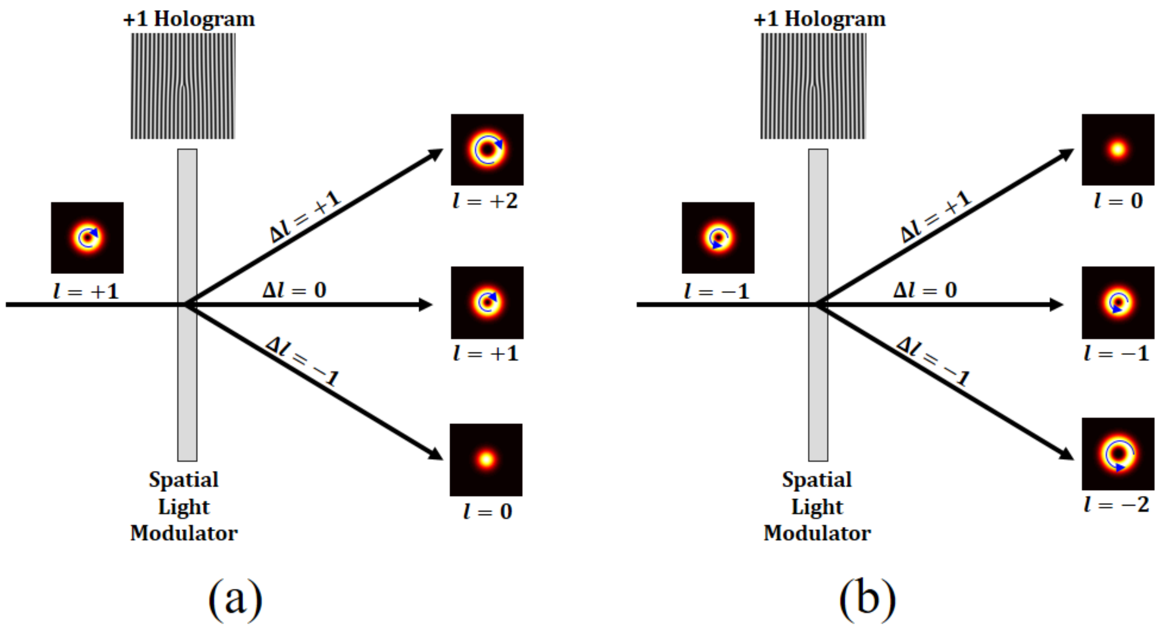

Fig. 5.3 Phase flattening method to detect optical vortex of topological charge (a) +1 and (b) -1.

Use of different holograms on SLM is advantageous in filtering out different OAM contents from an unknown superposition of OAM states. For example, to extract $+1$ OAM content from an unknown state, the light is incident on an SLM display of -1 hologram and the first order diffracted output is coupled to a single-mode fibre (SMF), which allows only $l = 0$ (fundamental Gaussian) to pass through (Fig. 5.3 (a) & (b)). At the photon level, a combination of SLM with forked diffraction gratings of various topological charges, a single mode fibre (SMF) along with a single-photon detector acts as a device for performing projective measurements of the OAM eigenstates of single photons.

5.2 Entanglement of orbital angular momentum states of light

Along with the conservation of energy and momentum in spontaneous parametric down conversion (SPDC) process, there is also conservation of orbital angular momentum (OAM), which states like this: 'OAM of the pump has to be the sum of OAM of signal and idler' in paraxial regime followed in our experiments. This OAM conservation leads to the observation of OAM correlations and entanglement in SPDC biphoton modes for any type of SPDC phase-matching. The signal and idler beams in SPDC have independently very low spatial coherence, and they are a mixture of many different OAM eigenstates. For a pump beam carrying an OAM of l_p, the OAM of signal (l_s) and idler (l_i) are distributed according to [104]:

$$l_p = l_s + l_i \tag{5.4}$$

Then a pure state of biphotons generated in SPDC will be

$$|\psi\rangle_{\text{SPDC}} = \sum_{l_s=-\infty}^{\infty} c_{l_s,l_p-l_s} |l_s\rangle_a |l_p - l_s\rangle_b \tag{5.5}$$

where the subscripts a and b represent signal and idler photons respectively. c_{l_s,l_p-l_s} is the probability amplitude to create a photon pair carrying OAM $l_s\hbar$ and $(l_p - l_s)\hbar$. For example, if we pump with a fundamental Gaussian beam ($l_p = 0$), the SPDC biphoton state is represented as

$$\begin{aligned} |\Psi\rangle &= c_{0,0}|0\rangle_a|0\rangle_b \\ &+ c_{1,-1}|1\rangle_a|-1\rangle_b + c_{-1,1}|-1\rangle_a|1\rangle_b \\ &+ c_{2,-2}|2\rangle_a|-2\rangle_b + c_{-2,2}|-2\rangle_a|2\rangle_b + \dots \end{aligned} \tag{5.6}$$

The state given in Eqn. 5.6 is a multi-dimensional OAM entangled state of two photons. This means that none of the photons in the SPDC output possess a well-defined orbital angular momentum. To measure the OAM of a photon in this state, one has to use the 'phase flattening' technique (as described in the previous section) in signal and idler arms so that the coincidence values measured corresponding to these projections give the number of photons having a particular OAM as well as the probability of twin photons to be in a state defined by a particular OAM basis.

To generate and measure OAM entanglement in SPDC biphotons experimentally, the scheme given in Fig. 5.4 is implemented. Pump beam from a laser is incident on a second order non-linear crystal to produce SPDC photon pairs. The signal and idler each is sent to a spatial light modulator (SLM) on which the forked hologram is displayed. The first order diffracted output from the SLMs are then coupled to a single mode fiber (SMF), which is connected to single photon counting modules

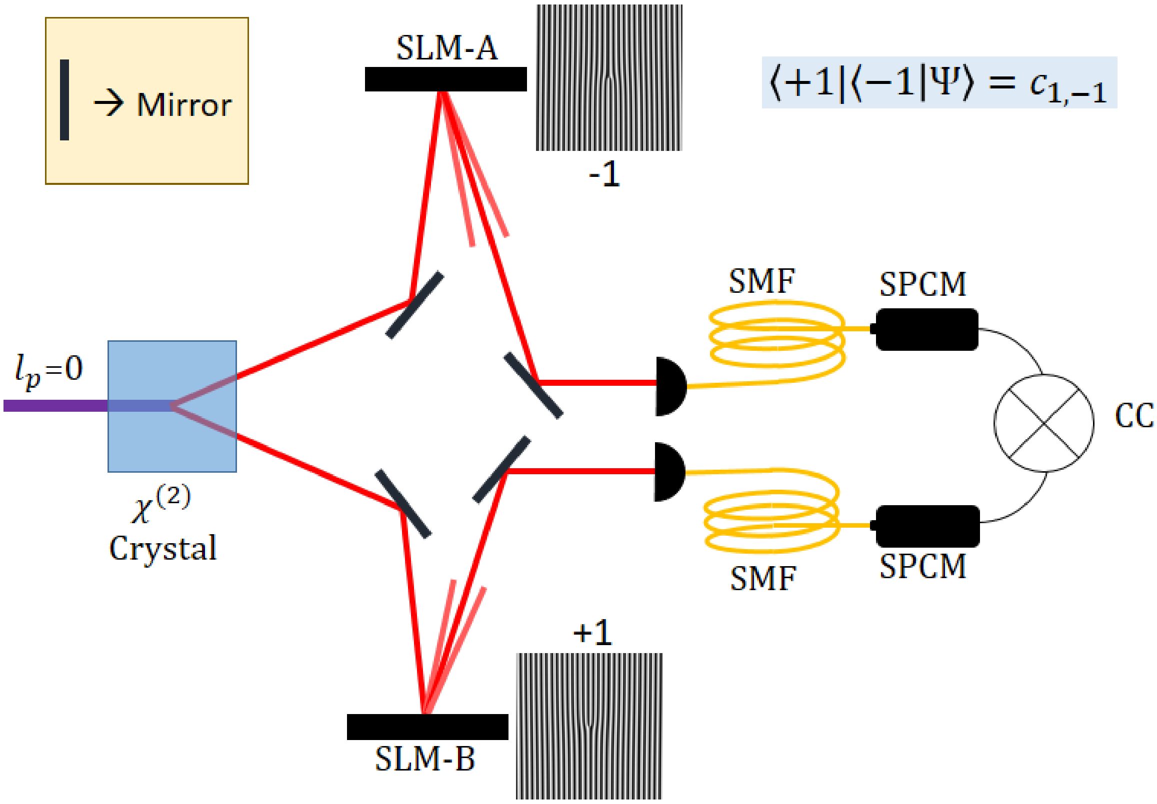

Fig. 5.4 Basic experimental scheme for the generation and measurement of SPDC biphoton OAM modes. SLM - Spatial light modulator; SMF - Single mode fiber; SPCM - Single photon counting module; CC - Coincidence counter.

(SPCM) to measure the photon counts. A coincidence counter connected to both the SPCMs will count the number of photon pairs in a particular biphoton OAM basis, which will represent the probability amplitude (c_{l_s,l_i}) corresponding to that basis. Here, in Fig. 5.4, to measure $c_{1,-1}$, a -1 order forked grating hologram is displayed on SLM-A and a +1 order hologram on SLM-B.

5.3 Selective tuning of biphoton OAM eigenstates in SPDC

When a pump beam of a particular OAM l_p is used, the generated biphoton OAM state is restricted to a particular OAM eigenbasis determined by the OAM selection rule (Eqn. 5.4). If we have a superposition of many optical vortices in the pump, the generated biphoton state will span over a larger range of OAM eigenbases. The probability of biphotons in a particular OAM basis can be tuned by controlling the amount of a particular OAM in the pump superposition. For example, consider an SPDC crystal pumped with an optical vortex beam of order +1. The generated twin photons will be in the state

$$\begin{aligned}|\psi\rangle^{(+1)} &= c_{1,0}|1\rangle_a|0\rangle_b + c_{0,1}|0\rangle_a|1\rangle_b \\ &\quad + c_{2,-1}|2\rangle_a|-1\rangle_b + c_{-1,2}|-1\rangle_a|2\rangle_b + ... \end{aligned} \tag{5.7}$$

When the crystal is pumped with a vortex beam of order -1, the SPDC state becomes

$$\begin{aligned}|\psi\rangle^{(-1)} &= c_{-1,0}|-1\rangle_a|0\rangle_b + c_{0,-1}|0\rangle_a|-1\rangle_b \\ &\quad + c_{-2,1}|-2\rangle_a|1\rangle_b + c_{1,-2}|1\rangle_a|-2\rangle_b + ... \end{aligned} \tag{5.8}$$

For a superposition of optical vortices of order +1 and -1, the SPDC output state will have all the terms from the basis expansion of $|\psi\rangle^{(+1)}$ and $|\psi\rangle^{(-1)}$ with values of each probability amplitude c_{l_s,l_i} different from that given in Eqn. 5.7 & 5.8. The probability amplitudes corresponding to different bases can be tuned by controlling the amount of +1 and -1 vortices in the superposed pump beam. To show this, we performed a proof-of-principle experiment with a pump beam as a superposition of optical vortices of order +1 and -1 with amounts of each vortex controlled by adjustment of polarization in the pump. The detailed experimental scheme and results are discussed below.

5.3.1 Generation of superposed optical vortices

Figure 5.5 shows the experimental schematic for the generation of superposition of optical vortices. We start with a Gaussian pump beam of a particular polarization. The state of the pump beam before the first half-wave plate (HWP1) can be expressed as the tensor product of polarization and orbital angular momentum (OAM) bases,

$$|\Psi_{in}\rangle = |H\rangle|0\rangle \tag{5.9}$$

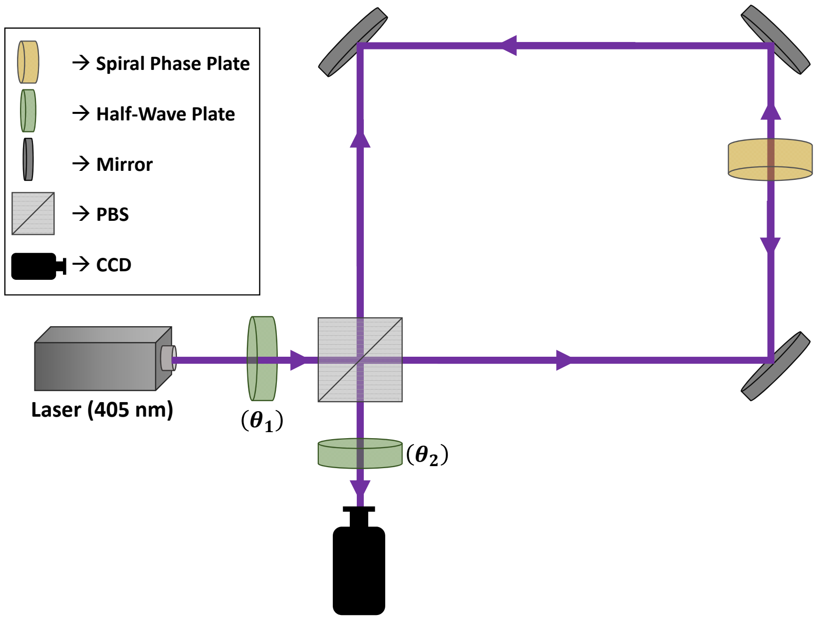

Fig. 5.5 Experimental schematic for the generation of superposition of optical vortices. PBS - Polarizing Beam Splitter

where $|H\rangle$ represents the state of horizontally polarized light and $|0\rangle$ denotes zero OAM state of the initial pump beam.

Using Jones matrix notation, we can represent horizontally and vertically polarized light with the respective column vectors

$$|H\rangle = \begin{pmatrix} 1 \\ 0 \end{pmatrix}, |V\rangle = \begin{pmatrix} 0 \\ 1 \end{pmatrix} \tag{5.10}$$

and the action of HWP1 whose fast axis is at an angle θ_1 with respect to vertical axis is given by a 2×2 Jones matrix

$$\hat{U}_{HWP}(\theta_1) = \begin{pmatrix} \cos 2\theta_1 & \sin 2\theta_1 \\ \sin 2\theta_1 & -\cos 2\theta_1 \end{pmatrix} \tag{5.11}$$

After passing through HWP1, the state of the pump beam becomes

$$\hat{U}_{HWP}(\theta_1)|H\rangle|\,0\rangle = (\cos 2\theta_1 |H\rangle + \sin 2\theta_1 |V\rangle)\,|0\rangle \tag{5.12}$$

Now the beam is fed into a polarizing Sagnac interferometer where the orthogonally polarized beams ($|H\rangle$ & $|V\rangle$) with equal but opposite OAM ($|l_p\rangle$ & $|-l_p\rangle$) counter-propagate and combine at the output of the interferometer. The Spiral Phase Plate (SPP) of order l_p converts the forward propagating Gaussian beam to an optical vortex of order l_p and back-propagating Gaussian beam to an optical vortex of order $-l_p$. So, the output state of the beam after interferometer is

$$|\Psi_{sag}\rangle = \cos 2\theta_1 |H\rangle|l_p\rangle + \sin 2\theta_1 |V\rangle|-l_p\rangle \tag{5.13}$$

This light is then passed through the second half-wave plate (HWP2) before the crystal, whose fast axis is at an angle θ_2 with respect to the vertical axis. Using similar calculations, we can find the state of the beam as

$$|\Psi_{out}\rangle = \cos 2\theta_1 \left(\cos 2\theta_2 |H\rangle + \sin 2\theta_2 |V\rangle\right)|l_p\rangle + \sin 2\theta_1 \left(\sin 2\theta_2 |H\rangle - \cos 2\theta_2 |V\rangle\right)|-l_p\rangle \tag{5.14}$$

Eqn. 5.14 can be re-written as

$$\begin{aligned}|\Psi_{out}\rangle = {} & |H\rangle \left(\cos 2\theta_1 \cos 2\theta_2 |l_p\rangle + \sin 2\theta_1 \sin 2\theta_2 |-l_p\rangle\right) \\ & + |V\rangle \left(\cos 2\theta_1 \sin 2\theta_2 |l_p\rangle - \sin 2\theta_1 \cos 2\theta_2 |-l_p\rangle\right)\end{aligned} \tag{5.15}$$

5.3.2 OAM correlations in SPDC with superposed vortex pump

When a superposed vortex pump in the state given by Eqn. 5.15 is incident of a non-linear crystal, it will down convert only the light of polarization oriented along the optic axis of it. Let the optic axis of the crystal is horizontally oriented. For $\theta_1 = 0$, the down converted portion of the pump beam is a variable superposition of optical vortices of order l_p and $-l_p$ based on the angle θ_2. For $\theta_2 = 0$, the down converted pump is a $+l_p$ vortex beam and for $\theta_2 = \pi/4$, it is a $-l_p$ vortex beam. For $\theta_2 = \pi/8$, the down converted pump contains equal mixture of $+l_p$ and $-l_p$ vortices.

The experimental setup to measure biphoton OAM correlation between signal and idler for a pump of superposed vortices, is given in Fig. 5.6. The setup consists of a UV diode laser (Toptica iBeam smart) of wavelength 405 nm and power 250 mW with a spectral band-width of 2 nm. For superposition of optical vortices, we set up a polarizing Sagnac interferometer. The pump beam,

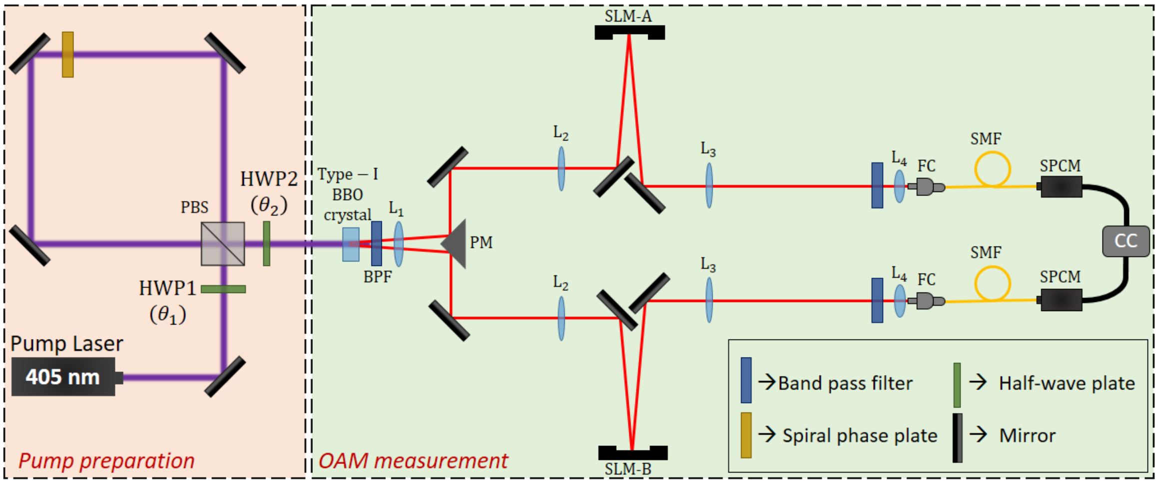

Fig. 5.6 Experimental setup for measuring OAM correlations in SPDC with pump as superposition of optical vortices. HWP - Half-wave plate; PBS - Polarizing beam splitter; SPP - Spiral phase plate; BBO - β-Barium borate; BPF - Band pass filter; PM - Prism mirror; L_1,L_2,L_3,L_4 - Lenses; SLM - Spatial light modulator; IF - Interference filter; FC - Fiber coupler; SMF - Single mode fiber; SPCM - Single photon counting module; CC - Coincidence counter.

passing through a polarizing beam splitter (PBS), is split into horizontal and vertical polarizations in each arm. Both beams pass through the spiral phase plate (SPP) of order 1, and form optical vortices (LG modes with $p = 0$) of equal and opposite charges (+1 & -1). They are combined again at the PBS to obtain superposition of equal and opposite vortices. A half wave plate (HWP1) is used to control the intensity distribution in each arm of the interferometer. A second half wave plate (HWP2) is used to orient the polarization of the pump with optic axis of the non-linear crystal Type-I β-Barium Borate (BBO), of thickness 5 mm. A band pass filter (BPF) of pass band 810$\pm$5 nm is used after the crystal to block pump beam and pass down converted photons.

The down converted signal and idler photons of wavelength 810 nm each (degenerate) generated from the crystal, are imaged to spatial light modulators (SLM-A & SLM-B) using lenses L_1 (f=100mm) and L_2 (f=500mm). SLMs are used to project the signal-idler pair to a particular OAM state. We select the first diffraction order of the output of each SLM so that the projected photons in the first order are Gaussian. This is achieved by imaging SLM plane at the fiber couplers (FC) in each arm using lenses

L_3 (f=750mm) and the aspheric lens L_4 attached with the fiber coupler (f=2mm). The fiber couplers are attached to the single mode fibers (P1-780A-FC-2, Thorlabs) each having a numerical aperture of 0.13 and a mode field diameter of 5.0±0.5 μm, which in turn are connected to the single photon counting modules (SPCM-AQRH-16-FC, Excelitas). The SPCMs have a timing resolution of 350 ps with 25 dark counts per second. Two band pass filters of pass band 810±5 nm are kept very close to the fiber couplers to make sure that other unwanted wavelengths are properly filtered out. To measure the number of correlated photon pairs, the two detectors are connected to a coincidence counter (CC), IDQuantique-ID800, having a time resolution of 81 ps.

5.3.3 Results

The light coming out of the interferometer will be in the state

$$|\psi\rangle = \cos 2\theta_1 |H\rangle|+1\rangle + e^{i\phi} \sin 2\theta_1 |V\rangle|-1\rangle \tag{5.16}$$

where $|H\rangle$, $|V\rangle$ and $|+1\rangle$, $|-1\rangle$ are basis vectors ot two dimensional complex vector spaces of polarization and OAM respectively. θ_1 is the angle of HWP1 and ϕ is the phase delay between the

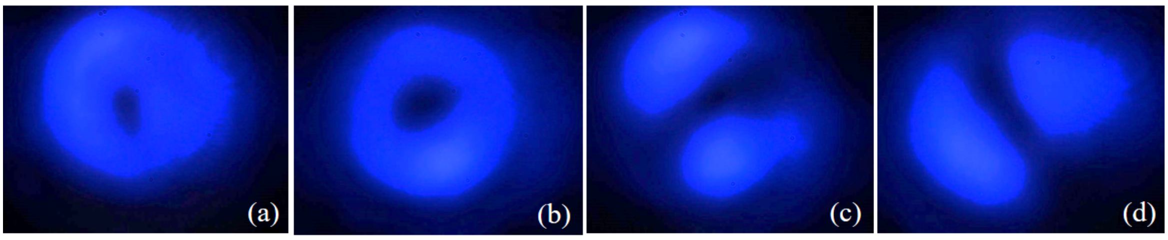

Fig. 5.7 Projected modes of pump beam for (a) horizontal (b) vertical (c) diagonal and (d) anti-diagonal polarizations.

superposing modes. For $\theta_1 = \pi/8$, we obtain superposition of +1 and -1 optical vortices of equal intensity. The polarization modes of the superposition is probed by keeping a polarizer (not shown in Fig. 5.6) before HWP2. The images of the pump beam for different polarization projections are shown in Fig. 5.7. For $\theta_1 = 0$, we have only vertical polarization in the interferometer that results into the order of the pump vortex $l_p = -1$. The entangled photons generated in SPDC will have a

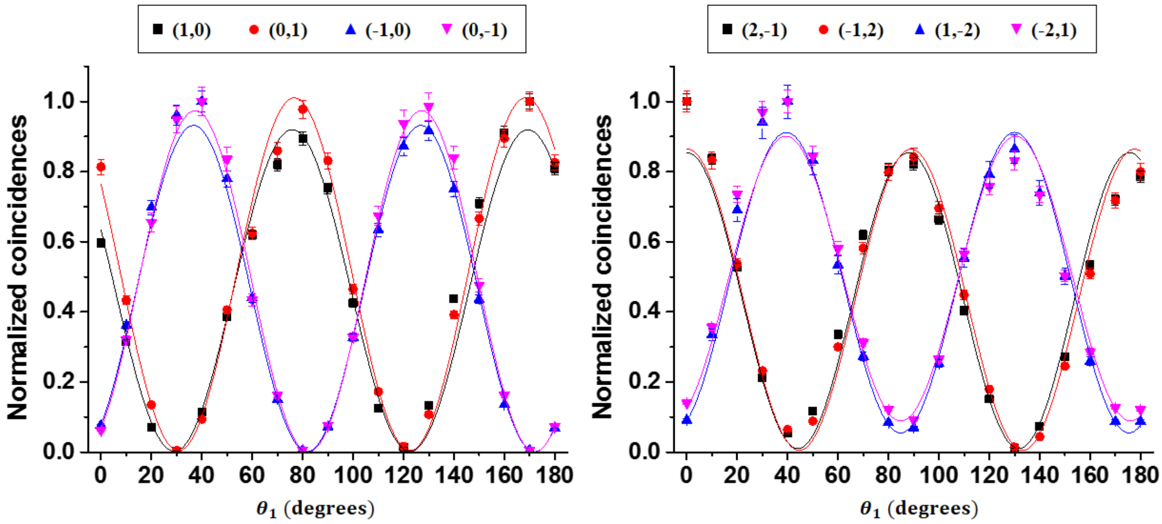

Fig. 5.8 Plots of coincidence counts with respect to HWP1 angles for (a) (1,0), (0,1), (-1,0), (0,-1) and (b) (2,-1), (-1,2), (1,-2), (-2,1) signal-idler OAM bases.

state of the form given in the Eqn. 5.8. For $\theta = \pi/4$, $l_p = 1$, the state of the SPDC will have the form given in Eqn. 5.7. For all other θ_1 values, the biphoton OAM state will have terms from both Eqn. 5.7 and 5.8. The coefficients (probability amplitudes) of each term in Eqn. 5.7 and 5.8 can be quantified by measuring the coincidence counts for each signal-idler OAM combinations. For example, to obtain the probability for generating $|1\rangle_a|0\rangle_b$, we projected fork hologram of charge -1 in SLM1 and hologram of charge zero in SLM2, and measured the coincidence counts. The mixing of +1 and -1 vortices is varied by changing θ_1. The variation of coincidences (normalized) for signal-idler OAM bases (-1,0), (0,-1), (1,0), (0,1), (-2,1), (1,-2), (-1,2) and (2,-1) with respect to θ_1 is shown in Fig. 5.8. Here, the numbers in the brackets correspond to the OAM of signal and idler respectively. We observed a sinusoidal variation of coincidence counts with θ_1. At the angles θ_1 where (-1,0) and (1,0) coincidence curves intersect, the generated entangled states have (-1,0), (0,-1), (1,0), (0,1) contributions with equal probability. So, by this method, we can generate biphoton OAM state in particular selected bases with controllable amounts.

5.4 Conclusion

We studied the orbital angular momentum correlations in SPDC. For a pump carrying single OAM, the SPDC biphoton OAM state is restricted to a single OAM eigenbasis. We showed that the biphoton state can be spanned over multiple OAM eigenbases by adding many OAM contributions to the pump, *i.e.* superpostion of different optical vortices. Further the generated state can be switched to different OAM bases just by controlling the amount of a particular OAM in the pump superposition that corresponds to a particular basis. The presented results may find applications in the generation of higher dimensional OAM entangled states.

Chapter 6

Conclusion and Outlook

This thesis basically deals with the study of spontaneous parametric down conversion (SPDC) process and its characterization for generating a good quantum source of light. In an SPDC process, a photon (called pump), when interacts with a non-linear optical crystal it annihilates to give two other photons of lower energies (called signal and idler). First, we discuss the conditions and laws that make SPDC process to happen inside the crystal and then we exploit the property of simultaneity of signal and idler in generation to define various correlations between them. We study the spatial distribution of individual SPDC photons for different for Gaussian as well as normal optical vortex (NOV) pump beams. Some novel structured light beams carrying orbital angular momentum (OAM) give similar spatial distribution in down conversion for higher as well as lower OAM values that they may be useful to carry OAM states of photons for communication.

Next, we generate heralded single photons from SPDC by detecting signal-idler pair using photon detectors and a coincidence counter. We study how pump and crystal parameters affect the biphoton heralding efficiency. We generate heralded twisted single photons (single photons carrying OAM) by pumping the SPDC crystal with an NOV beam. With Bessel-Gaussian (BG) and perfect optical vortex (POV) pump modes, we show that the heralding efficiency can be improved for higher OAM values.

Finally, we study the OAM correlations present in SPDC biphotons. We demonstrate a method to generate biphoton OAM state with selected OAM eigenbases in a controllable manner. The work presented in the thesis may be useful in implementing methods to generate higher dimensional entangled states used in some quantum information schemes.

6.1 Summary of the work-done

Chapter 1 provides a brief introduction on light sources, their characteristics and their classification based on the number distribution. We explain some common classical properties of light. Then, we discuss about quantum sources of light and how to characterize the quantum nature of light. Concept of modes, which is important in describing a light source, is illustrated with examples. Objective and the outline of the thesis is mentioned at the end of the chapter.

In chapter 2, we discuss the theory of spontaneous parametric down conversion in detail. We give the difference in the classical as well as the quantum treatment of SPDC and show how classical treatment cannot explain the process. Next, we discus about different phase-matching conditions for SPDC to occur. Careful calculation of phase-matching parameters is very important in choosing the non-linear crystals for a given experiment. Then, we talk about the non-classical features an SPDC source can produce, starting from proving the quantum nature of the source to the quantum entanglement realized in different degrees of freedom such as polarization and orbital angular momentum (OAM).

Chapter 3 studies the spatial distribution of signal or idler photons in SPDC for different pump modes, which is basically the angular spectrum of SPDC. We first discuss the angular spectrum with Gaussian pump beam. For a Gaussian beam focused with a spherical lens, we observe that the SPDC annular distribution becomes asymmetric. The asymmetry increases with the focusing of the pump. However, for the case of focusing with a cylindrical lens, we observe that the asymmetry on the diametrically opposite points of the SPDC ring can be manipulated by orienting the lateral axis of the lens along the optic axis of the crystal. The numerical results very well match with the experimental ones. We then perform a comparative study of SPDC angular spectra with different light modes carrying OAM. Here, we use mainly three modes – normal optical vortex (NOV), Bessel-Gaussian (BG) and perfect optical vortex (POV). For all the three pump modes, we observe a double Gaussian transverse intensity distribution in the SPDC annular ring. For the case of a NOV mode, the width of the double Gaussian distribution increases with the order of the vortex, which is due to the fact that the size of the vortex increases with the order. However, for the case of a BG or POV mode, the size remains same for any OAM value, and the corresponding SPDC ring distribution also remains the same.

The method to generate single photons from SPDC and their characterization are given in chapter 4. Single photons are generated in SPDC in a heralding configuration, where a photon from the produced pair is detected (heralding photon) that confirms the presence of the other photon (heralded single photon). On measurement, we show that the heralding efficiency of single photons decreases with focusing of the pump due to the increasing asymmetry of the SPDC ring distribution. We also generate heralded single photons carrying OAM (or heralded twisted single photons) by pumping the SPDC crystal with NOV, BG & POV, and compare their heralding efficiency. To detect the twisted single photons, we couple the idler photon to a single-mode fiber and collect the signal into a multi-mode fiber. We observe that the heralding efficiency is improved for higher OAM values for the case of pumping with BG and POV, than that for the case of a NOV pump. This is due to the fact that the size of an NOV increases with the vortex order whereas it remains the same for BG or POV beams. The results may find applications in the efficient preparation of higher dimensional entanglement.

In chapter 5, we discuss the OAM correlations present in an SPDC process. Access to higher dimensions in Hilbert space makes OAM a good candidate for realizing higher dimensional entanglement. We explore the distribution of OAM among signal and idler according to OAM conservation. A single OAM in the pump beam will give an SPDC biphoton OAM state with a single OAM eigenbasis. However, addition of multiple OAMs in the pump will generate biphoton modes spanned over the corresponding OAM eigenbases. To show this, we performed a proof-to-principle experiment by using a superposition of optical vortices of order +1 & -1 in the pump. We showed that the probability amplitudes of biphoton OAM states in different OAM eigenbases can be controlled by tuning the content of +1 or -1 OAM content in the pump. The present study may be useful in generating higher dimensional OAM entangled states in selected two-photon OAM bases.

6.2 Scope for future work

The non-classical correlations between signal and idler in SPDC in various degrees of freedom are realized using Gaussian beam as pump. The biphoton OAM modes in SPDC are used to prepare higher dimensional entangled states [118] for quantum information applications [119, 120]. The bandwidth of two-photon spiral spectra of SPDC with Gaussian pump is usually restricted to lower OAM values. This is mainly due to the size effects of conventional Laguerre-Gaussian modes used in the mode projecting holograms, with OAM [59]. Some new types of structured light modes carrying OAM – Bessel-Guassian (BG) and perfect optical vortex (POV) modes, have their sizes independent of the OAM. Therefore, the use of such modes in the pump may increase the spiral bandwidth of biphoton modes. As a primary investigation, we have already verified that the heralding efficiency of twisted single photons in SPDC is better when such pump beams are used (Chapter 4.5). With this, we finally intend to prepare efficient high dimensional entangled states for applications in quantum information processing.

If an unknown quantum state is entangled or separable is still a challenging problem among the scientific community [121–123]. Mostly, people use Bell's inequality violation as a primary qualification of entanglement. However, there are certain class of entangled states, called *Werner states* [124], which do not show Bell's violation [125]. An operator, called entanglement witness $\hat{W}$, is introduced to differentiate between separable states and entangled states. For a state represented by the density matrix ρ to be entangled, $\mathrm{Tr}[\hat{W}\rho] < 0$ and $\mathrm{Tr}[\hat{W}\sigma] \geq 0$ for all separable states with density matrices σ. In general, conventional entanglement witness operators do not have universal character [126] and they depend on the perfectness of the device used for the measurement [127]. Augusiak *et. al.* [128] introduced a universal entanglement witness operator that can confirm entanglement in any bipartite state, but is not measurement device independent. An entanglement witness in measurement device independent way was implemented by Branciard *et.al* [129], but which is not universal. Here, we plan to implement an experimental scheme to introduce a universal measurement device independent entanglement witness (UMDIEW) operator by using the polarization and OAM degrees of freedom in SPDC biphoton state. We first generate OAM Werner state in SPDC and then show that the introduced UMDIEW operator confirms the entanglement. So, UMDIEW will act as a universal answering machine for entanglement that solves the problem of reliable detection of entanglement for any type of two-qubit state.

References

[1] Z. Y. Ou and L. Mandel, *Violation of bell's inequality and classical probability in a two-photon correlation experiment,* Physical Review Letters **61**, 50–53 (1988).

[2] C. Gerry and P. Knight, *Introductory quantum optics* (Cambridge university press, 2005).

[3] G. Grynberg, A. Aspect, and C. Fabre, *Introduction to quantum optics: from the semi-classical approach to quantized light* (Cambridge university press, 2010).

[4] R. Birrittella, A. Gura, and C. C. Gerry, *Coherently stimulated parametric down-conversion, phase effects, and quantum-optical interferometry,* Physical Review A **91**, 053801 (2015).

[5] M. Hennrich, T. Legero, A. Kuhn, and G. Rempe, *Photon statistics of a non-stationary periodically driven single-photon source,* New Journal of Physics **6**, 86 (2004).

[6] M. Steiner, A. Hartschuh, R. Korlacki, and A. J. Meixner, *Highly efficient, tunable single photon source based on single molecules,* Applied Physics Letters **90**, 183122 (2007).

[7] C. Maurer, C. Becher, C. Russo, J. Eschner, and R. Blatt, *A single-photon source based on a single ca+ ion,* New Journal of Physics **6**, 94 (2004).

[8] S. Chen, Y.-A. Chen, T. Strassel, Z.-S. Yuan, B. Zhao, J. Schmiedmayer, and J.-W. Pan, *Deterministic and storable single-photon source based on a quantum memory,* Physical Review Letters **97**, 173004 (2006).

[9] A. J. Shields, *Semiconductor quantum light sources,* Nature Photonics **1**, 215 (2007).

[10] S. Strauf, N. G. Stoltz, M. T. Rakher, L. A. Coldren, P. M. Petroff, and D. Bouwmeester, *High-frequency single-photon source with polarization control,* Nature Photonics **1**, 704 (2007).

[11] E. Wu, J. Rabeau, G. Roger, F. Treussart, H. Zeng, P. Grangier, S. Prawer, and J.-F. Roch, *Room temperature triggered single-photon source in the near infrared,* New Journal of Physics **9**, 434 (2007).

[12] T. Gaebel, I. Popa, A. Gruber, M. Domhan, F. Jelezko, and J. Wrachtrup, *Stable single-photon source in the near infrared,* New Journal of Physics **6**, 98 (2004).

[13] E. Waks, E. Diamanti, and Y. Yamamoto, *Generation of photon number states,* New Journal of Physics **8**, 4 (2006).

[14] A. Soujaeff, T. Nishioka, T. Hasegawa, S. Takeuchi, T. Tsurumaru, K. Sasaki, and M. Matsui, *Quantum key distribution at 1550 nm using a pulse heralded single photon source,* Optics Express **15**, 726–734 (2007).

[15] A. B. U'Ren, C. Silberhorn, K. Banaszek, and I. A. Walmsley, *Efficient conditional preparation of high-fidelity single photon states for fiber-optic quantum networks,* Physical Review Letters **93**, 093601 (2004).

[16] E. Hecht, *Optics* (Pearson Education, 2016).

[17] R. W. Boyd, *Nonlinear Optics (Third Edition)* (Academic Press, 2008).

[18] M. Fox, *Quantum optics: an introduction*, vol. 15 (OUP Oxford, 2006).

[19] C. Monroe, *Quantum information processing with atoms and photons,* Nature **416**, 238 (2002).

[20] R. Daendliker, *Concept of modes in optics and photonics,* (2000).

[21] L. Allen, M. W. Beijersbergen, R. Spreeuw, and J. Woerdman, *Orbital angular momentum of light and the transformation of laguerre-gaussian laser modes,* Physical Review A **45**, 8185 (1992).

[22] D. N. Klyshko, *Coherent Photon Decay in a Nonlinear Medium,* Soviet Journal of Experimental and Theoretical Physics Letters **6**, 23 (1967).

[23] D. C. Burnham and D. L. Weinberg, *Observation of simultaneity in parametric production of optical photon pairs,* Physical Review Letters **25**, 84–87 (1970).

[24] I. Shoji, T. Kondo, A. Kitamoto, M. Shirane, and R. Ito, *Absolute scale of second-order nonlinear-optical coefficients,* Journal of Optical Society of America B **14**, 2268–2294 (1997).

[25] R. L. Byer and S. E. Harris, *Power and bandwidth of spontaneous parametric emission,* Physical Review **168**, 1064–1068 (1968).

[26] T. P. Grayson and G. A. Barbosa, *Spatial properties of spontaneous parametric down-conversion and their effect on induced coherence without induced emission,* Physical Review A **49**, 2948–2961 (1994).

[27] C. K. Hong, Z. Y. Ou, and L. Mandel, *Measurement of subpicosecond time intervals between two photons by interference,* Physical Review Letters **59**, 2044–2046 (1987).

[28] S.-Y. Baek and Y.-H. Kim, *Spectral properties of entangled photons generated via type-i frequency-nondegenerate spontaneous parametric down-conversion,* Physical Review A **80**, 033814 (2009).

[29] Y. H. Shih and C. O. Alley, *New type of einstein-podolsky-rosen-bohm experiment using pairs of light quanta produced by optical parametric down conversion,* Physical Review Letters **61**, 2921–2924 (1988).

[30] P. G. Kwiat, K. Mattle, H. Weinfurter, A. Zeilinger, A. V. Sergienko, and Y. Shih, *New high-intensity source of polarization-entangled photon pairs,* Physical Review Letters **75**, 4337–4341 (1995).

[31] A. Mair, A. Vaziri, G. Weihs, and A. Zeilinger, *Entanglement of the orbital angular momentum states of photons,* Nature **412**, 313–316 (2001).

[32] A. Migdall, S. V. Polyakov, J. Fan, and J. C. Bienfang, *Single-photon generation and detection: physics and applications*, vol. 45 (Academic Press, 2013).

[33] B. E. Saleh, M. C. Teich, and B. E. Saleh, *Fundamentals of photonics*, vol. 22 (Wiley New York, 1991).

[34] R. L. Sutherland, *Handbook of nonlinear optics* (CRC press, 2003).

[35] J. Rarity, P. Tapster, and E. Jakeman, *Observation of sub-poissonian light in parametric downconversion,* Optics Communications **62**, 201–206 (1987).

[36] Y. H. Shih and C. O. Alley, *New type of einstein-podolsky-rosen-bohm experiment using pairs of light quanta produced by optical parametric down conversion,* Physical Review Letters **61**, 2921–2924 (1988).

[37] P. G. Kwiat, E. Waks, A. G. White, I. Appelbaum, and P. H. Eberhard, *Ultrabright source of polarization-entangled photons,* Physical Review A **60**, R773 (1999).

[38] P. G. Kwiat, K. Mattle, H. Weinfurter, A. Zeilinger, A. V. Sergienko, and Y. Shih, *New high-intensity source of polarization-entangled photon pairs,* Physical Review Letters **75**, 4337–4341 (1995).

[39] S. Walborn, A. De Oliveira, R. Thebaldi, and C. Monken, *Entanglement and conservation of orbital angular momentum in spontaneous parametric down-conversion,* Physical Review A **69**, 023811 (2004).

[40] C. H. Monken, P. H. S. Ribeiro, and S. Pádua, *Transfer of angular spectrum and image formation in spontaneous parametric down-conversion,* Physical Review A **57**, 3123–3126 (1998).

[41] V. Vicuña-Hernández, H. Cruz-Ramírez, R. Ramírez-Alarcón, and A. B. U'Ren, *Classical to quantum transfer of optical vortices,* Optics Express **22**, 20027–20037 (2014).

[42] M. Jabir, N. A. Chaitanya, M. Mathew, and G. Samanta, *Direct transfer of classical non-separable states into hybrid entangled two photon states,* Scientific Reports **7**, 7331 (2017).

[43] S. Prabhakar, S. G. Reddy, A. Aadhi, A. Kumar, P. Chithrabhanu, G. Samanta, and R. Singh, *Spatial distribution of spontaneous parametric down-converted photons for higher order optical vortices,* Optics Communications **326**, 64–69 (2014).

[44] C. I. Osorio, A. Valencia, and J. P. Torres, *Spatiotemporal correlations in entangled photons generated by spontaneous parametric down conversion,* New Journal of Physics **10**, 113012 (2008).

[45] Y. Jeronimo-Moreno and R. Jáuregui, *Type i parametric down conversion of highly focused gaussian beams in finite length crystals,* Journal of Optics **16**, 065201 (2014).

[46] L. E. Vicent, A. B. U'Ren, R. Rangarajan, C. I. Osorio, J. P. Torres, L. Zhang, and I. A. Walmsley, *Design of bright, fiber-coupled and fully factorable photon pair sources,* New Journal of Physics **12**, 093027 (2010).

[47] A. Moura, W. Nogueira, S. Walborn, and C. Monken, *Transverse spatial and frequency properties of two-photon states generated by spontaneous parametric down-conversion,* arXiv preprint arXiv:0806.4624 (2008).

[48] R. Ramirez-Alarcon, H. Cruz-Ramirez, and A. B. U'Ren, *Effects of crystal length on the angular spectrum of spontaneous parametric downconversion photon pairs,* Laser Physics **23**, 055204 (2013).

[49] L. C. Andrews and R. L. Phillips, *Laser beam propagation through random media*, vol. 152 (SPIE press Bellingham, WA, 2005).

[50] M. S. Soskin, V. N. Gorshkov, M. V. Vasnetsov, J. T. Malos, and N. R. Heckenberg, *Topological charge and angular momentum of light beams carrying optical vortices,* Physical Review A **56**, 4064–4075 (1997).

[51] J. Durnin, J. Miceli Jr, and J. Eberly, *Diffraction-free beams,* Physical Review Letters **58**, 1499 (1987).

[52] D. McGloin and K. Dholakia, *Bessel beams: diffraction in a new light,* Contemporary Physics **46**, 15–28 (2005).

[53] Z. Bouchal, J. Wagner, and M. Chlup, *Self-reconstruction of a distorted nondiffracting beam,* Optics Communications **151**, 207–211 (1998).

[54] F. Gori, G. Guattari, and C. Padovani, *Bessel-gauss beams,* Optics Communications **64**, 491–495 (1987).

[55] S. Li and J. Wang, *Multi-orbital-angular-momentum multi-ring fiber for high-density space-division multiplexing,* IEEE Photonics Journal **5**, 7101007–7101007 (2013).

[56] P. Gregg, P. Kristensen, S. Golowich, J. Olsen, P. Steinvurzel, and S. Ramachandran, *Stable transmission of 12 oam states in air-core fiber,* in "Lasers and Electro-Optics (CLEO), 2013 Conference on," (IEEE, 2013), pp. 1–2.

[57] A. E. Willner, H. Huang, Y. Yan, Y. Ren, N. Ahmed, G. Xie, C. Bao, L. Li, Y. Cao, Z. Zhao *et al.*, *Optical communications using orbital angular momentum beams,* Advances in Optics and Photonics **7**, 66–106 (2015).

[58] S. G. Reddy, C. Permangatt, S. Prabhakar, A. Anwar, J. Banerji, and R. Singh, *Divergence of optical vortex beams,* Applied Optics **54**, 6690–6693 (2015).

[59] H. Qassim, F. M. Miatto, J. P. Torres, M. J. Padgett, E. Karimi, and R. W. Boyd, *Limitations to the determination of a laguerre-gauss spectrum via projective, phase-flattening measurement,* Journal of Optical Society of America B **31**, A20–A23 (2014).

[60] A. S. Ostrovsky, C. Rickenstorff-Parrao, and V. Arrizón, *Generation of the "perfect" optical vortex using a liquid-crystal spatial light modulator,* Optics Letters **38**, 534–536 (2013).

[61] P. Vaity and L. Rusch, *Perfect vortex beam: Fourier transformation of a bessel beam,* Optics Letters **40**, 597–600 (2015).

[62] Y. Jian-Ping, G. Wei-Jian, W. Hai-Feng, L. Quan, and W. Yu-Zhu, *Generations of dark hollow beams and their applications in laser cooling of atoms and all optical-type bose-einstein condensation,* Chinese Physics **11**, 1157 (2002).

[63] I. Manek, Y. B. Ovchinnikov, and R. Grimm, *Generation of a hollow laser beam for atom trapping using an axicon,* Optics Communications **147**, 67–70 (1998).

[64] G. Schweiger, R. Nett, B. Özel, and T. Weigel, *Generation of hollow beams by spiral rays in multimode light guides,* Optics Express **18**, 4510–4517 (2010).

[65] M. Beijersbergen, R. Coerwinkel, M. Kristensen, and J. Woerdman, *Helical-wavefront laser beams produced with a spiral phaseplate,* Optics Communications **112**, 321–327 (1994).

[66] C. Zhao, Y. Cai, F. Wang, X. Lu, and Y. Wang, *Generation of a high-quality partially coherent dark hollow beam with a multimode fiber,* Optics Letters **33**, 1389–1391 (2008).

[67] S. G. Reddy, A. Kumar, S. Prabhakar, and R. Singh, *Experimental generation of ring-shaped beams with random sources,* Optics Letters **38**, 4441–4444 (2013).

[68] E. J. Galvez, L. E. Coyle, E. Johnson, and B. J. Reschovsky, *Interferometric measurement of the helical mode of a single photon,* New Journal of Physics **13**, 053017 (2011).

[69] H. Cruz-Ramírez, R. Ramírez-Alarcón, F. J. Morelos, P. A. Quinto-Su, J. C. Gutiérrez-Vega, and A. B. U'Ren, *Observation of non-diffracting behavior at the single-photon level,* Optics Express **20**, 29761–29768 (2012).

[70] R. S. Bennink, S. J. Bentley, R. W. Boyd, and J. C. Howell, *Quantum and classical coincidence imaging,* Physical Review Letters **92**, 033601 (2004).

[71] F. Flossmann, U. Schwarz, and M. Maier, *Propagation dynamics of optical vortices in laguerre-gaussian beams,* Optics Communications **250**, 218 – 230 (2005).

[72] C. Perumangatt, G. R. Salla, A. Anwar, A. Aadhi, S. Prabhakar, and R. Singh, *Scattering of non-separable states of light,* Optics Communications **355**, 301 – 305 (2015).

[73] S. Slussarenko, V. D'Ambrosio, B. Piccirillo, L. Marrucci, and E. Santamato, *The polarizing sagnac interferometer: a tool for light orbital angular momentum sorting and spin-orbit photon processing,* Optics Express **18**, 27205–27216 (2010).

[74] Q. Zhan, *Cylindrical vector beams: from mathematical concepts to applications,* Advances in Optics and Photonics **1**, 1–57 (2009).

[75] A. Aadhi, P. Vaity, P. Chithrabhanu, S. G. Reddy, S. Prabakar, and R. P. Singh, *Non-coaxial superposition of vector vortex beams,* Applied Optics **55**, 1107–1111 (2016).

[76] M. J. Padgett and J. Courtial, *Poincaré-sphere equivalent for light beams containing orbital angular momentum,* Optics Letters **24**, 430–432 (1999).

[77] A. Joobeur, B. E. A. Saleh, T. S. Larchuk, and M. C. Teich, *Coherence properties of entangled light beams generated by parametric down-conversion: Theory and experiment,* Physical Review A **53**, 4360–4371 (1996).

[78] M. D'Angelo, Y.-H. Kim, S. P. Kulik, and Y. Shih, *Identifying entanglement using quantum ghost interference and imaging,* Physical Review Letters **92**, 233601 (2004).

[79] T. J. Herzog, P. G. Kwiat, H. Weinfurter, and A. Zeilinger, *Complementarity and the quantum eraser,* Physical Review Letters **75**, 3034–3037 (1995).

[80] D. Tasca, S. Walborn, P. S. Ribeiro, F. Toscano, and P. Pellat-Finet, *Propagation of transverse intensity correlations of a two-photon state,* Physical Review A **79**, 033801 (2009).

[81] J. Arlt, K. Dholakia, L. Allen, and M. J. Padgett, *Parametric down-conversion for light beams possessing orbital angular momentum,* Physical Review A **59**, 3950–3952 (1999).

[82] S. P. Walborn, S. Pádua, and C. H. Monken, *Conservation and entanglement of hermite-gaussian modes in parametric down-conversion,* Physical Review A **71**, 053812 (2005).

[83] M. McLaren, M. Agnew, J. Leach, F. S. Roux, M. J. Padgett, R. W. Boyd, and A. Forbes, *Entangled bessel-gaussian beams,* Optics Express **20**, 23589–23597 (2012).

[84] J. Romero, D. Giovannini, M. McLaren, E. Galvez, A. Forbes, and M. Padgett, *Orbital angular momentum correlations with a phase-flipped gaussian mode pump beam,* Journal of Optics **14**, 085401 (2012).

[85] F. A. Bovino, P. Varisco, A. M. Colla, G. Castagnoli, G. D. Giuseppe, and A. V. Sergienko, *Effective fiber-coupling of entangled photons for quantum communication,* Optics Commnications **227**, 343 – 348 (2003).

[86] S. Castelletto, I. P. Degiovanni, A. Migdall, and M. Ware, *On the measurement of two-photon single-mode coupling efficiency in parametric down-conversion photon sources,* New Journal of Physics **6**, 87 (2004).

[87] S. A. Castelletto, I. P. Degiovanni, A. Migdall, V. Schettini, and M. Ware, *Measurement of coupling pdc photon sources with single-mode and multimode optical fibers,* in "Optical Science and Technology, the SPIE 49th Annual Meeting," (International Society for Optics and Photonics, 2004), pp. 60–72.

[88] A. Dragan, *Efficient fiber coupling of down-conversion photon pairs,* Physical Review A **70**, 053814 (2004).

[89] R. Andrews, E. R. Pike, and S. Sarkar, *Optimal coupling of entangled photons into single-mode optical fibers,* Optics Express **12**, 3264–3269 (2004).

[90] Y.-S. Kim, O. Kwon, S. M. Lee, J.-C. Lee, H. Kim, S.-K. Choi, H. S. Park, and Y.-H. Kim, *Observation of young's double-slit interference with the three-photon n00n state,* Optics Express **19**, 24957–24966 (2011).

[91] D. Ljunggren and M. Tengner, *Optimal focusing for maximal collection of entangled narrow-band photon pairs into single-mode fibers,* Physical Review A **72**, 062301 (2005).

[92] A. Fedrizzi, T. Herbst, A. Poppe, T. Jennewein, and A. Zeilinger, *A wavelength-tunable fiber-coupled source of narrowband entangled photons,* Optics Express **15**, 15377–15386 (2007).

[93] C. Kurtsiefer, M. Oberparleiter, and H. Weinfurter, *High-efficiency entangled photon pair collection in type-ii parametric fluorescence,* Physical Review A **64**, 023802 (2001).

[94] G. D. Boyd and D. A. Kleinman, *Parametric interaction of focused gaussian light beams,* Journal of Applied Physics **39**, 3597–3639 (1968).

[95] P. B. Dixon, D. Rosenberg, V. Stelmakh, M. E. Grein, R. S. Bennink, E. A. Dauler, A. J. Kerman, R. J. Molnar, and F. N. C. Wong, *Heralding efficiency and correlated-mode coupling of near-ir fiber-coupled photon pairs,* Physical Review A **90**, 043804 (2014).

[96] J.-L. Smirr, M. Deconinck, R. Frey, I. Agha, E. Diamanti, and I. Zaquine, *Optimal photon-pair single-mode coupling in narrow-band spontaneous parametric downconversion with arbitrary pump profile,* Journal of Optical Society of America B **30**, 288–301 (2013).

[97] C. Monken, P. S. Ribeiro, and S. Pádua, *Optimizing the photon pair collection efficiency: A step toward a loophole-free bell's inequalities experiment,* Physical Review A **57**, R2267 (1998).

[98] H. D. L. Pires, F. Coppens, and M. van Exter, *Type-i spontaneous parametric down-conversion with a strongly focused pump,* Physical Review A **83**, 033837 (2011).

[99] J.-C. Lee and Y.-H. Kimp, *Spatial and spectral properties of entangled photons from spontaneous parametric down-conversion with a focused pump,* Optics Communications **366**, 442 – 450 (2016).

[100] R. S. Bennink, Y. Liu, D. D. Earl, and W. P. Grice, *Spatial distinguishability of photons produced by spontaneous parametric down-conversion with a focused pump,* Physical Review A **74**, 023802 (2006).

[101] P. Lee, M. Van Exter, and J. Woerdman, *How focused pumping affects type-ii spontaneous parametric down-conversion,* Physical Review A **72**, 033803 (2005).

[102] M. V. Jabir, N. A. Chaitanya, A. Aadhi, and G. Samanta, *Generation of "perfect" vortex of variable size and its effect in angular spectrum of the down-converted photons,* Scientific reports **6**, 21877 (2016).

[103] B. Septriani, J. A. Grieve, K. Durak, and A. Ling, *Thick-crystal regime in photon pair sources,* Optica **3**, 347–350 (2016).

[104] S. P. Walborn, A. N. de Oliveira, R. S. Thebaldi, and C. H. Monken, *Entanglement and conservation of orbital angular momentum in spontaneous parametric down-conversion,* Physical Review A **69**, 023811 (2004).

[105] P. Kok, W. J. Munro, K. Nemoto, T. C. Ralph, J. P. Dowling, and G. J. Milburn, *Linear optical quantum computing with photonic qubits,* Reviews of Modern Physics **79**, 135–174 (2007).

[106] J. C. Maxwell, *Viii. a dynamical theory of the electromagnetic field,* Philosophical Transactions of the Royal Society of London **155**, 459–512 (1865).

[107] J. Poynting *et al.*, *The wave motion of a revolving shaft, and a suggestion as to the angular momentum in a beam of circularly polarised light,* Proceedings of Royal Society of London A **82**, 560–567 (1909).

[108] R. A. Beth, *Mechanical detection and measurement of the angular momentum of light,* Physical Review **50**, 115 (1936).

[109] J. D. Jackson, *Classical electrodynamics* (Wiley, New York, NY, 1999), 3rd ed.

[110] N. J. Cerf, M. Bourennane, A. Karlsson, and N. Gisin, *Security of quantum key distribution using d-level systems,* Physical Review Letters **88**, 127902 (2002).

[111] A. C. Dada, J. Leach, G. S. Buller, M. J. Padgett, and E. Andersson, *Experimental high-dimensional two-photon entanglement and violations of generalized bell inequalities,* Nature Physics **7**, 677 (2011).

[112] F. M. Miatto, A. M. Yao, and S. M. Barnett, *Full characterization of the quantum spiral bandwidth of entangled biphotons,* Physical Review A **83**, 033816 (2011).

[113] J. Torres, A. Alexandrescu, and L. Torner, *Quantum spiral bandwidth of entangled two-photon states,* Physical Review A **68**, 050301 (2003).

[114] H. D. L. Pires, H. Florijn, and M. Van Exter, *Measurement of the spiral spectrum of entangled two-photon states,* Physical Review Letters **104**, 020505 (2010).

[115] J. Romero, D. Giovannini, S. Franke-Arnold, S. Barnett, and M. Padgett, *Increasing the dimension in high-dimensional two-photon orbital angular momentum entanglement,* Physical Review A **86**, 012334 (2012).

[116] J. Leach, M. J. Padgett, S. M. Barnett, S. Franke-Arnold, and J. Courtial, *Measuring the orbital angular momentum of a single photon,* Physical Review Letters **88**, 257901 (2002).

[117] Z. Wang, Z. Zhang, and Q. Lin, *A novel method to determine the helical phase structure of laguerreâ€“gaussian beams,* Journal of Optics A: Pure and Applied Optics **11**, 085702 (2009).

[118] M. G. McLaren, F. S. Roux, and A. Forbes, *Realising high-dimensional quantum entanglement with orbital angular momentum,* South African Journal of Science **111**, 01–09 (2015).

[119] Q. Zeng, T. Li, X. Song, and X. Zhang, *Realization of optimized quantum controlled-logic gate based on the orbital angular momentum of light,* Optics Express **24**, 8186–8193 (2016).

[120] Z.-R. Jian, G.-S. Jin, and T.-J. Wang, *Efficient quantum secure direct communication using the orbital angular momentum of single photons,* International Journal of Theoretical Physics **55**, 1811–1819 (2016).

[121] R. Horodecki and M. Horodecki, *Information-theoretic aspects of inseparability of mixed states,* Physical Review A **54**, 1838–1843 (1996).

[122] L. M. Ioannou, B. C. Travaglione, D. Cheung, and A. K. Ekert, *Improved algorithm for quantum separability and entanglement detection,* Physical Review A **70**, 060303 (2004).

[123] L. M. Ioannou and B. C. Travaglione, *Quantum separability and entanglement detection via entanglement-witness search and global optimization,* Physical Review A **73**, 052314 (2006).

[124] R. F. Werner, *Quantum states with einstein-podolsky-rosen correlations admitting a hidden-variable model,* Physical Review A **40**, 4277 (1989).

[125] R. Horodecki, P. Horodecki, M. Horodecki, and K. Horodecki, *Quantum entanglement,* Reviews of Modern Physics **81**, 865 (2009).

[126] R. Augusiak, J. Bae, J. Tura, and M. Lewenstein, *Checking the optimality of entanglement witnesses: an application to structural physical approximations,* Journal of Physics A: Mathematical and Theoretical **47**, 065301 (2014).

[127] P. Xu, X. Yuan, L.-K. Chen, H. Lu, X.-C. Yao, X. Ma, Y.-A. Chen, and J.-W. Pan, *Implementation of a measurement-device-independent entanglement witness,* Physical Review Letters **112**, 140506 (2014).

[128] R. Augusiak, M. Demianowicz, and P. Horodecki, *Universal observable detecting all two-qubit entanglement and determinant-based separability tests,* Physical Review A **77**, 030301 (2008).

[129] C. Branciard, D. Rosset, Y.-C. Liang, and N. Gisin, *Measurement-device-independent entanglement witnesses for all entangled quantum states,* Physical Review Letters **110**, 060405 (2013).

LIST OF PUBLICATIONS

Publications contributing to this thesis:

1. *Direct transfer of pump amplitude to parametric down-converted photons*,
   Ali Anwar, Pravin Vaity, Chithrabhanu P and R. P. Singh, Optics Letters **43(5)**, 1155-1158 (2018).

2. *Selecting the pre-detection characteristics for fiber coupling of parametric down-converted biphoton modes*,
   Ali Anwar, Chithrabhanu P, Salla Gangi Reddy, Nijil Lal and R. P. Singh, Optics Communications **382**, 219-224 (2017).

3. *Tunable quantum entangled states*,
   Ali Anwar, Nijil Lal, Chithrabhanu P, Vijay Kumar and R. P. Singh, 13th International Conference on Fiber Optics and Photonics, OSA Technical Digest (online) (Optical Society of America, 2016), paper **W2C.2**.

4. *Optimizing focused pump beam characteristics for maximum correlated photon pairs in non-collinear parametric down-conversion*,
   Ali Anwar, Nijil Lal, Chithrabhanu P, Vijay Kumar and R. P. Singh, Proceedings of IEEE Xplore 16596509, Workshop on Recent Advances in Photonics (2014), doi:10.1109/WRAP.2015.7806002.

Other publications:

1. *Controlling the biphoton orbital angular momentum eigenmodes using asymmetric pump vortex beam*,
   M V Jabir, **Ali Anwar**, and G. K. Samanta, arXiv,1803.04635 (2018) (under communication).

2. *Structuring Stokes correlation functions using vector-vortex beam*,
   Vijay Kumar, **Ali Anwar** and R. P. Singh, Journal of Optics **20(1)**, 015604 (2017).

3. *Quantum information with even and odd states of orbital angular momentum states of light*, Chithrabhanu P, Nijil Lal, **Ali Anwar**, Salla Gangi Reddy and R. P. Singh, Physics Letters A **381**, 1858-1865 (2017).

4. *Pancharatnam phase in non-separable states of light*, Chithrabhanu P, Salla Gangi Reddy, Nijil Lal, **Ali Anwar**, A. Aadhi and R. P. Singh, Journal of Optical Society of America B **33(10)**, 2093-2098 (2017).

5. *Recovering the vorticity of a light beam after scattering*, Salla Gangi Reddy, Chithrabhanu P, Shashi Prabhakar, **Ali Anwar** and R. P. Singh, Applied Physics Letters **107**, 021104 (2015).

6. *Scattering of non-separable states of light*, Chithrabhanu P, Salla Gangi Reddy, **Ali Anwar**, Aadhi A, Shashi Prabhakar, and R. P. Singh, Optics Communications **355**, 301-305 (2015).

7. *Divergence of optical vortex beams*, Salla Gangi Reddy, Chithrabhanu P, Shashi Prabhakar, **Ali Anwar**, J. Banerji and R. P. Singh, Applied Optics **54(22)**, 6690-6693 (2015).

Conference papers:

1. **Ali Anwar**, Nijil Lal, Chithrabhanu P, Vijay Kumar and R. P. Singh, *Tunable quantum entangled states* in 13th International Conference on Fiber Optics and Photonics, OSA Technical Digest (online) (Optical Society of America, 2016), paper **W2C.2**.

2. Chithrabhanu P, Nijil Lal, **Ali Anwar**, Salla Gangi Reddy and R. P. Singh, *A stabilized polarization controlled orbital angular momentum sorter*, 13th International Conference on Fiber Optics and Photonics, OSA Technical Digest (online) (Optical Society of America, 2016), paper **Tu4A.46**.

3. Nijil Lal, Biveen Shajilal, **Ali Anwar**, Chithrabhanu P and R. P. Singh, *Observing sub-poissonian statistics of heralded single photons using an oscilloscope*, 13th International

Conference on Fiber Optics and Photonics, OSA Technical Digest (online) (Optical Society of America, 2016), paper **Th3A.72**.

4. **Ali Anwar**, Chithrabhanu P, Salla Gangi Reddy, Shashi Prabhakar, Nijil Lal and R. P. Singh, *Optimizing focused pump beam characteristics for maximum correlated photon pairs in non-collinear degenerate parametric down conversion*, Proceedings of IEEE Xplore 16596509, Workshop on Recent Advances in Photonics (2014), doi: 10.1109/WRAP.2015.7806002.

5. Chithrabhanu P, Salla Gangi Reddy, **Ali Anwar**, R. P. Singh, *Generalized orbital angular momentum Poincare sphere*, Proceedings of SPIE 9654, International Conference on Optics and Photonics 2015, 965421 (2015), doi: 10.1117/12.2182651.

6. Salla Gangi Reddy, Shashi Prabhakar, **M. A. Ali Anwar**, J. Banerji, and R. P. Singh, *Modelling of scattered optical vortices* in 12th International Conference on Fiber Optics and Photonics, OSA Technical Digest (online) (Optical Society of America, 2014), paper **S5A.32**.

Publications attached with the thesis

1. *Direct transfer of pump amplitude to parametric down-converted photons*,

   Ali Anwar, Pravin Vaity, Chithrabhanu P and R. P. Singh, Optics Letters **43(5)**, 1155-1158 (2018).

2. *Selecting the pre-detection characteristics for fiber coupling of parametric down-converted biphoton modes*,

   Ali Anwar, Chithrabhanu P, Salla Gangi Reddy, Nijil Lal and R. P. Singh, Optics Communications **382**, 219-224 (2017).